Molecular mechanism of barnacle adhesion : a structural approach and underlying biochemistry

Sunyoung Hur

Sunyoung Hur. Molecular mechanism of barnacle adhesion : a structural approach and underlying biochemistry. Material chemistry. Sorbonne Université; Nanyang Technological University (Singapour), 2022. English. NNT : 2022SORUS572 . tel-04318937

HAL Id: tel-04318937
https://theses.hal.science/tel-04318937v1

NANYANG
TECHNOLOGICAL
UNIVERSITY
SINGAPORE

SORBONNE
UNIVERSITÉ

MOLECULAR MECHANISM OF BARNACLE ADHESION : A STRUCTURAL APPROACH AND UNDERLYING BIOCHEMISTRY

Dual Degree of Doctor of Philosophy (Ph.D.)
at Nanyang Technological University (NTU)
and Sorbonne Université (SU)

SUNYOUNG HUR

Interdisciplinary Graduate School
Energy Research Institute at NTU (ERIAN)
Physique et Chimie des Matériaux at Sorbonne Université

2022

MOLECULAR MECHANISM OF BARNACLE ADHESION : A STRUCTURAL APPROACH AND UNDERLYING BIOCHEMISTRY

SUNYOUNG HUR

Interdisciplinary Graduate School
Energy Research Institute at NTU (ERIAN)

Physique et Chimie des Matériaux at Sorbonne Université

A thesis submitted to the Nanyang Technological University
in partial fulfilment of the requirement for the degree of Doctor of Philosophy

2022

Statement of Originality

I hereby certify that the work embodied in this thesis is the result of original research, is free of plagiarised materials, and has not been submitted for a higher degree to any other University or Institution.

16/02/2022

Date

SunYoung Hur

Supervisor Declaration Statement

I have reviewed the content and presentation style of this thesis and declare it is free of plagiarism and of sufficient grammatical clarity to be examined. To the best of my knowledge, the research and writing are those of the candidate except as acknowledged in the Author Attribution Statement. I confirm that the investigations were conducted in accord with the ethics policies and integrity standards of Nanyang Technological University and that the research data are presented honestly and without prejudice.

24/03/2022

. . . .

Date

. . . .

Prof. Ali Miserez

Authorship Attribution Statement

This thesis contains material from two papers going to be published in the following peer-reviewed journals where I am the first author.

Chapter 4 is going to be published as **Hur, S.** ; Wang, J. ; Yu, J. ; Boujday, S. ; Miserez, A. Surface adsorption and adhesion studies of barnacle cement proteins with structural understanding.

The contributions of the co-authors are as follows:

- Prof. Miserez and Prof. Boujday provided the initial project direction and reviewed the manuscript drafts.
- I prepared the manuscript drafts. The manuscript was revised by Prof. Miserez, Prof. Boujday, and Prof. Jing.
- I designed the study, performed the laboratory work including sample preparation, microscopy, and other surface analysis techniques at Nanyang Technological University and Sorbonne Universite.
- Under the guidance of Prof. Jing, surface interaction experiments using the Surface Force Apparatus were carried out and analyzed with a PhD student Mr. Wang.
- Research director Salmain advised on protein analysis.

Chapter 5 is going to be published as **Hur, S.** ; Méthivier, C. ; Wilson, A ; Boujday, S. ; Miserez, A. Biomineralization in barnacle base plate with the effect of adhesive cement proteins.

The contributions of the co-authors are as follows:

- Prof. Miserez and Prof. Boujday provided the initial project direction and reviewed the manuscript drafts.
- I prepared the manuscript drafts. The manuscript was revised by Prof. Miserez and Prof. Boujday.
- I designed the study, performed the laboratory work including sample preparation, microscopy, and other surface analysis techniques at Sorbonne Universite.
- Ingénieur de Recherche Methivier assisted in the collection and provided guidance in the interpretation of the X-ray photoelectron spectroscopy measurement data.
- Dr. Wilson assisted in building 3D printed model and reviewed the manuscript.

16/02/2022

Date

SunYoung Hur

Acknowledgements

I would like to express my sincere gratitude to people who supported my research not only in a technical aspect but also internally.

I appreciate my supervisor Prof. Ali Miserez in Nanyang Technological University (NTU), who guided and influenced me the most with his strong support, academic guidance, and motivation. His good insight and consistent passion for research helped me proceed the professional career on the right direction with a good discern of the goal, by overcoming obstacles and difficult times. His patience and kind understanding enabled me to focus on work even during the Covid time and multiple lockdowns. Prof. Souhir Boujday in Sorbonne Université (SU) has offered huge guidance and insightful advice as a co-supervisor to improve research ideas and improve my project in her lab. It would not have been possible for me to continue my work and life in Paris without her warm supporting. She encouraged and motivated me greatly to focus on the most important things and to make the right choices when I faced difficulties. Prof. Chandra Shekhar Verma in Bioinformatics Institute, A*STAR, has provided excellent guidance for the project with his discerning advice as a mentor.

I am also sincerely grateful to Prof. Yu Jing in NTU Materials Science and Engineering (MSE) for broadening my knowledge in marvelous concepts and useful skills for Surface Force Apparatus experiments, Prof. Scott A. Rice and Dr. Poh Wee Han in Singapore Centre for Environmental Life Sciences Engineering (SCELSE) for teaching me antimicrobial experiments and letting me work in their laboratory, research engineer Michèle Salmain in Centre National de la Recherche Scientifique (CNRS) for being there and supporting my thesis journey with both academic and non-academic advices as a great mentor, research engineer Christophe Méthivier in CNRS for guiding me through X-ray photoelectron spectroscopy (XPS) techniques and theories, and Prof. Atul N. Parikh for advising me during my manuscript work. I cannot exaggerate tremendous help and support from Prof. Bo Liedberg as a previous dean of Interdisciplinary Graduate School (IGS), encouraging me to stay on good track of the double degree program between the two amazing research groups, even during his last years which had strong international health crisis. Prof. Sierin Lim in School of Chemical and Biomedical Engineering (SCBE) as an associate dean for global partnerships at Graduate College, has always motivated me for collaborations and active interactions.

It has been a great honor and happiness to work with my wonderful colleagues in the Biological & Biomimetic Materials Laboratory (BBML) in NTU and Laboratoire de Réactivité de Surface (LRS) in SU. All of them made my four years inside and outside the labs very pleasurable and invaluable. I am greatly thankful to my mentors Dr. Akshita Kumar and Dr. Harini Mohanram, who have been dedicated to guiding me in the lab. With their research expertise especially in biology, I could improve my research knowledge and experimental skills in the field. I thank to my colleagues in BBML as endearing supporters, whom I have learned necessary in-lab skills at the same time who turned every second of work as joyful moments, including Dr. Eva Hiew Shu Hui, Dr. Kanagavel Deepankumar, Dr. Chua Jia Qing Isaiah, Loke Jun Jie, Soon Wei Long, Kenrick Koh, and Sun Yue. I am thankful to my colleagues in LRS, for their constant motivation and encouragement, enthusiastic scientific discussions we had, and warm-hearted supporting, including Dr. David Hu, Dr. Yacine Mazouzi, Dr. Vincent Pellas, Dr. Somia Tomane, Dr. Nadia Nazi, and Mathieu Nicolas. Special thanks to Jining Wang from MSE as a great collaborator and a great friend, for sharing countless intellectual discussions with me during these few years. All these people willingly provided me with valuable tips for my professional and personal growth. The work done and written in this paper was possible by virtue of all the support given by these great colleagues around me.

Lastly but importantly, I want to have my greatest thanks to my dear family and friends for their unconditional love and support throughout the happy and difficult times. I could have come through this journey owing to their presence in my life.

Table of Contents

Table Captions

`

Table of Figures

Abbreviations

AFM	Atomic Force Microscopy
Ala/A	Alanine
Arg/R	Arginine
Asp/D	Aspartic Acid
AMP	Antimicrobial Peptide
ATR	Attenuated Total Reflectance
Au	Gold
Ca^{+2}	Calcium ion
$CaCl_2$	Calcium Chloride
$CaCO_3$	Calcium Carbonate
CO_3^{-2}	Carbonate ion
CD	Circular Dichroism
CP	Cement Protein
Cys/C	Cysteine
DLS	Dynamic Light Scattering
E. coli	*Escherichia coli*
FECO	Fringes of Equal Chromatic Order
FTIR	Fourier Transform Infrared Spectroscopy
Glu/E	Glutamic Acid

Gly/G	Glycine
HCl	Hydrochloric Acid
His/H	Histidine
LSPR	Localized Surface Plasmon Resonance
Lys/K	Lysine
MUA	11-Mercaptoundecanoic acid
MALDI-TOF	Matrix-assisted Laser Desorption/ Ionization Time of Flight Mass Spectrometry
MHB	Müller-Hinton broth
MIC	Minimal Inhibitory Concentration
MrCP19	*Megabalanus rosa* Cement Protein with 19 kDa
MrCP20	*Megabalanus rosa* Cement Protein with 20 kDa
MWCO	Molecular Weight Cut-Off
MUA	11-mercaptoundecanoic acid
MUAM	11-mercaptoundecylamine
NaOH	Sodium Hydroxide
$(NH_4)_2CO_3$	Ammonium Carbonate
Ni-NTA	Nickel-Nitrilotriacetic Acid
NPS	Nanoplasmonic Sensing
pI	Isoelectric Point
PZC	Point of Zero Charge
QCM-D	Quartz Crystal Microbalance with Dissipation monitoring
SDS-PAGE	Sodium Dodecyl Sulfate Polyacrylamide Gel Electrophoresis

SEC	Size Exclusion Chromatography
SEM	Scanning Electron Microscopy
Ser/S	Serine
SFA	Surface Force Apparatus
TEM	Transmission Electron Microscopy
Thr/T	Threonine
UM	11-mercaptoundecanol
Val/V	Valine
XPS	X-ray photoelectron spectrometer
XRD	X-ray Diffraction

Abstract

Barnacles adhere themselves robustly and permanently to diverse underwater substrates through strong interactions of a multi-protein complex layer called the "cement". However, the intermolecular interactions responsible for the strong adhesive properties of the barnacle cement remains poorly understood. A central hypothesis of this thesis is that underwater properties of the cement complex are intimately linked to the molecular characteristics of cement proteins (CPs) forming the cement complex.

Previous studies have shown that the cement is made of amyloid-like nanofibrils that may contribute to adhesion. However, the protein responsible for the formation of these nanofibrils remain unknown. In this study, the nanoscale morphological features of recombinant cement proteins (CPs) from the barnacle *Megabalanus rosa* (MrCP19 and MrCP20, with the numbers indicating molecular weight of 19 kDa and 20 kDa respectively) were characterized by Circular Dichroism (CD) measurement, Thioflavin T (ThT) assay, Atomic Force Microscopy (AFM), and Transmission Electron Microscopy (TEM), suggesting the potential to form nano-fibrillar structures under certain conditions. Based on the proteins' primary structure and surface morphology, mechanical, biochemical, and antimicrobial studies were conducted to understand the unique roles of these interfacial proteins on barnacle growth and surface attachment process, for instance biomineralization and biodegradation control. Measurements using Surface Force Apparatus (SFA) and Quartz Crystal Microbalance with Dissipation monitoring (QCM-D) illustrated that electrostatic interactions play a key role in surface adsorption and adhesion of MrCP19 and MrCP20. In addition, the mutual influence of barnacle base plate growth (calcium carbonate mineralization) and the adjacent cement protein MrCP20 fibrillation was investigated using self-assembled monolayer (SAM) functionalized gold surfaces, Raman spectroscopy, QCM-D, X-ray photoelectron spectrometer (XPS), and Attenuated total reflectance Fourier transform infrared spectroscopy (ATR-FTIR). Concurrently, the influence of the external substrate adjacent cement protein MrCP19 on bacteria cells which are present in biofilm on underwater surfaces in marine environment was demonstrated using different microbiology tests including zone of inhibition test, Minimum inhibitory concentration (MIC) assay, TEM, fluorescence study, and so on. More interestingly, an intriguing hypothesis regarding amyloid fibrillation process and antimicrobial activity was suggested.

Based on these preliminary examinations, the two interfacial CPs showed distinctive potential responsibilities on barnacle settlement not only with its adhesion but also with other functional roles at the interfaces. This work will improve our knowledge about individual contributions of MrCP19 and MrCP20 in cement complex and hence in overall underwater adhesion capacity of barnacles. In this regard, the thesis aims at providing molecular guidelines towards the development of CPs inspired polymeric (peptide or protein based) mimics from this bio-adhesive molecular system.

Keywords: Barnacle cement proteins, Underwater adhesion, Protein conformation, Amyloid fiber, Fibril formation, Surface adsorption behavior, Surface adhesion energy, Calcium carbonate, Biomineralization, Antimicrobial activity

Chapter 1 Introduction

Barnacles are sessile organisms that colonize a wide range of underwater surfaces in various marine environments, resulting in the widespread issue of biofouling. In order to combat the tenacious underwater attachment, researchers have been developing specialized non-toxic antifouling surfaces, which has been challenging, in particular because the adhesion mechanisms of barnacles are still not well understood. The goal of this research is to understand the molecular mechanisms adopted by barnacles to strongly adhere to underwater substrates with their proteinaceous cement. Outcomes of this research will guide the development of wet-resistant adhesives with significant potential for biomedical applications.

1.1 Problem Statement and Hypothesis

Barnacles are unique sessile crustaceans, recognized as the dominant hard shelled marine biofoulers. Combined with their gregarious nature, barnacles attach themselves to diverse foreign materials such as hull of ship, rocks, bivalve shells, and even on other barnacles' shells.[1] Their underwater adhesion is so robust that external forces cannot detach the adhesive joint without breaking the calcified shells of barnacles. Therefore, colonization or biofouling by barnacles damages ships' hulls and port infrastructures, causing serious economic problems especially to the shipping industry.[2] It also creates high friction between water and the hulls, thus reducing the ship's efficiency and increasing fuel consumption.[3–6]

To mitigate these problems, antifouling coatings have been designed for underwater surfaces, which either showed unsuccessful results or were toxic to the marine ecosystem.[4] In the past decade, molecular strategies used by biofouling organisms for underwater adhesion have been studied in greater details in order to overcome the drawbacks of existing antifouling coatings. Indeed, a wide range of living organisms exhibit underwater adhesion[7] in a way that is still unmatched with their synthetic counterparts. Therefore, it is important to understand barnacle adhesion in order to improve strategies to combat fouling.

Biological adhesion has been studied successfully in mussels, which aggressively attach themselves to solid surfaces via protein-based filaments called the "byssus".[8–10] In contrast to the now well-established adhesive strategies of mussel adhesive proteins, very little is known about the barnacle holdfast system. Understanding the adhesion mechanism of barnacles at the same level of mussel adhesion will contribute to the development of eco-friendly antifouling coatings.

This project uses the common acorn barnacle *Megabalanus rosa* to study its molecular mechanism of underwater attachment. It exhibits unique adhesion by its multi-protein complex, "cement", which is secreted and cured underneath the base plate. As of date, amyloid fibrils, the mainly observed structure from the native cured cement, have been prominently believed to involve in the underwater adhesion.[11] Meanwhile, Kamino (2013)[12] has identified 5 unique proteins composing the cement and suggested their possible locations in the cement based on amino acid compositions and investigations from adsorption studies on various substrates. It has been suggested that hydrophobic MrCP100 and MrCP52 form the bulk of the cement, hydrophilic MrCP20 and MrCP68 constitute the interface between barnacle base plate and the cement, whereas hydrophilic MrCP19 is located at the bottom of the cement gland interacting with the foreign substrate. So far, experimental evidence confirming these proposed interactions is still sparse. The structure of the listed cement proteins in solution, their self-assembly (fibrillization) in the final cured state on the surface, and specific functional roles of each protein have not been fully clarified.

The current project specifically focuses on MrCP19 and MrCP20 that have been suggested to be located in the interfacial layers of the cement to perform the critical role of surface interaction. In addition, both proteins are known to be soluble after recombinant expression [13,14], thereby facilitating in-depth characterization by surface sensitive techniques to elucidate the hypothesis. This work aims to correlate the primary structure of these cement proteins with their three-dimensional conformation and their resulting behavior on distinct model surfaces. Furthermore, additional potential functional roles of these proteins will be discussed, which will be necessary for surface adhesion and the barnacle growth process. Consequently, these results will contribute to current knowledge of adhesive strategies of barnacles, and therefore provide bioinspired solutions to engineer synthetic yet biocompatible adhesives that are durable in wet environment, which is a longstanding issue in the biomedical field.[12,15]

1.2 Objectives and Scope

A better understanding of barnacle adhesion at molecular level is targeted and will be achieved by characterizing the two interfacial cement proteins, MrCP19 and MrCP20. Molecular level observations suggesting different functions of these recombinant cement proteins will demonstrate the physiology and evaluate the adhesive process of barnacles. The specific research goals of the project are the following:

i. Identify the morphology and surface characteristic of two soluble cement proteins MrCP19 and MrCP20 under acidic and basic pH conditions. This will be useful to gain knowledge on their individual properties on surfaces.

ii. Compare and analyze the nano-scale adsorption behavior and adhesion energy of MrCP19 and MrCP20 on mica and metal oxide surfaces mimicking the chemical environment of the immersed substrates for the above tested conditions.

iii. Examine molecular-level coordination of MrCP20 with calcium carbonate to understand the protein's functional role participating in base plate biomineralization, and ultimately its contribution to regulating the growth of barnacles' shells.

iv. Investigate the potential anti-microbial activity of MrCP19 on gram-positive and gram-negative bacteria. These results will elucidate one of the additional role of the cement, namely how it prevents bacterial degradation in the marine environment.

The thesis comprises seven Chapters to address the objectives above. Chapter 1 provides the basis and motivation for this PhD, and Chapter 2 introduces a comprehensive background of barnacle cement proteins. The objectives **i - iv** will be presenting in Chapter 3-6, respectively, with the conclusion in Chapter 7.

1.3 Expected Outcomes

The current study characterizes recombinant cement proteins MrCP19 and MrCP20 to enhance the overall understanding of underwater adhesion of barnacles. Different observations on their structural behavior, surface morphology, surface interaction energy, mutual influence on biomineralization, and antimicrobial function will be performed to attain the above listed objectives, and the expected outcomes are outlined as follows:

i. Characterization of structural features of MrCP19 and MrCP20 on surfaces, based on understanding of their primary structure and conformational changes upon surface attachment. Biophysical analysis of the proteins in solution should be precedented to demonstrate critical process of surface adsorption.

ii. Identification of intermolecular forces controlling surface adhesion. Interaction of MrCP19 and MrCP20 on surfaces will be investigated, and plausible hypotheses for inter-protein interactions will be demonstrated. Adhesion is not only attributed to surface attachment but also to cohesive interactions of the bulk material.

iii. Identification of structurally constrained domains of MrCP19 and MrCP20 to be used as motifs for controlled self-assembly into fibrils. Subsequently the generated nanofibrils will be investigated for surface adhesion measurements in order to help understand the role of nanofibrils observed on surfaces of the native cement.

iv. The role of MrCP20 in regulating mineralization of the shell will be studies to bring insights into the protein's multifunctional role and understand barnacle's strategies at the interface.

v. Bacterial membrane disruption mechanism of MrCP19 with regard to its putative fibrillation behavior into amyloid-like nanofibrils and possible applications will be discussed.

References

1. Dürr, S. & Thomason, J. C. *Biofouling*. (John Wiley & Sons, 2009).

2. Sangeetha, R., Kumar, R., Doble, M. & Venkatesan, R. Barnacle cement: An etchant for stainless steel 316L? *Colloids and Surfaces B: Biointerfaces* **79,** 524–530 (2010).

3. Chambers, L. D., Stokes, K. R., Walsh, F. C. & Wood, R. J. Modern approaches to marine antifouling coatings. *Surface and Coatings Technology* **201,** 3642–3652 (2006).

4. Flemming, H.-C., Murthy, P. S., Venkatesan, R. & Cooksey, K. *Marine and industrial biofouling*. **333,** (Springer, 2009).

5. Schultz, M. P., Bendick, J. A., Holm, E. R. & Hertel, W. M. Economic impact of biofouling on a naval surface ship. *Biofouling* **27,** 87–98 (2011).

6. Rosenhahn, A., Ederth, T. & Pettitt, M. E. Advanced nanostructures for the control of biofouling: the FP6 EU integrated project AMBIO. *Biointerphases* **3,** IR1–IR5 (2008).

7. Flammang, P., Santos, R., Aldred, N. & Gorb, S. *Biological and biomimetic adhesives: challenges and opportunities*. (Royal Society of Chemistry, 2013).

8. Lee, H., Dellatore, S. M., Miller, W. M. & Messersmith, P. B. Mussel-inspired surface chemistry for multifunctional coatings. *science* **318,** 426–430 (2007).

9. Waite, J. H. Mussel power. *Nature materials* **7,** 8–9 (2008).

10. Waite, J. H., Andersen, N. H., Jewhurst, S. & Sun, C. Mussel adhesion: finding the tricks worth mimicking. *The journal of adhesion* **81,** 297–317 (2005).

11. Liu, X. Amyloid fibril aggregation: An insight into the underwater adhesion of barnacle cement. *Biochemical and Biophysical Research Communications* 6 (2017).

12. Kamino, K. Mini-review: barnacle adhesives and adhesion. *Biofouling* **29,** 735–749 (2013).

13. Mori, Y., Urushida, Y., Nakano, M., Uchiyama, S. & Kamino, K. Calcitespecific coupling protein in barnacle underwater cement. *FEBS Journal* 11 (2007).

14. Kamino, K. Novel barnacle underwater adhesive protein is a charged amino acid-rich protein constituted by a Cys-rich repetitive sequence. 5 (2001).

15. Shivapooja, P., Wang, Q., Orihuela, B., Rittschof, D., López, G. P. & Zhao, X. Bioinspired surfaces with dynamic topography for active control of biofouling. *Advanced Materials* **25,** 1430–1434 (2013).

Chapter 2 Literature Review

Barnacles are dominant fouling organisms found throughout the world's oceans and seas. Extensive research on barnacles has been carried out with respect to their attachment to foreign substrates, which always occurs underwater. Previous studies have examined the barnacles' cement curing mechanisms from their cyprid larvae stage to the permanent adhesive in the adult stage. This Chapter discusses investigations on biochemical and sequencing analyses of barnacle cement, the mechanics of adhesion at the macroscopic level, surface spectroscopy of the barnacle cement, and identification of nanoscale structural features of the barnacle cement.

2.1 Barnacles

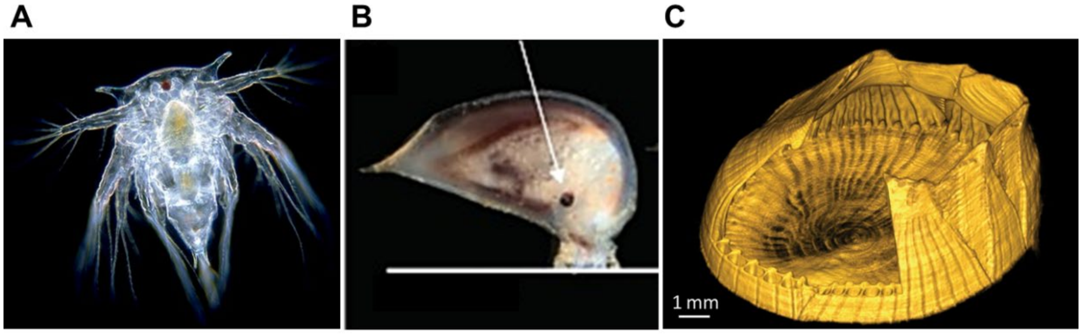

Figure 2.1 Acorn barnacles at different stages of their lifecycle starting with **(A)** nauplius stage (Taken from Wim Van Egmond 'Living on the Edge' 1999), **(B)** cyprid larva stage,[1] and **(C)** juvenile to adult barnacle.[2]

The barnacle's lifecycle begins with the pelagic suspension-feeding nauplius stage. Depending on the larva's perception of surrounding habitat condition and proper diet, it undergoes metamorphosis to the cyprid at appropriate timing for ideal age, size, and lipid reserves.[3,4] When the non-feeding cyprid larva stage is reached, they start to explore potential surfaces with modified antennules, depositing footprints.[5,6] Once the cyprids successfully locate a conducive surface to settle down, they undergo metamorphosis into a juvenile barnacle changing its shape within 6-10 hours.[7–17] The juvenile grows into an adult by expanding its base and side plates with molting and calcification.[1]

Adhesion is crucial for the survival of barnacles during the transition from cyprid larvae to juvenile state, and necessary to maintain permanent attachment as the juvenile grows into an adult barnacle.[18] As a result many studies have been done on barnacles, starting from their premature state.[8,15,19,20] Adult acorn barnacles are protected by a hard, volcano-shaped calcareous shell protecting their soft body tissue. Every few days they undergo periodic molts, where the base plate laterally extending while the outer shell expands in height by calcification at the bottom edges adjoining the base.[21,22] Organic compounds or cellular tissue within the parietal and base plates have been suggested to play roles in osmoregulation, biomineralization, and interlocking system at the growing boundary.[23–25] Most of barnacle exoskeleton is known to consist of calcite and small percentage (less than 3 %) of organic material.[22,26,27] Calcite crystals are heterogeneous in their size, shape, and orientation, resulting in a biomineralized structure resistant against mechanical fracture.[27–29] The adhesive secreted underneath the base plate allows the barnacles to firmly and permanently adhere to foreign substrates.

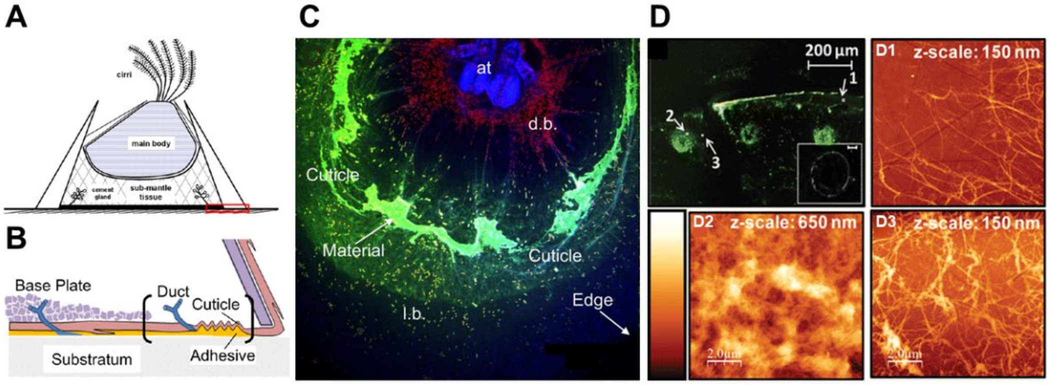

Figure 2.2 Barnacle structure in different views. **(A)** Cross-sectional diagram of an adult acorn barnacle with **(B)** the active growing region of the adhesive interface enlarged.[30] **(C)** Confocal microscope images of adhesive interface of newly metamorphosed juveniles barnacles completing their settlement and metamorphosis.[17] **(D)** Fluorescence micrograph of the adhesive remaining on the substrate from a barnacle that secreted fluorescent material from newly formed capillaries (arc) as well as previously formed capillaries (circular spots), and **(D1-D3)** AFM topography scans taken from corresponding regions (1-3) labeled in **D**.[2]

The development of the cement interface under the base plate involves multiple steps, which includes adhesive glue delivery to the perimeter of the base by radial canals located at the base plate.[31] The deposition and curing processes of the adhesive interface are protected by cuticular tissues and newly formed calcite in the base plate. It has been suggested that different regions in the horizontal plane exhibit different compositions, structures, and anti-bacterial activities.[17,32] Aldred *et al.*[6] also conducted observations on the adhesives released from the cyprid stage. They revealed that dual-component adhesives do not merge into one continuous plaque nor mix homogeneously but remain separate and interact with surfaces with different chemistry. Research on the process of adhering, curing, molting, and mineralization are still ongoing.

2.2 Barnacle cement proteins

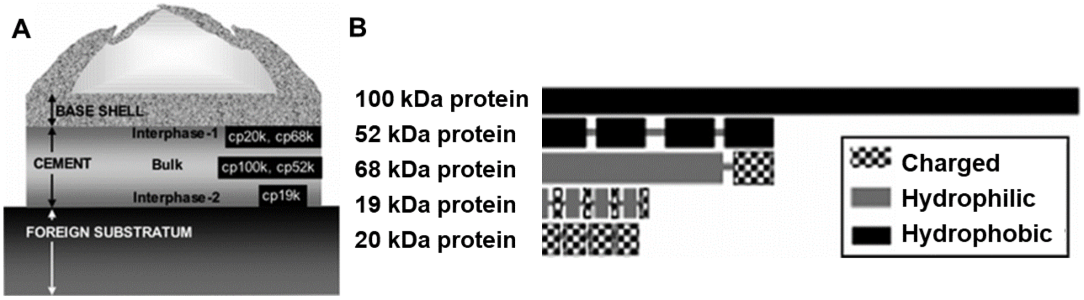

Figure 2.3 (A) Barnacle cement protein complex indicated with possible functions and **(B)** schematic illustration of cement protein primary structures with relative length indicating the molecular weight of each protein.[33]

Barnacles' firm attachment can be explained by the secretion of a multi-protein complex "cement", followed by rapid curing of this adhesive. Kamino[33] identified at least 5 proteins from the cured cement of adult barnacle *Megabalanus rosa*, namely MrCP19, MrCP20, MrCP52, MrCP68, and MrCP100, with the numbers indicating the molecular weight (MW) of each protein. He proposed the spatial location of these proteins within the complex through adsorption studies of the proteins on various substrates such as calcite, gold, glass and polystyrene.[34] **Figure 2.3** shows the putative location of cement proteins and illustration of their sequence design. According to his hypothesis, hydrophobic MrCP100 and MrCP52 are located in the bulk of the cement, hydrophilic MrCP20 and MrCP68 exist at the interface between barnacle base plate and bulk cement, and hydrophilic MrCP19 forms the layer that interacts with the external substrate. Since MrCP19 and MrCP20 are the proteins assumed to be in the interfacial regions, there is a strong interest to investigate their functional role in the cement complex.

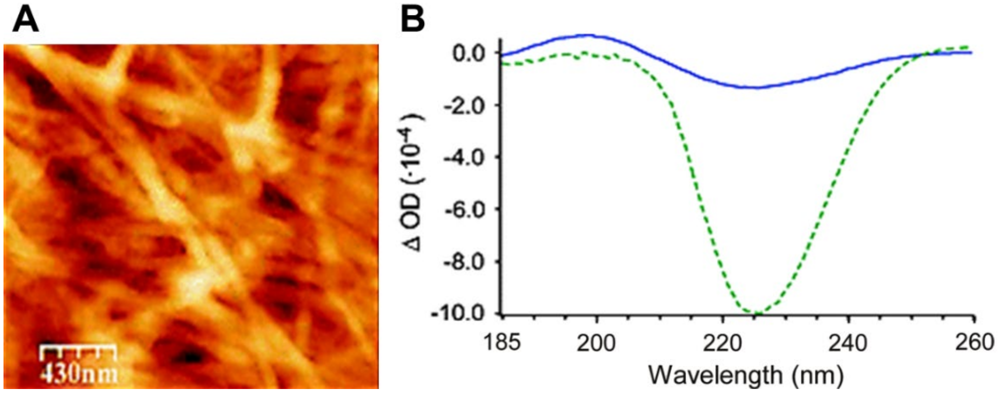

Figure 2.4 (A) AFM topography from the base plate region of *Balanus amphitrite* and **(B)** CD spectra of the bulk cement from the same barnacle originally settled as cyprids on quartz and CaF2 (green, dashed) and "secondary cement" (blue, solid; referring to cement used for reattachment).[35]

Studies by surface spectroscopy and nano-scale structural investigations of the bulk barnacle cement[35–38] from the *Balanus amphitrite* species have suggested that it partially forms highly insoluble amyloid-like nanofibrils beneath the base plate. (**Figure 2.4**) Amyloids are fibrillar proteins with a cross β-sheet structure in which individual β-strands are arranged in a perpendicular direction to the long axis of the fiber, connected through a dense C=O and N-H hydrogen-bonding network over thousands of molecular units.[39–43] Mostly, two or more protofilaments twist around each other to form the fibril (**Figure 2.5**). Amyloid fibrils are identified by X-ray diffraction pattern comprised of one longitudinal and one transverse set of diffraction lines. Strong, sharp diffraction signals at 4.7 Å and 10 Å correspond to hydrogen bonded interstrand distance and β-sheets stacking distance, respectively.[44–47] There are labile amyloid-like fibrils as well as stable and irreversible ones, which are formed from Gly (G), Ser (S), and Tyr (Y) rich low-complexity domains.[48–50] Such fibrillar structures are considered to be highly advantageous for interfacial adhesion on account of their tolerance to environmental deterioration,[43] self-healing from self-polymerization,[51] and large fibrous surface area.[35,52] Also their mechanical benefits are well-established, with strong cohesion arising from intermolecular β-sheet structures and adhesive residues external to the amyloid core providing adhesion.[43,53]

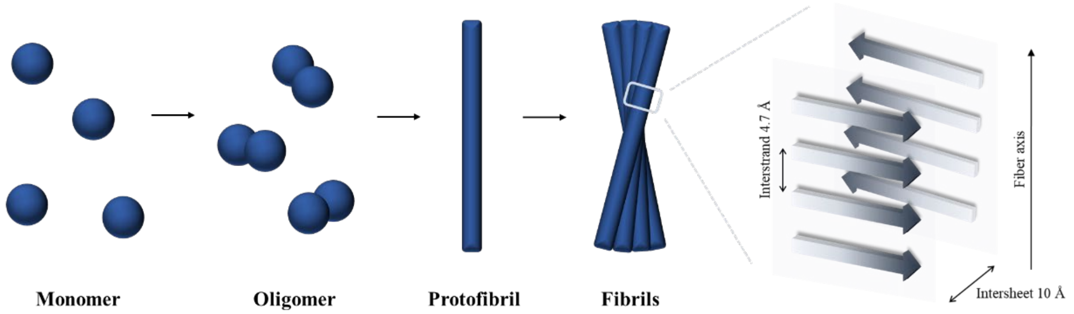

Figure 2.5 A hierarchical illustration of amyloid fibrils at structural level. Generic amyloid fibril structure is defined by a cross-β structure, where β-strands are aligned perpendicular to the fibril axis with the inter-strand distance of approximately 4.7 Å, and β-sheets are parallel to the same axis with the inter-sheet distance of approximately 10 Å.

The presence of amyloid-like fibrils has been established in other adhesive proteins in living organisms, including curli and chaplins from bacteria,[54] hydrophobins of fungi,[43] chorion found in protective membranes of insect and fish eggs,[55] and other adhesives from algae and marine parasites.[43,55] Therefore, studies have been undertaken to identify such amyloid-like conformations in the barnacle cement, based on the hypothesis that barnacles might also share similar adhesion principles. In this regard, amyloid-like short sequences have been identified in MrCP52,[56] whereas MrCP20 has been shown to self-assemble into nanofibrils on calcite surfaces at a specific crystallographic directions, suggesting geometric binding of MrCP20 with calcite.[57] Furthermore, different experimental methods have been used to establish the presence of these nano-fibrils in barnacle cement, including staining assay for cross-beta structure of amyloids,[37] Scanning Electron Microscopy (SEM),[58] Attenuated Total Reflectance Fourier Transform Infrared Spectroscopy (ATR-FTIR),[35,36,38] UV Circular Dichroism (CD),[35] and Atomic Force Microscopy (AFM).[37,59]

Although these reports suggest that the overall cement comprises of cross-β structure forming amyloid nanofibrils, how the initially soluble cement proteins assemble into these fibrils remains unknown. In addition, there is little understanding linking amyloid fibrils of cement proteins with their adhesive propensity.

2.3 Sequence features of MrCPs

Among the five proteins composing barnacle cement layer as shown in **Figure 2.3**, MrCP19 and MrCP20 have been suggested in various studies as the most plausible cement proteins for surface adhesion studies. These proteins are also convenient to work with because they express relatively well in bacteria likely due to their low molecular weight and high solubility. The sequences of the proteins are shown in **Figure 2.6**, as obtained from Peptide Property Calculator (Bio-Synthesis, Inc.). MrCP20 is less hydrophobic at both acidic and neutral pH than MrCP19, possessing more charged (both acidic and basic) components and less hydrophobic content. The comparison is shown in **Table 2.1**.

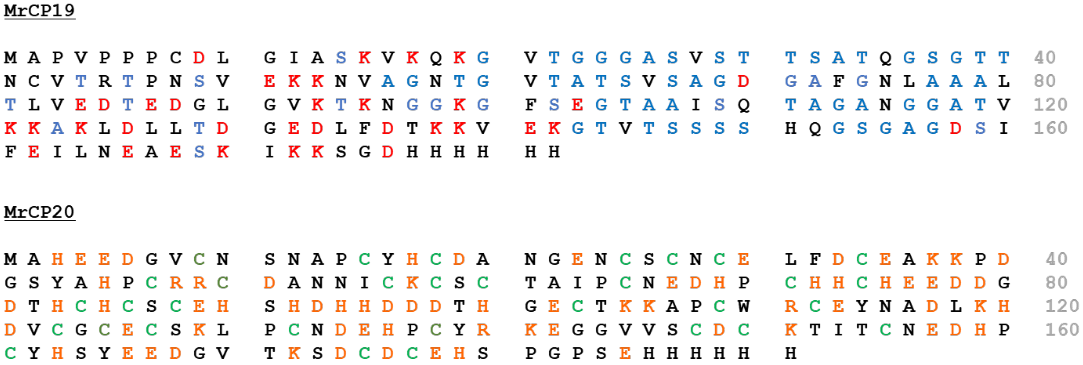

```
MrCP19

M A P V P P P C D L   G I A S K V K Q K G   V T G G G A S V S T   T S A T Q G S G T T   40
N C V T R T P N S V   E K K N V A G N T G   V T A T S V S A G D   G A F G N L A A A L   80
T L V E D T E D G L   G V K T K N G G K G   F S E G T A A I S Q   T A G A N G G A T V   120
K K A K L D L L T D   G E D L F D T K K V   E K G T V T S S S S   H Q G S G A G D S I   160
F E I L N E A E S K   I K K S G D H H H H   H H

MrCP20

M A H E E D G V C N   S N A P C Y H C D A   N G E N C S C N C E   L F D C E A K K P D   40
G S Y A H P C R R C   D A N N I C K C S C   T A I P C N E D H P   C H H C H E E D D G   80
D T H C H C S C E H   S H D H H D D D T H   G E C T K K A P C W   R C E Y N A D L K H   120
D V C G C E C S K L   P C N D E H P C Y R   K E G G V V S C D C   K T I T C N E D H P   160
C Y H S Y E E D G V   T K S D C D C E H S   P G P S E H H H H H   H
```

Figure 2.6 Amino acid sequence of the two cement proteins from *Megabalanus rosa*, MrCP19 and MrCP20. MrCP19 is enriched in Ser (S), Thr (T), Gly (G), Ala (A) amino acids (blue), as well as Lys (K), Asp (D), and Glu (E) (red). MrCP20 is more abundant in charged residues (orange) and Cys (green).

Table 2.1 Amino acid composition and primary structure analysis of the two cement proteins from *Megabalanus rosa,* MrCP19 and MrCP20.

	pI	**Amino Acids**	**MW (kDa)**	**Positive (Arg + Lys)**	**Negative (Asp + Glu)**	**Hydrophobic Residues**	**Theoretical Net Charge**
MrCP19	6.89	182	18.1	18	20	85	-5 (pH 8.3) +18 (pH3.6)
MrCP20	5.05	191	21.4	15	40	44	-50 (pH 8.3) +25 (pH3.6)

The primary sequence of MrCP19 is abundant with Ser (S), Thr (T), Gly (G), Ala (A), and Lys (K), Asp (D), Glu (E) with approximate molecular weight of 18.1 kDa. The repetitive alternating pattern of flexible residues and charged residues of MrCP19 provides distinct polymerization behavior of the protein.[60] Hydroxyl groups of Ser and Thr are claimed to play significant role on water molecules displacement on surfaces which is necessary as priming process followed by coupling process.[61,62] Ala and/or methyl group of Thr of a relevant antifreeze protein are known to bind to the ice nucleus in several organisms.[63–65] The aforementioned amino acids comprise about two thirds of the total amino acids of MrCP19, which would be useful to interact with diverse foreign substratum *via* hydrogen bonding, electrostatic and hydrophobic interactions.[66] The biased amino acid compositions were well conserved from three barnacle species CP19, and it may indicate these common amino acid residues can represent a new biological adhesion mechanism, different from mussel underwater attachment which is highly related to post-translational modified amino acids.[67–69]

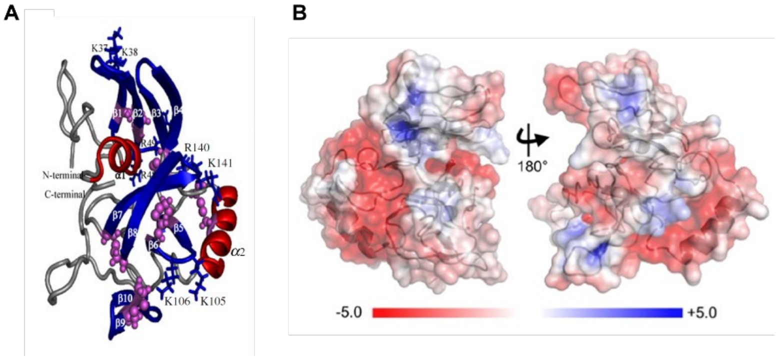

Figure 2.7 (**A**) Tertiary structure of MrCP20 in solution with disulfide linkages (pink spheres), α-helices (red) and β-sheets (blue).[70] (**B**) Surface representation of calculated electrostatic potential with the colors represent −5 kT/e (red) to +5 kT/e (blue).[71]

MrCP20 with a MW of 21.4 kDa, is hydrophilic and enriched with charged residues as well as Cys (C) (17.3%). Out of 32 Cys residues, only 12 of them are oxidized into disulfide bonds (**Figure 2.7**).[34,70,72,73] The remaining free thiols can contribute to other types of intermolecular interactions possibly for barnacle shell adhesion or biomineralization. Pro residues are known to disrupt β-sheets incapable of hydrogen bonding and thereby destabilize tertiary structures of globular proteins.[74] Pro residues in MrCP20 are often distributed next to oxidized Cys residues, suggesting adjacent disulfide bonds' mitigation and stabilization effect. NMR analysis observed 6 intramolecular disulfide bonds, which helps to compensate for poor hydrophobic core formation in the protein structure. The abundance of Cys in MrCP20 is more essential for the intramolecular structure than for the surface function.[18] The rigid structure improved by intramolecular disulfide bonds are also observable from extracellular small protein compounds.[75–77] This structural dependency generally displays functional specificity, adsorbing to limited materials namely calcite and metal oxides but not to glass and synthetic polymers.[34,78]

2.4 Plausible Surface functions of MrCP20 and MrCP19

2.4.1 Surface Interactions of Barnacle Cement

Beside biochemical investigations, barnacles' adhesive strength has been studied *in vitro* to understand their adhesion mechanisms at the macroscopic level. Various antifouling surfaces have been developed to minimize the adhesion of fouling organisms, including barnacles, and facilitate macroscopic adhesive tests using shear and tension tests.[79] Studies to improve antifouling behavior of polymers revealed that a combination of surface energy, mechanical properties such as elastic modulus or friction coefficient,[80–83] and glass transition temperature[84,85] affects the adhesion process. Phenomenological studies have been carried out to elucidate the role of environmental conditions as well as mechanical and physio-chemical properties of antifouling coatings on adhesion strength.[86–90] Efforts have been directed to understand the adhesion strength of barnacles on solid substrates using fracture mechanics concepts, by conducting "pseudo barnacle" tests, such as tension measurement on different coatings.[79,91–95] However, there is lack of information on specific substrates preference of barnacles. Likewise, fundamental understanding on the correlation between macroscopic adhesion strength and molecular level adsorption of barnacle adhesive is sparely understood. Analyzing the adhesion strength of the proteins of interest should provide a better understanding behind barnacle adhesion at both the micro- and macroscopic level.

2.4.2 Additional Plausible Functions of MrCP20

2.4.2.1 Biomineralization regulation by functionalized surfaces

Crystal growth process of $CaCO_3$ has been widely studied because of its commercial relevance from construction industry to biomedical applications, as well as the environmental role of biomineralization in marine biology.[96–104] Nucleation events as the first step must involve long-range ordering of atoms and molecules, and self-assembled monolayers (SAMs) on gold substrates have been significantly used in order to test different surface parameters affecting the nucleation and growth, morphology, polymorphism of the crystals, and so on. The use of structured SAMs can discuss the quantitative control of crystal growth as well as orientational specificity for crystal nucleating faces.[105–110]

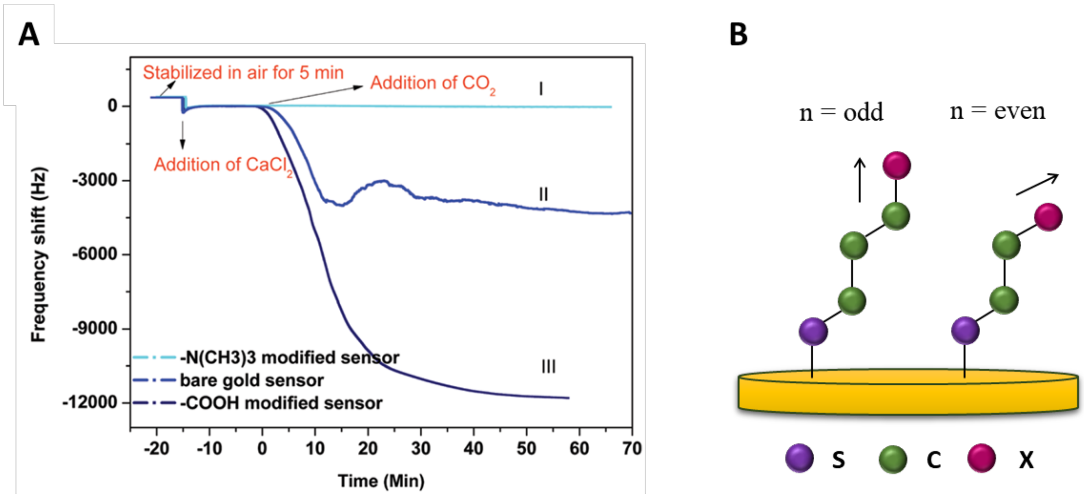

Figure 2.8 (**A**) Frequency shift of the QCM-D due to the crystallization of $CaCO_3$ on the -$N(CH_3)_3$, bare gold, and -COOH modified surfaces. Excess solid $(NH_4)_2CO_3$ was located aside the $CaCl_2$ solution to provide CO_2.[111] (**B**) Schematic illustration of odd and even chain

length alkyl thiols adsorbed on gold substrate, with the differences in the orientation of the terminal functional group X indicated with the arrows.

1. Composition of the functional groups exposed at the surface

Quantitative control of crystal growth was monitored by adjusting the ratio of two functional groups –$N(CH_3)_3$ and –COOH on alkyl thiol SAMs on gold surface (**Figure 2.8A**). The growth of $CaCO_3$ crystals was followed by QCM-D response due to the surface mass increase. No frequency shift was observed on the –$N(CH_3)_3$ modified surface attributed to excellent ability to inhibit the crystal growth. On the other hand, –COOH enhanced the surface crystallization compared to the bare gold surface, in quantity as well as in quality with higher stability and efficient saturation of the frequency shift. The higher ratio of –COOH on surface induced not only more crystals growth but also higher uniformity in size, morphology, and polymorphism.

2. Spatial orientation of the terminal functional groups

SAMs offer unique opportunities to understand self-organization, structure property, and various interfacial phenomenon. With variation of the chain length in either odd or even number while keeping the spacing of alkyl thiols constant, orientation of the terminal moiety is affected, which is one of well-known “odd-even” effects (**Figure 2.8B**).[112,113] For instance, carboxylic alkyl thiols with the odd-chain length (HS-C_7, C_{11}, C_{15}-COOH) templated the calcite growth from (01*l*) faces (*l* = 2-5), while even-chain length thiols (HS-C_{10}, C_{14}, C_{16}-COOH) had calcite crystals nucleated from the (11*l*) crystallographic planes. The ordered carboxylates on SAMs attract Ca^{2+} ions and induce the oriented bonding of subsequent carbonates, resulting in a fixed, highly controlled, and oriented growth of the crystals.[108,114]

2.4.2.2 Biomineralization regulation by amino acids in solution

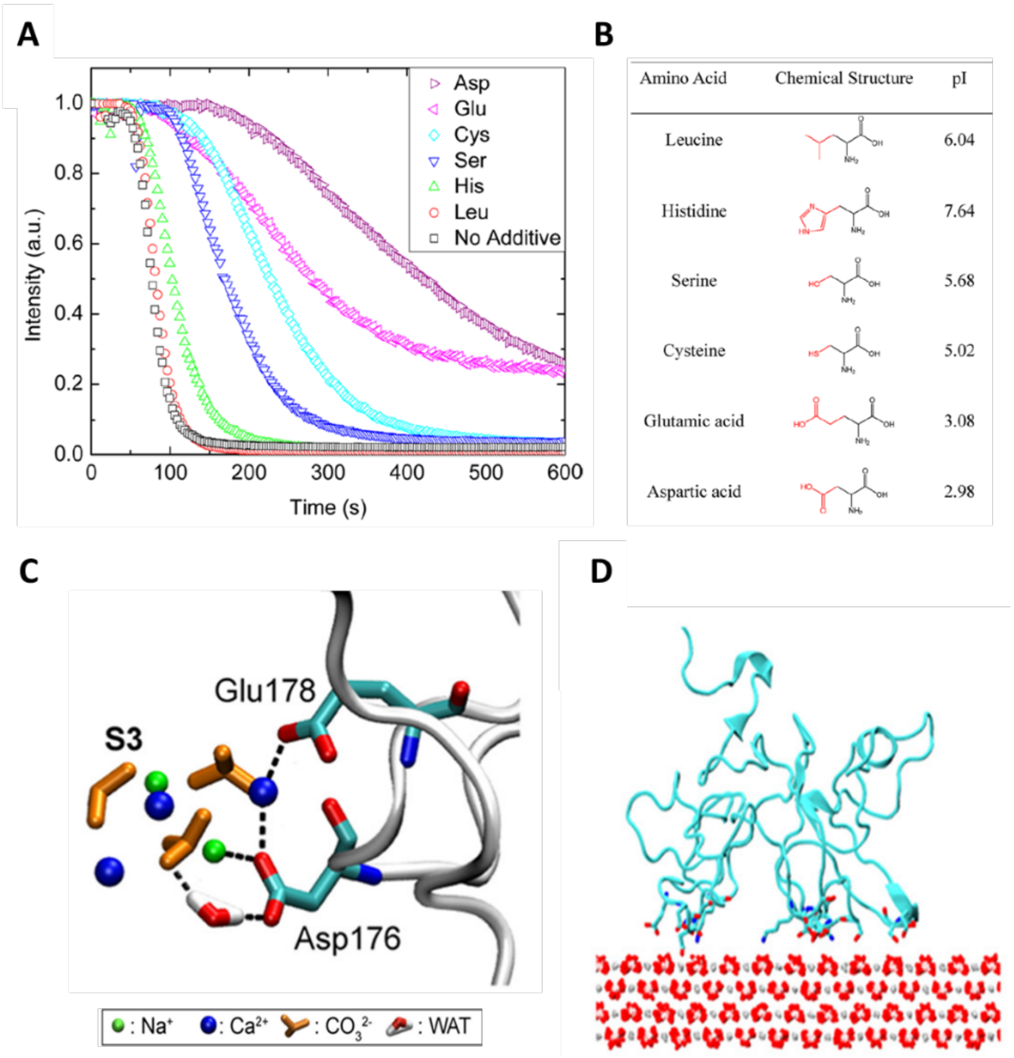

Amino Acid	Chemical Structure	pI
Leucine		6.04
Histidine		7.64
Serine		5.68
Cysteine		5.02
Glutamic acid		3.08
Aspartic acid		2.98

Figure 2.9 (**A**) Light transmission curve for the $CaCO_3$ crystallization in the presence of different amino acids at an amino acid-to-calcium ratio of 2:1, and (**B**) Chemical structure and isoelectric point (pI) of amino acids used. The amino acids' side-chain acidity is directly related to the greater ability to inhibit crystal growth.[115] (**C**) Ion–residue interactions shown with MrCP20 in a white cartoon, interacting residues in cyan sticks, the interactions in dashed lines.[71] (**D**) MrCP20 adsorption onto the $\{10\bar{1}4\}$ face of a calcite surface. MrCP20 is displayed as a cartoon and the interacting protein residues (cyan) and calcite surface are in stick representation.[71]

Nature often uses organic compounds for the morphology control and apposite polymorph selection of $CaCO_3$ to design biologically structured crystal habits which is beneficial for mechanical properties in material such as, eggshells, antlers, and other sea creatures' shells.[116–119] Recent studies have extracted peptides from the invertebrates' shells, and shown that acidic amino acids bind to calcium ions and calcite crystal surfaces, retarding their growth.[120–125] A light transmission measurement following crystal growth in the presence of different amino acids discovered that the degree of side chain acidity is directly related to the inhibitory efficiency of the additives as well as vaterite stabilization, due to interaction between the additives and the crystal faces (**Figure 2.9A-B**).[115]

The influence of charged domains of MrCP20 on dynamic nature of the protein was investigated, including calcite base coupling behavior. Salt bridges observed by NMR and MD provide dynamic flexibility of protein conformation via stabilizing interactions between different domains and loops of MrCP20.[70] The coordination of the charged residues with Ca^{2+} and CO_3^{2-} ions through electrostatic or water mediated interactions was demonstrated (**Figure 2.9C**). The alternatively layered charge distribution of the solutes surrounding MrCP20 affects the $CaCO_3$ network. NMR analysis on MrCP20 in the presence of $CaCO_3$ confirmed that Asp (D) is critical and that the mineral ions form clusters around the acidic residue rich domains.[126] MrCP20 adsorption onto the $\{10\bar{1}4\}$ calcite crystal face was studied in simulation (**Figure 2.9D**). Conformational lability of MrCP20 upon calcite surface coupling is aided by disulfide bridges being distant from the residues interacting with the mineral surface.[71]

2.4.2.3 Potential link between calcite interaction and fibrillation

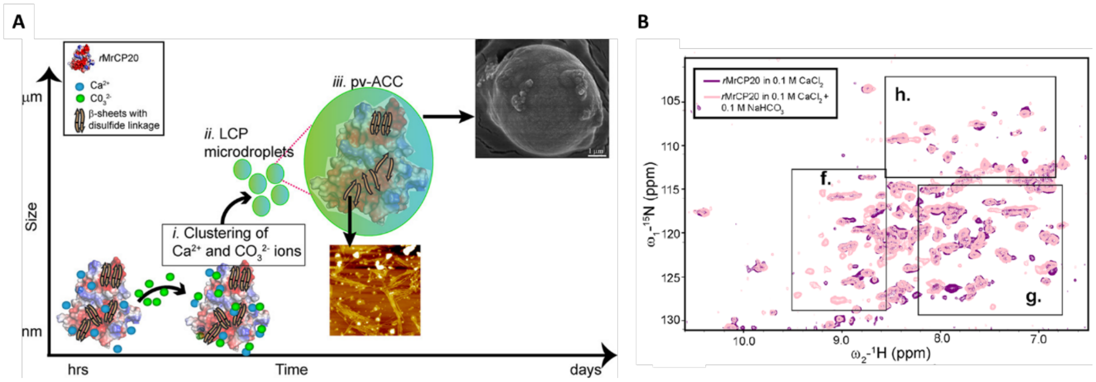

Figure 2.10 (**A**) Model illustrating the steps involved in MrCP20-mediated vaterite crystallization. (i) Domains rich in acidic residues of MrCP20 capture inorganic ions that aggregate into (ii) liquid condensed phase (LCP) microdroplets. (iii) Inside the droplets, fibrillization of MrCP20 and the growth of cluster aggregates into proto-vaterite ACC take place simultaneously. (**B**) ^{1}H–^{15}N HSQC spectra of MrCP20 in 0.1 M $CaCl_2$ in the absence (purple) and in the presence (pink) of 0.1 M $NaHCO_3$.[126]

NMR analysis on MrCP20 structure upon interaction with $CaCO_3$ identified Cys (C) as the key amino acid showing significant chemical shift (**Figure 2.10**). The pH drops as nucleation proceeds, reducing intramolecular disulfide bonds, and therefore freeing thiols to provide the flexibility to β-sheets and facilitate cross-β fibrillization forming amyloid-like nanofibrils.[57,126–128] At the same time, water molecules near the amyloid fibrils have the countereffect on vaterite stabilization, which supports the discussion above.[46,129]

2.4.3 Additional Plausible Functions of MrCP19

2.4.3.1 Antimicrobial activity

Antimicrobial peptides (AMPs) are known to damage cell membranes and cause cell death by functioning as host-defense or host-offense components in many innate immune systems in plants, animals, and humans.[130] Like other biofouling organisms in the ocean, barnacles' larvae settle on various surface in response to natural product and biofilm stimuli. However, the role of biofilms in fostering or inhibiting barnacles' settlement is not clearly understood.[131–139] It has been known that barnacles' larvae settle on surfaces regardless of the biofilm state, and this behavior is usually encouraged by the presence of other barnacles, whose shells are also promoting biofilm formation.[7,8,13,140–143] Studies on characterizing biofilm communities on barnacle substrata and on their shell surfaces[139,144–146] have been carried out to establish the correlation between the bacteria and barnacles, but little is known with regard to their direct causal relationship.

Gohad *et al.*[15] have proposed that the larval adhesive secreted by barnacle cyprid contains lipids and phospho-proteins, and that the lipid phase may protect the nascent adhesive plaque from bacterial biodegradation. Aldred and colleagues[6] have also suggested that bacteria may be attracted to and excluded from the adhesive material underneath the barnacle base plate. Zardus *et al.*[145] have proposed that certain stage of settlement and metamorphosis for adhesion might be closely connected to the interaction with biofilms. Wahl and co-workers[17] have observed that the number of bacteria underneath the barnacle settlement changed throughout the process of settlement. Bacteria seemed to concentrate in specific regions under the base plate and then were annihilated during the last stages of settlement and metamorphosis.

These studies looking into the relationships between barnacles and biofilm on wet surfaces suggest specific, time-regulated interactions during initial attachment and subsequent growth.

However, which cement protein(s) may interact with biofilms and their respective mode of interactions remains unknown.

2.4.3.2 Potential link between antimicrobial and amyloid peptides

There have been suggestions that numerous AMPs such as bacteriocins,[147] temporins,[148] or proteins like lysozyme,[149] lactoferrin,[150] and eosinophil cationic protein[151] form amyloid-like structures. At the same time, a number of amyloid proteins are known to have membrane perturbing[152–155] or thinning abilities[155–162], by binding to the negatively charged cell membranes.[163,164] Because of the similarities in amino acid composition between amyloid-prone regions of proteins and AMPs, Torrent *et al.*[165] have proposed correlation between antimicrobial activity and amyloid propensity. He suggested that amyloid-prone regions of peptides and proteins with a mutation to adopt amphipathic structure may retain membrane-disrupting function as AMPs. Additionally, it has been hypothesized that amyloid and antimicrobial peptides may act against their targets through a similar mechanism.[166] Fibril formation directly on cellular membranes is known to cause local membrane damage,[167,168] and the idea was supported by other research as well.[169,170] These studies, together with evidences that barnacle cement proteins form amyloid-like nanofibrils, lead us to hypothesize that cement proteins also exhibit antimicrobial activity, which will be tested in this project.

References

1. Høeg, J. T., Maruzzo, D., Okano, K., Glenner, H. & Chan, B. K. K. Metamorphosis in Balanomorphan, Pedunculated, and Parasitic Barnacles: A Video-Based Analysis. *Integrative and Comparative Biology* **52,** 337–347 (2012).

2. Burden, D. K., Barlow, D. E., Spillmann, C. M., Orihuela, B., Rittschof, D., Everett, R. K. & Wahl, K. J. Barnacle Balanus amphitrite adheres by a stepwise cementing process. *Langmuir* **28,** 13364–13372 (2012).

3. Hentschel, B. T. & Emlet, R. B. METAMORPHOSIS OF BARNACLE NAUPLII: EFFECTS OF FOOD VARIABILITY AND A COMPARISON WITH AMPHIBIAN MODELS. **81,** 14 (2000).

4. Lang, W. H. *Larval Development of Shallow Water Barnacles of the Carolinas:(Cirripedia; Thoracica) with Keys to Naupliar Stages*. **55,** (Department of Commerce, National Oceanic and Atmospheric Administration …, 1979).

5. Maleschlijski, S., Bauer, S., Aldred, N., Clare, A. S. & Rosenhahn, A. Classification of the pre-settlement behaviour of barnacle cyprids. *Journal of The Royal Society Interface* **12,** 20141104 (2015).

6. Aldred, N., Gohad, N. V., Petrone, L., Orihuela, B., Liedberg, B., Ederth, T., Mount, A., Rittschof, D. & Clare, A. S. Confocal microscopy-based goniometry of barnacle cyprid permanent adhesive. *THE JOURNAL OF EXPERIMENTAL BIOLOGY* 4

7. Crisp, D. J. & Ryland, J. S. Influence of filming and of surface texture on the settlement of marine organisms. *Nature* **185,** 119–119 (1960).

8. Crisp, D. J., Meadows, P. S. & Brambell, F. W. R. Adsorbed layers: the stimulus to settlement in barnacles. *Proceedings of the Royal Society of London. Series B. Biological Sciences* **158,** 364–387 (1963).

9. Walker, G. A study of the cement apparatus of the cypris larva of the barnacle Balanus balanoides. *Marine Biology* **9,** 205–212 (1971).

10. Walker, G. The early development of the cement apparatus in the barnacle, Balanus balanoides (L.)(Crustacea: Cirripedia). *Journal of experimental marine Biology and Ecology* **12,** 305–314 (1973).

11. Yule, A. B. & Walker, G. Settlement of Balanus Balanoides: The Effect of Cyprid Antennular Secretion. *Journal of the Marine Biological Association of the United Kingdom* **65,** 707–712 (1985).

12. Mullineaux, L. S. & Butman, C. A. Initial contact, exploration and attachment of barnacle (Balanus amphitrite) cyprids settling in flow. *Marine Biology* **110,** 93–103 (1991).

13. Matsumura, K., Nagano, M. & Fusetani, N. Purification of a larval settlement-inducing protein complex (SIPC) of the barnacle, Balanus amphitrite. *Journal of Experimental Zoology* **281,** 12–20 (1998).

14. Aldred, N., Phang, I. Y., Conlan, S. L., Clare, A. S. & Vancso, G. J. The effects of a serine protease, Alcalase®, on the adhesives of barnacle cyprids (Balanus amphitrite). *Biofouling* **24,** 97–107 (2008).

15. Gohad, N. V., Aldred, N., Hartshorn, C. M., Jong Lee, Y., Cicerone, M. T., Orihuela, B., Clare, A. S., Rittschof, D. & Mount, A. S. Synergistic roles for lipids and proteins in the permanent adhesive of barnacle larvae. *Nat Commun* **5,** 4414 (2014).

16. Gohad, N. V., Aldred, N., Orihuela, B., Clare, A. S., Rittschof, D. & Mount, A. S. Observations on the settlement and cementation of barnacle (Balanus amphitrite) cyprid larvae after artificial exposure to noradrenaline and the locations of adrenergic-like receptors. *Journal of Experimental Marine Biology and Ecology* **416,** 153–161 (2012).

17. Essock-Burns, T., Gohad, N. V., Orihuela, B., Mount, A. S., Spillmann, C. M., Wahl, K. J. & Rittschof, D. Barnacle biology before, during and after settlement and metamorphosis: a study of the interface. *Journal of Experimental Biology* jeb.145094 (2016). doi:10.1242/jeb.145094

18. Kamino, K. in *Biological Adhesives* (ed. Smith, A. M.) 153–176 (Springer International Publishing, 2016). doi:10.1007/978-3-319-46082-6_7

19. CRISP, D. J. The Behaviour of Barnacle Cyprids in Relation to Water Movement over a Surface. *Journal of Experimental Biology* **32,** 569–590 (1955).

20. Barnes, H. & Blackstock, J. The biochemical composition of the cement of a pedunculate cirripede. *Journal of Experimental Marine Biology and Ecology* **16,** 87–91 (1974).

21. Bourget, E. & Crisp, D. J. An analysis of the growth bands and ridges of barnacle shell plates. *Journal of the Marine Biological Association of the United Kingdom* **55,** 439–461 (1975).

22. Bourget, E. in *Barnacle biology* 267–285 (Routledge, 2018).

23. Gohad, N. V., Dickinson, G. H., Orihuela, B., Rittschof, D. & Mount, A. S. Visualization of putative ion-transporting epithelia in Amphibalanus amphitrite using correlative microscopy: Potential function in osmoregulation and biomineralization. *Journal of Experimental Marine Biology and Ecology* **380,** 88–98 (2009).

24. Checa, A. G., Salas, C., Rodríguez-Navarro, A. B., Grenier, C. & Lagos, N. A. Articulation and growth of skeletal elements in balanid barnacles (Balanidae, Balanomorpha, Cirripedia). *R. Soc. open sci.* **6,** 190458 (2019).

25. Metzler, R. A., O'Malley, J., Herrick, J., Christensen, B., Orihuela, B., Rittschof, D. & Dickinson, G. H. *Amphibalanus amphitrite* begins exoskeleton mineralization within 48 hours of metamorphosis. *R. Soc. open sci.* **7,** 200725 (2020).

26. Barnes, H., Klepal, W. & Mitchell, B. D. The organic and inorganic composition of some cirripede shells. *Journal of Experimental Marine Biology and Ecology* **21,** 119–127 (1976).

27. Khalifa, G. M., Weiner, S. & Addadi, L. Mineral and Matrix Components of the Operculum and Shell of the Barnacle Balanus amphitrite: Calcite Crystal Growth in a Hydrogel. *Crystal Growth & Design* **11,** 5122–5130 (2011).

28. Raman, S. & Kumar, R. Construction and nanomechanical properties of the exoskeleton of the barnacle, Amphibalanus reticulatus. *Journal of Structural Biology* **176,** 360–369 (2011).

29. Lewis, A. C., Burden, D. K., Wahl, K. J. & Everett, R. K. Electron Backscatter Diffraction (EBSD) Study of the Structure and Crystallography of the Barnacle Balanus amphitrite. *JOM* **66,** 143–148 (2014).

30. So, C. R., Scancella, J. M., Fears, K. P., Essock-Burns, T., Haynes, S. E., Leary, D. H., Diana, Z., Wang, C., North, S., Oh, C. S., Wang, Z., Orihuela, B., Rittschof, D., Spillmann, C. M. & Wahl, K. J. Oxidase Activity of the Barnacle Adhesive Interface Involves Peroxide-Dependent Catechol Oxidase and Lysyl Oxidase Enzymes. *ACS Appl. Mater. Interfaces* **9,** 11493–11505 (2017).

31. Power, A. M., Klepal, W., Zheden, V., Jonker, J., McEvilly, P. & von Byern, J. in *Biological adhesive systems* 153–168 (Springer, 2010).

32. Burden, D. K., Spillmann, C. M., Everett, R. K., Barlow, D. E., Orihuela, B., Deschamps, J. R., Fears, K. P., Rittschof, D. & Wahl, K. J. Growth and development of the barnacle *Amphibalanus amphitrite* : time and spatially resolved structure and chemistry of the base plate. *Biofouling* **30,** 799–812 (2014).

33. Kamino, K. Mini-review: barnacle adhesives and adhesion. *Biofouling* **29,** 735–749 (2013).

34. Mori, Y., Urushida, Y., Nakano, M., Uchiyama, S. & Kamino, K. Calcitespecific coupling protein in barnacle underwater cement. *FEBS Journal* 11 (2007).

35. Barlow, D. E., Dickinson, G. H., Orihuela, B., Kulp III, J. L., Rittschof, D. & Wahl, K. J. Characterization of the adhesive plaque of the barnacle Balanus amphitrite: amyloid-like nanofibrils are a major component. *Langmuir* **26,** 6549–6556 (2010).

36. Barlow, D. E., Dickinson, G. H., Orihuela, B., Rittschof, D. & Wahl, K. J. In situ ATR–FTIR characterization of primary cement interfaces of the barnacle Balanus amphitrite. *Biofouling* **25,** 359–366 (2009).

37. Sullan, R. M. A., Gunari, N., Tanur, A. E., Chan, Y., Dickinson, G. H., Orihuela, B., Rittschof, D. & Walker, G. C. Nanoscale structures and mechanics of barnacle cement. *null* **25,** 263–275 (2009).

38. Golden, J. P., Burden, D. K., Fears, K. P., Barlow, D. E., So, C. R., Burns, J., Miltenberg, B., Orihuela, B., Rittshof, D., Spillmann, C. M., Wahl, K. J. & Tender, L. M. Imaging Active Surface Processes in Barnacle Adhesive Interfaces. *Langmuir* **32,** 541–550 (2016).

39. Wasmer, C., Lange, A., Van Melckebeke, H., Siemer, A. B., Riek, R. & Meier, B. H. Amyloid fibrils of the HET-s (218–289) prion form a β solenoid with a triangular hydrophobic core. *Science* **319,** 1523–1526 (2008).

40. Sawaya, M. R., Sambashivan, S., Nelson, R., Ivanova, M. I., Sievers, S. A., Apostol, M. I., Thompson, M. J., Balbirnie, M., Wiltzius, J. J. & McFarlane, H. T. Atomic structures of amyloid cross-β spines reveal varied steric zippers. *Nature* **447,** 453–457 (2007).

41. Zhong, C., Gurry, T., Cheng, A. A., Downey, J., Deng, Z., Stultz, C. M. & Lu, T. K. Strong underwater adhesives made by self-assembling multi-protein nanofibres. *Nature nanotechnology* **9,** 858–866 (2014).

42. Knowles, T. P. J. & Buehler, M. J. Nanomechanics of functional and pathological amyloid materials. *Nature Nanotechnology* **6,** 469–479 (2011).

43. Fukuma, T., Mostaert, A. S. & Jarvis, S. P. Explanation for the mechanical strength of amyloid fibrils. *Tribology Letters* **22,** 233–237 (2006).

44. Sunde, M., Serpell, L. C., Bartlam, M., Fraser, P. E., Pepys, M. B. & Blake, C. C. Common core structure of amyloid fibrils by synchrotron X-ray diffraction. *Journal of molecular biology* **273,** 729–739 (1997).

45. Toyama, B. H. & Weissman, J. S. Amyloid structure: conformational diversity and consequences. *Annual review of biochemistry* **80,** 557–585 (2011).

46. Ke, P. C., Zhou, R., Serpell, L. C., Riek, R., Knowles, T. P. J., Lashuel, H. A., Gazit, E., Hamley, I. W., Davis, T. P., Fändrich, M., Otzen, D. E., Chapman, M. R., Dobson, C. M., Eisenberg, D. S. & Mezzenga, R. Half a century of amyloids: past, present and future. *Chem. Soc. Rev.* **49,** 5473–5509 (2020).

47. Chiti, F. & Dobson, C. M. Protein misfolding, amyloid formation, and human disease: a summary of progress over the last decade. *Annual review of biochemistry* **86,** 27–68 (2017).

48. Kato, M., Han, T. W., Xie, S., Shi, K., Du, X., Wu, L. C., Mirzaei, H., Goldsmith, E. J., Longgood, J. & Pei, J. Cell-free formation of RNA granules: low complexity sequence domains form dynamic fibers within hydrogels. *Cell* **149,** 753–767 (2012).

49. Murray, D. T., Kato, M., Lin, Y., Thurber, K. R., Hung, I., McKnight, S. L. & Tycko, R. Structure of FUS protein fibrils and its relevance to self-assembly and phase separation of low-complexity domains. *Cell* **171,** 615–627 (2017).

50. Hughes, M. P., Sawaya, M. R., Boyer, D. R., Goldschmidt, L., Rodriguez, J. A., Cascio, D., Chong, L., Gonen, T. & Eisenberg, D. S. Atomic structures of low-complexity protein segments reveal kinked β sheets that assemble networks. *Science* **359,** 698–701 (2018).

51. Knowles, T. P., Fitzpatrick, A. W., Meehan, S., Mott, H. R., Vendruscolo, M., Dobson, C. M. & Welland, M. E. Role of intermolecular forces in defining material properties of protein nanofibrils. *science* **318,** 1900–1903 (2007).

52. Chapman, M. R., Robinson, L. S., Pinkner, J. S., Roth, R., Heuser, J., Hammar, M., Normark, S. & Hultgren, S. J. Role of Escherichia coli curli operons in directing amyloid fiber formation. *Science* **295,** 851–855 (2002).

53. Jarvis, S. & Mostaert, A. *The functional fold: amyloid structures in nature*. (CRC Press, 2012).

54. Mostaert, A. S., Crockett, R., Kearn, G., Cherny, I., Gazit, E., Serpell, L. C. & Jarvis, S. P. Mechanically functional amyloid fibrils in the adhesive of a marine invertebrate as revealed by Raman spectroscopy and atomic force microscopy. *Archives of histology and cytology* **72,** 199–207 (2009).

55. Gebbink, M. F., Claessen, D., Bouma, B., Dijkhuizen, L. & Wösten, H. A. Amyloids—a functional coat for microorganisms. *Nature Reviews Microbiology* **3,** 333–341 (2005).

56. Nakano, M. & Kamino, K. Amyloid-like conformation and interaction for the self-assembly in barnacle underwater cement. *Biochemistry* **54,** 826–835 (2015).

57. So, C. R., Liu, J., Fears, K. P., Leary, D. H., Golden, J. P. & Wahl, K. J. Self-assembly of protein nanofibrils orchestrates calcite step movement through selective nonchiral interactions. *ACS nano* **9,** 5782–5791 (2015).

58. Wiegemann, M. & Watermann, B. Peculiarities of barnacle adhesive cured on non-stick surfaces. *Journal of adhesion science and technology* **17,** 1957–1977 (2003).

59. Dickinson, G. H., Vega, I. E., Wahl, K. J., Orihuela, B., Beyley, V., Rodriguez, E. N., Everett, R. K., Bonaventura, J. & Rittschof, D. Barnacle cement: a polymerization model based on evolutionary concepts. *Journal of Experimental Biology* **212,** 3499–3510 (2009).

60. So, C. R., Yates, E. A., Estrella, L. A., Fears, K. P., Schenck, A. M., Yip, C. M. & Wahl, K. J. Molecular Recognition of Structures Is Key in the Polymerization of Patterned Barnacle Adhesive Sequences. *ACS Nano* **13,** 5172–5183 (2019).

61. Waite, J. H. Nature's underwater adhesive specialist. *International Journal of Adhesion and Adhesives* **7,** 9–14 (1987).

62. Kamino, K. Underwater Adhesive of Marine Organisms as the Vital Link Between Biological Science and Material Science. *Mar Biotechnol* 11 (2008).

63. Zhang, W. & Laursen, R. A. Structure-function relationships in a type I antifreeze polypeptide: the role of threonine methyl and hydroxyl groups in antifreeze activity. *Journal of Biological Chemistry* **273,** 34806–34812 (1998).

64. Fletcher, G. L., Hew, C. L. & Davies, P. L. Antifreeze proteins of teleost fishes. *Annual review of physiology* **63,** 359–390 (2001).

65. Jia, Z. & Davies, P. L. Antifreeze proteins: an unusual receptor–ligand interaction. *Trends in biochemical sciences* **27,** 101–106 (2002).

66. Urushida, Y., Nakano, M., Matsuda, S., Inoue, N., Kanai, S., Kitamura, N., Nishino, T. & Kamino, K. Identification and functional characterization of a novel barnacle cement protein. *The FEBS journal* **274,** 4336–4346 (2007).

67. Deming, T. J. Mussel byssus and biomolecular materials. *Current opinion in chemical biology* **3,** 100–105 (1999).

68. Statz, A. R., Meagher, R. J., Barron, A. E. & Messersmith, P. B. New peptidomimetic polymers for antifouling surfaces. *Journal of the American Chemical Society* **127,** 7972–7973 (2005).

69. Sagert, J. & Sun, C. in *Biological adhesives* 125–143 (Springer, 2006).

70. Mohanram, H., Kumar, A., Verma, C. S., Pervushin, K. & Miserez, A. Three-dimensional structure of *Megabalanus rosa* Cement Protein 20 revealed by multi-dimensional NMR and molecular dynamics simulations. *Phil. Trans. R. Soc. B* **374,** 20190198 (2019).

71. Kumar, A., Mohanram, H., Li, J., Le Ferrand, H., Verma, C. S. & Miserez, A. Disorder–Order Interplay of a Barnacle Cement Protein Triggered by Interactions with Calcium and Carbonate Ions: A Molecular Dynamics Study. *Chem. Mater.* **32,** 8845–8859 (2020).

72. Kamino, K. Novel barnacle underwater adhesive protein is a charged amino acid-rich protein constituted by a Cys-rich repetitive sequence. 5 (2001).

73. Suzuki, R., Mori, Y., Kamino, K. & Yamazaki, T. NMR assignment of the barnacle cement protein Mrcp-20k. *Journal of biomolecular NMR* **32,** 257 (2005).

74. Li, S.-C., Goto, N. K., Williams, K. A. & Deber, C. M. Alpha-helical, but not beta-sheet, propensity of proline is determined by peptide environment. *Proceedings of the National Academy of Sciences* **93,** 6676–6681 (1996).

75. Mandard, N., Sy, D., Maufrais, C., Bonmatin, J.-M., Bulet, P., Hetru, C. & Vovelle, F. Androctonin, a novel antimicrobial peptide from scorpion Androctonus australis: solution structure and molecular dynamics simulations in the presence of a lipid monolayer. *Journal of Biomolecular Structure and Dynamics* **17,** 367–380 (1999).

76. Iijima, M., Hashimoto, T., Matsuda, Y., Nagai, T., Yamano, Y., Ichi, T., Osaki, T. & Kawabata, S. Comprehensive sequence analysis of horseshoe crab cuticular proteins and their involvement in transglutaminase-dependent cross-linking. *The FEBS journal* **272,** 4774–4786 (2005).

77. Maksimainen, M., Hakulinen, N., Kallio, J. M., Timoharju, T., Turunen, O. & Rouvinen, J. Crystal structures of Trichoderma reesei β-galactosidase reveal conformational changes in the active site. *Journal of structural biology* **174,** 156–163 (2011).

78. Williams, T., Marumo, K., Waite, J. H. & Henkens, R. W. Mussel glue protein has an open conformation. *Archives of biochemistry and biophysics* **269,** 415–422 (1989).

79. Brady Jr, R. F. & Singer, I. L. Mechanical factors favoring release from fouling release coatings. *Biofouling* **15,** 73–81 (2000).

80. Newby, B. Z., Chaudhury, M. K. & Brown, H. R. Macroscopic evidence of the effect of interfacial slippage on adhesion. *Science* **269,** 1407–1409 (1995).

81. Zhang Newby, B. & Chaudhury, M. K. Effect of interfacial slippage on viscoelastic adhesion. *Langmuir* **13,** 1805–1809 (1997).

82. Singer, I. L., Kohl, J. G. & Patterson, M. Mechanical aspects of silicone coatings for hard foulant control. *Biofouling* **16,** 301–309 (2000).

83. Brady Jr, R. F. A fracture mechanical analysis of fouling release from nontoxic antifouling coatings. *Progress in organic coatings* **43,** 188–192 (2001).

84. Bausch, G. G. & Tonge, J. S. Silicone technology for fouling release coating systems. *Proc Waterborne High-Solids Powder* 340–353 (1996).

85. Brady, R. F. In search of non-stick coatings. *Chemistry and industry* 219–22 (1997).

86. Swain, G., Anil, A. C., Baier, R. E., Chia, F.-S., Conte, E., Cook, A., Hadfield, M., Haslbeck, E., Holm, E. & Kavanagh, C. Biofouling and barnacle adhesion data for fouling-release coatings subjected to static immersion at seven marine sites. *Biofouling* **16,** 331–344 (2000).

87. Kavanagh, C. J., Schultz, M. P., Swain, G. W., Stein, J., Truby, K. & Wood, C. D. Variation in adhesion strength of Balanus eburneus, crassostrea virginica and hydroides dianthus to fouling-release coatings. *Biofouling* **17,** 155–167 (2001).

88. Kavanagh, C. J., Quinn, R. D. & Swain, G. W. Observations of barnacle detachment from silicones using high-speed video. *The Journal of Adhesion* **81,** 843–868 (2005).

89. Berglin, M. & Gatenholm, P. The barnacle adhesive plaque: morphological and chemical differences as a response to substrate properties. *Colloids and Surfaces B: Biointerfaces* **28,** 107–117 (2003).

90. Wendt, D. E., Kowalke, G. L., Kim, J. & Singer, I. L. Factors that influence elastomeric coating performance: the effect of coating thickness on basal plate morphology, growth and critical removal stress of the barnacle Balanus amphitrite. *Biofouling* **22,** 1–9 (2006).

91. Swain, G. W. & Schultz, M. P. The testing and evaluation of non-toxic antifouling coatings. *Biofouling* **10,** 187–197 (1996).

92. Chung, J. Y. & Chaudhury, M. K. Soft and hard adhesion. *The Journal of Adhesion* **81,** 1119–1145 (2005).

93. Ramsay, D. B., Dickinson, G. H., Orihuela, B., Rittschof, D. & Wahl, K. J. Base plate mechanics of the barnacle Balanus amphitrite (= Amphibalanu s amphitrite). *Biofouling* **24,** 109–118 (2008).

94. Hui, C.-Y., Long, R., Wahl, K. J. & Everett, R. K. Barnacles resist removal by crack trapping. *Journal of the Royal Society Interface* **8,** 868–879 (2011).

95. Kaffashi, A., Jannesari, A. & Ranjbar, Z. Silicone fouling-release coatings: effects of the molecular weight of poly (dimethylsiloxane) and tetraethyl orthosilicate on the magnitude of pseudobarnacle adhesion strength. *Biofouling* **28,** 729–741 (2012).

96. Boyjoo, Y., Pareek, V. K. & Liu, J. Synthesis of micro and nano-sized calcium carbonate particles and their applications. *Journal of Materials Chemistry A* **2,** 14270–14288 (2014).

97. Maleki Dizaj, S., Barzegar-Jalali, M., Zarrintan, M. H., Adibkia, K. & Lotfipour, F. Calcium carbonate nanoparticles as cancer drug delivery system. *Expert opinion on drug delivery* **12,** 1649–1660 (2015).

98. Som, A., Raliya, R., Tian, L., Akers, W., Ippolito, J. E., Singamaneni, S., Biswas, P. & Achilefu, S. Monodispersed calcium carbonate nanoparticles modulate local pH and inhibit tumor growth in vivo. *Nanoscale* **8,** 12639–12647 (2016).

99. Yu, H.-D., Zhang, Z.-Y., Win, K. Y., Chan, J., Teoh, S. H. & Han, M.-Y. Bioinspired fabrication of 3D hierarchical porous nanomicrostructures of calcium carbonate for bone regeneration. *Chemical communications* **46,** 6578–6580 (2010).

100. Erez, J. The source of ions for biomineralization in foraminifera and their implications for paleoceanographic proxies. *Reviews in mineralogy and geochemistry* **54,** 115–149 (2003).

101. Anbu, P., Kang, C.-H., Shin, Y.-J. & So, J.-S. Formations of calcium carbonate minerals by bacteria and its multiple applications. *Springerplus* **5,** 1–26 (2016).

102. Reddy, M. S. Biomineralization of calcium carbonates and their engineered applications: a review. *Frontiers in microbiology* **4,** 314 (2013).

103. Ries, J. B. Geological and experimental evidence for secular variation in seawater Mg/Ca (calcite-aragonite seas) and its effects on marine biological calcification. *Biogeosciences* **7,** 2795–2849 (2010).

104. Meldrum, F. C. Calcium carbonate in biomineralisation and biomimetic chemistry. *International Materials Reviews* **48,** 187–224 (2003).

105. Aizenberg, J., Black, A. J. & Whitesides, G. M. Control of crystal nucleation by patterned self-assembled monolayers. *Nature* **398,** 495–498 (1999).

106. Aizenberg, J. Crystallization in Patterns: A Bio-Inspired Approach. *Advanced Materials* **16,** 1295–1302 (2004).

107. Travaille, A. M., Donners, J. J., Gerritsen, J. W., Sommerdijk, N. A., Nolte, R. J. & van Kempen, H. Aligned growth of calcite crystals on a self-assembled monolayer. *Advanced Materials* **14,** 492–495 (2002).

108. Han, Y.-J. & Aizenberg, J. Face-Selective Nucleation of Calcite on Self-Assembled Monolayers of Alkanethiols: Effect of the Parity of the Alkyl Chain. *Angew. Chem. Int. Ed.* **42,** 3668–3670 (2003).

109. Han, Y.-J. & Aizenberg, J. Effect of magnesium ions on oriented growth of calcite on carboxylic acid functionalized self-assembled monolayer. *Journal of the American Chemical Society* **125,** 4032–4033 (2003).

110. Aizenberg, J., Muller, D. A., Grazul, J. L. & Hamann, D. R. Direct fabrication of large micropatterned single crystals. *Science* **299,** 1205–1208 (2003).

111. Wu, C., Sun, Z. & Liu, L.-S. Quantitative control of CaCO $_3$ growth on quartz crystal microbalance sensors as a signal amplification method. *Analyst* **142,** 2547–2551 (2017).

112. Tao, F. & Bernasek, S. L. Understanding odd− even effects in organic self-assembled monolayers. *Chemical reviews* **107,** 1408–1453 (2007).

113. Wang, Z., Chen, J., Oyola-Reynoso, S. & Thuo, M. The Porter-Whitesides Discrepancy: Revisiting Odd-Even Effects in Wetting Properties of n-Alkanethiolate SAMs. *Coatings* **5,** 1034–1055 (2015).

114. Love, J. C., Estroff, L. A., Kriebel, J. K., Nuzzo, R. G. & Whitesides, G. M. Self-Assembled Monolayers of Thiolates on Metals as a Form of Nanotechnology. *Chem. Rev.* **105,** 1103–1170 (2005).

115. Hood, M. A., Landfester, K. & Muñoz-Espí, R. The Role of Residue Acidity on the Stabilization of Vaterite by Amino Acids and Oligopeptides. *Crystal Growth & Design* **14,** 1077–1085 (2014).

116. Mann, S. *Biomineralization: principles and concepts in bioinorganic materials chemistry*. **5,** (Oxford University Press on Demand, 2001).

117. Belcher, A. M., Wu, X. H., Christensen, R. J., Hansma, P. K., Stucky, G. D. & Morse, D. E. Control of crystal phase switching and orientation by soluble mollusc-shell proteins. *Nature* **381,** 56–58 (1996).

118. Aizenberg, J., Lambert, G., Weiner, S. & Addadi, L. Factors involved in the formation of amorphous and crystalline calcium carbonate: a study of an ascidian skeleton. *Journal of the American Chemical Society* **124,** 32–39 (2002).

119. Scheffel, A., Gruska, M., Faivre, D., Linaroudis, A., Plitzko, J. M. & Schüler, D. An acidic protein aligns magnetosomes along a filamentous structure in magnetotactic bacteria. *Nature* **440,** 110–114 (2006).

120. Michenfelder, M., Fu, G., Lawrence, C., Weaver, J. C., Wustman, B. A., Taranto, L., Evans, J. S. & Morse, D. E. Characterization of two molluscan crystal-modulating biomineralization proteins and identification of putative mineral binding domains. *Biopolymers: Original Research on Biomolecules* **70,** 522–533 (2003).

121. Orme, C. A., Noy, A., Wierzbicki, A., McBride, M. T., Grantham, M., Teng, H. H., Dove, P. M. & DeYoreo, J. J. Formation of chiral morphologies through selective binding of amino acids to calcite surface steps. *Nature* **411,** 775–779 (2001).

122. Gotliv, B.-A., Addadi, L. & Weiner, S. Mollusk shell acidic proteins: in search of individual functions. *ChemBioChem* **4,** 522–529 (2003).

123. Addadi, L., Joester, D., Nudelman, F. & Weiner, S. Mollusk shell formation: a source of new concepts for understanding biomineralization processes. *Chemistry–A European Journal* **12,** 980–987 (2006).

124. Morse, J. W., Arvidson, R. S. & Lüttge, A. Calcium carbonate formation and dissolution. *Chemical reviews* **107,** 342–381 (2007).

125. Suzuki, M., Saruwatari, K., Kogure, T., Yamamoto, Y., Nishimura, T., Kato, T. & Nagasawa, H. An acidic matrix protein, Pif, is a key macromolecule for nacre formation. *Science* **325,** 1388–1390 (2009).

126. Mohanram, H., Georges, T., Pervushin, K., Azaïs, T. & Miserez, A. Self-Assembly of a Barnacle Cement Protein (MrCP20) into Adhesive Nanofibrils with Concomitant Regulation of $CaCO_3$ Polymorphism. *Chem. Mater.* **33,** 9715–9724 (2021).

127. Tetsch, L., Koller, C., Dönhöfer, A. & Jung, K. Detection and function of an intramolecular disulfide bond in the pH-responsive CadC of Escherichia coli. *BMC microbiology* **11,** 1–12 (2011).

128. Hoffman, M. Z. & Hayon, E. One-electron reduction of the disulfide linkage in aqueous solution. Formation, protonation, and decay kinetics of the RSSR-radical. *Journal of the American Chemical Society* **94,** 7950–7957 (1972).

129. Kim, Y. S., Liu, L., Axelsen, P. H. & Hochstrasser, R. M. 2D IR provides evidence for mobile water molecules in β-amyloid fibrils. *Proceedings of the National Academy of Sciences* **106,** 17751–17756 (2009).

130. Zhang, M., Zhao, J. & Zheng, J. Molecular understanding of a potential functional link between antimicrobial and amyloid peptides. *Soft Matter* **10,** 7425–7451 (2014).

131. Hadfield, C., Cashmore, A. M. & Meacock, P. A. An efficient chloramphenicol-resistance marker for Saccharomyces cerevisiae and Escherichia coli. *Gene* **45,** 149–158 (1986).

132. Tran, C. & Hadfield, M. G. Larvae of Pocillopora damicornis (Anthozoa) settle and metamorphose in response to surface-biofilm bacteria. *Marine Ecology Progress Series* **433,** 85–96 (2011).

133. Pawlik, J. R. & Hadfield, M. G. A symposium on chemical factors that influence the settlement and metamorphosis of marine invertebrate larvae: introduction and perspective. *Bull. Mar. Sci* **46,** 450–454 (1990).

134. Unabia, C. R. C. & Hadfield, M. G. Role of bacteria in larval settlement and metamorphosis of the polychaete Hydroides elegans. *Marine Biology* **133,** 55–64 (1999).

135. Rittschof, D., Maki, J., Mitchell, R. & Costlow, J. D. Ion and neuropharmacological studies of barnacle settlement. *Netherlands Journal of Sea Research* **20,** 269–275 (1986).

136. Maki, J. S., Rittschof, D., Schmidt, A. R., Snyder, A. G. & Mitchell, R. Factors controlling attachment of bryozoan larvae: a comparison of bacterial films and unfilmed surfaces. *The Biological Bulletin* **177,** 295–302 (1989).

137. Maki, J. S., Ding, L., Stokes, J., Kavouras, J. H. & Rittschof, D. Substratum/bacterial interactions and larval attachment: films and exopolysaccharides of Halomonas marina (ATCC 25374) and their effect on barnacle cyprid larvae, Balanus amphitrite Darwin. *Biofouling* **16,** 159–170 (2000).

138. Dobretsov, S., Abed, R. M. & Teplitski, M. Mini-review: Inhibition of biofouling by marine microorganisms. *Biofouling* **29,** 423–441 (2013).

139. Khandeparker, L., Chandrashekar Anil, A. & Raghukumar, S. Relevance of biofilm bacteria in modulating the larval metamorphosis of Balanus amphitrite. *FEMS microbiology ecology* **58,** 425–438 (2006).

140. Knight-Jones, E. W. & Stevenson, J. P. Gregariousness during settlement in the barnacle Elminius modestus Darwin. *Journal of the Marine Biological Association of the United Kingdom* **29,** 281–297 (1950).

141. Dreanno, C., Kirby, R. R. & Clare, A. S. Smelly feet are not always a bad thing: the relationship between cyprid footprint protein and the barnacle settlement pheromone. *Biology letters* **2,** 423–425 (2006).

142. Dreanno, C., Matsumura, K., Dohmae, N., Takio, K., Hirota, H., Kirby, R. R. & Clare, A. S. An α2-macroglobulin-like protein is the cue to gregarious settlement of the barnacle Balanus amphitrite. *Proceedings of the National Academy of Sciences* **103,** 14396–14401 (2006).

143. Khandeparker, L. & Anil, A. C. Role of conspecific cues and sugars in the settlement of cyprids of the barnacle, Balanus amphitrite. *Journal of Zoology* **284,** 206–214 (2011).

144. Faimali, M., Garaventa, F., Terlizzi, A., Chiantore, M. & Cattaneo-Vietti, R. The interplay of substrate nature and biofilm formation in regulating Balanus amphitrite Darwin, 1854 larval settlement. *Journal of Experimental Marine Biology and Ecology* **306,** 37–50 (2004).

145. Zardus, J. D., Nedved, B. T., Huang, Y., Tran, C. & Hadfield, M. G. Microbial biofilms facilitate adhesion in biofouling invertebrates. *The Biological Bulletin* **214,** 91–98 (2008).

146. Rajitha, K., Nancharaiah, Y. V. & Venugopalan, V. P. Insight into bacterial biofilm-barnacle larvae interactions for environmentally benign antifouling strategies. *International Biodeterioration & Biodegradation* **149,** 104937 (2020).

147. Zhao, H., Sood, R., Jutila, A., Bose, S., Fimland, G., Nissen-Meyer, J. & Kinnunen, P. K. Interaction of the antimicrobial peptide pheromone Plantaricin A with model membranes: implications for a novel mechanism of action. *Biochimica et biophysica acta (BBA)-biomembranes* **1758,** 1461–1474 (2006).

148. Mahalka, A. K. & Kinnunen, P. K. Binding of amphipathic α-helical antimicrobial peptides to lipid membranes: Lessons from temporins B and L. *Biochimica et Biophysica Acta (BBA)-Biomembranes* **1788,** 1600–1609 (2009).

149. Trexler, A. J. & Nilsson, M. R. The formation of amyloid fibrils from proteins in the lysozyme family. *Current Protein and Peptide Science* **8,** 537–557 (2007).

150. Nilsson, M. R. & Dobson, C. M. In vitro characterization of lactoferrin aggregation and amyloid formation. *Biochemistry* **42,** 375–382 (2003).

151. Torrent, M., Odorizzi, F., Nogués, M. V. & Boix, E. Eosinophil cationic protein aggregation: identification of an N-terminus amyloid prone region. *Biomacromolecules* **11,** 1983–1990 (2010).

152. Arispe, N., Diaz, J. C. & Simakova, O. Aβ ion channels. Prospects for treating Alzheimer's disease with Aβ channel blockers. *Biochimica et Biophysica Acta (BBA)-Biomembranes* **1768,** 1952–1965 (2007).

153. Lal, R., Lin, H. & Quist, A. P. Amyloid beta ion channel: 3D structure and relevance to amyloid channel paradigm. *Biochimica et Biophysica Acta (BBA)-Biomembranes* **1768,** 1966–1975 (2007).

154. Jang, H., Zheng, J., Lal, R. & Nussinov, R. New structures help the modeling of toxic amyloidß ion channels. *Trends in biochemical sciences* **33,** 91–100 (2008).

155. Capone, R., Quiroz, F. G., Prangkio, P., Saluja, I., Sauer, A. M., Bautista, M. R., Turner, R. S., Yang, J. & Mayer, M. Amyloid-β-induced ion flux in artificial lipid bilayers and neuronal cells: resolving a controversy. *Neurotoxicity research* **16,** 1–13 (2009).

156. Sokolov, Y., Kozak, J. A., Kayed, R., Chanturiya, A., Glabe, C. & Hall, J. E. Soluble amyloid oligomers increase bilayer conductance by altering dielectric structure. *The Journal of general physiology* **128,** 637–647 (2006).

157. Dante, S., Hauß, T., Brandt, A. & Dencher, N. A. Membrane fusogenic activity of the Alzheimer's peptide Aβ (1–42) demonstrated by small-angle neutron scattering. *Journal of molecular biology* **376,** 393–404 (2008).

158. Kayed, R., Sokolov, Y., Edmonds, B., McIntire, T. M., Milton, S. C., Hall, J. E. & Glabe, C. G. Permeabilization of lipid bilayers is a common conformation-dependent activity of soluble amyloid oligomers in protein misfolding diseases. *Journal of Biological Chemistry* **279,** 46363–46366 (2004).

159. Lemkul, J. A. & Bevan, D. R. Perturbation of membranes by the amyloid β-peptide–a molecular dynamics study. *The FEBS journal* **276,** 3060–3075 (2009).

160. Chi, E. Y., Ege, C., Winans, A., Majewski, J., Wu, G., Kjaer, K. & Lee, K. Y. C. Lipid membrane templates the ordering and induces the fibrillogenesis of Alzheimer's disease amyloid-β peptide. *Proteins: Structure, Function, and Bioinformatics* **72,** 1–24 (2008).

161. Ege, C. & Lee, K. Y. C. Insertion of Alzheimer's Aβ40 peptide into lipid monolayers. *Biophysical journal* **87,** 1732–1740 (2004).

162. Valincius, G., Heinrich, F., Budvytyte, R., Vanderah, D. J., McGillivray, D. J., Sokolov, Y., Hall, J. E. & Lösche, M. Soluble amyloid β-oligomers affect dielectric

membrane properties by bilayer insertion and domain formation: implications for cell toxicity. *Biophysical journal* **95,** 4845–4861 (2008).

163. Hertel, C., Terzi, E., Hauser, N., Jakob-Røtne, R., Seelig, J. & Kemp, J. A. Inhibition of the electrostatic interaction between β-amyloid peptide and membranes prevents β-amyloid-induced toxicity. *Proceedings of the National Academy of Sciences* **94,** 9412–9416 (1997).

164. Zhao, H., Tuominen, E. K. & Kinnunen, P. K. Formation of amyloid fibers triggered by phosphatidylserine-containing membranes. *Biochemistry* **43,** 10302–10307 (2004).

165. Torrent, M., Valle, J., Nogués, M. V., Boix, E. & Andreu, D. The generation of antimicrobial peptide activity: a trade-off between charge and aggregation? *Angewandte Chemie* **123,** 10874–10877 (2011).

166. Lashuel, H. A. & Lansbury, P. T. Are amyloid diseases caused by protein aggregates that mimic bacterial pore-forming toxins? *Quarterly reviews of biophysics* **39,** 167–201 (2006).

167. Lee, C.-C., Sun, Y. & Huang, H. W. How type II diabetes-related islet amyloid polypeptide damages lipid bilayers. *Biophysical Journal* **102,** 1059–1068 (2012).

168. Engel, M. F., Khemtémourian, L., Kleijer, C. C., Meeldijk, H. J., Jacobs, J., Verkleij, A. J., de Kruijff, B., Killian, J. A. & Höppener, J. W. Membrane damage by human islet amyloid polypeptide through fibril growth at the membrane. *Proceedings of the National Academy of Sciences* **105,** 6033–6038 (2008).

169. Soscia, S. J., Kirby, J. E., Washicosky, K. J., Tucker, S. M., Ingelsson, M., Hyman, B., Burton, M. A., Goldstein, L. E., Duong, S. & Tanzi, R. E. The Alzheimer's disease-associated amyloid β-protein is an antimicrobial peptide. *PloS one* **5,** e9505 (2010).

170. Last, N. B. & Miranker, A. D. Common mechanism unites membrane poration by amyloid and antimicrobial peptides. *Proceedings of the National Academy of Sciences* **110,** 6382–6387 (2013).

Chapter 3 Biophysical Characterizations of Barnacle Cement Proteins

Structural morphology of recombinant barnacle cement proteins MrCP19 and MrCP20 were experimentally characterized, and their molecular features discussed in this Chapter. The expression and purification of the proteins in monomeric form were confirmed with SDS-PAGE and MALDI-TOF. Secondary structure of the proteins was studied by CD measurements with the variance of the protein concentration. Together with CD results, result of ThT assay on self-assembled cement proteins indicated amyloid fibrillation of MrCP19. Characterization by DLS showed a much larger hydrodynamic radius of MrCP19 compared to MrCP20, especially at acidic pH, which is attributed to their stronger propensity towards amyloidosis.

3.1 Introduction

Barnacles (*Megabalanus Rosa*) have evolved unique surface adhesion strategy using multi-protein complex "cement". The morphology and biophysical properties of this cement layer underneath the barnacles has been widely studied, but information of the individual cement components is still incomplete. The two soluble recombinant cement proteins we are focusing on in this project, MrCP19 and MrCP20, were characterized after expression and purification to shed light on their biophysical behavior for further experiments.

The transformation of the gene encoding MrCP19 and MrCP20 was successfully done in *E. coli* with a heat shock method, followed by expression and a two-step purification protocol. The Ni-NTA purification was used to selectively purify His_6-tagged recombinant cement proteins. SEC was further used to separate monomeric MrCP19 and MrCP20 from their aggregated (oligomeric) proteins or from other bacterial components. The purity and molecular weight of the protein solution were confirmed by SDS-PAGE and MALDI-TOF.

To further study the molecular features of the proteins, their secondary structure was analyzed using CD spectroscopy. Additional conformation for amyloid fibrillation of the proteins was verified with ThT assay. These results were taken together to evaluate the hydrodynamic size of the proteins measured by DLS. Analysis of proteins structural behavior in this Section will be used to understand subsequent experimental results.

3.2 Materials and Methods

3.2.1 Transformation of Recombinant Plasmid of *MrCP19* and *MrCP20*

The codon-optimized gene encoding His6-tagged at the C-terminus of MrCP19 and MrCP20 were purchased from DNA 2.0 (Newark, California). The expression-ready pJ431 vector has low copy number, yielding between 0.2 - 1 µg DNA per mL of Luria-Bertani (LB) culture, with kanamycin resistance. The MrCP19 and MrCP20 genes were transformed into *E. coli* BL21 (DE3) competent cells with a heat shock method as follows. After 30 min of incubation on ice, a mixture of a chemically competent bacteria and DNA plasmids was placed at 45 ˚C for 30 sec and then placed back in ice for 5 min. 1 mL of ice-cold LB media was added and the transformed cells were incubated at 37 ˚C for 1h with agitation. Subsequently, the cells were centrifuged at 3000 rpm at 25˚C for 5 min using a high-speed refrigerated centrifuge (model CT15E, Hitachi Koki Co., Ltd., Japan). The supernatant was discarded, and the pellet was re-suspended. 100 µL of the cells was spread on the LB agar plates with Kanamycin (50 µg/mL) and incubated overnight at 37˚C.

3.2.2 Protein Expression and Purification

Expression and purification methods for both MrCP19 and MrCP20 proteins were identical. Single colonies from transformed cells were inoculated into selective LB media with Kanamycin (50 µg/mL). About 10 mL of this pre-culture was transferred into 1 L autoclaved LB medium containing 50 µg/mL Kanamycin and incubated at 37 ˚C, with shaking at 250 rpm for 3-4 hours until an optical density (OD_{600}) of 0.6-0.8 was achieved. OD_{600} was measured with Nano Drop 2000c. Subsequently, 1 mL of 1 M Isopropyl β-D-1-thiogalactopyranoside (IPTG) was added to induce cell expression, which was done at 25 ˚C, at 250 rpm overnight (16h). Comparatively low temperature was chosen to enhance the protein solubility and favor protein folding.[1–3] The 1 M IPTG stock solution was prepared by dissolving 2.38 g of IPTG in 10 mL H2O and filtering through 0.2 µm sterile filters.

The cells were harvested by centrifugation at 8000 rpm for 15 min at 4 ˚C (model CR22N, Hitachi Koki Co., Ltd., Japan). The cell pellet was gently washed with the buffer solution (50 mM Tris, 300 mM NaCl, 10 mM Imidazole, 5 mM β-Mercaptoethanol, pH 8.3), and then lysed by sonication with 35% amp and 1sec on/off pulse for 20 min. The lysate was then centrifuged at 18000 rpm for 60 min at 4 ˚C. The supernatant was collected and used for Fast Protein Liquid Chromatography purification (FPLC) in two steps: first with IMAC (Ni-NTA, HisTrap HP 1 mL or FF crude 5 mL) and then by SEC (HiLoad 16/600 Superdex 75pg) using the AKTA Purifier UPC10 (Sweden).

The supernatant was loaded onto a Ni-NTA column after an initial wash of the column with the binding buffer (50 mM Tris, 300 mM NaCl, 10 mM Imidazole, 5 mM β-Mercaptoethanol, pH 8.3), and then eluted with the elution buffer (50 mM Tris, 300 mM NaCl, 500 mM Imidazole, 5 mM β-Mercaptoethanol, pH 8.3). Subsequently, the eluted protein was loaded onto the SEC column. The column was washed with water and equilibrated with the running buffer (20 mM Tris, 150 mM NaCl, pH 8.3) followed by His-tag purified protein injections. The monomeric purified protein fractions were collected and the purity and the MW of recombinant MrCP19 and MrCP20 were assessed with SDS-PAGE.

The proteins collected in the running buffer, hereafter referred as “Tris”, were concentrated to high concentration using microporous centrifuge tubes (Vivaspin20 ultrafiltration device with Molecular weight cut-off at 3 or 5 kDa) and kept at 4˚C for stability. Acidic buffer was prepared to characterize protein behavior under acidic condition in comparison to basic condition for further experiments. The basic buffer and the acidic buffer were prepared to reproduce natural seawater condition and natural intracellular environment, respectively. Proteins in Tris were dialyzed into “AA” which is an acidic buffer with 10 mM Acetate (0.5 mM Sodium Acetate and 9.5 mM Acetic Acid) and 150 mM NaCl, at pH 3.6. The pH level of each solution was adjusted using 1.0 M HCl or 1.0 M NaOH and checked with either a pH meter (Seven Compact, Mettler Toledo) or pH indicator strips (MColorpHast).

3.2.3 MALDI-TOF

The MW of purified MrCP20 was measured using MALDI-TOF mass spectroscopy (SHIMADZU AXIMA Performance, Japan) equipped with a nitrogen laser light, and the data acquisition and process were performed using the equipment software.

The stock solution of matrix was prepared with Sinapinic Acid (3,5-dimethoxy-4-hydroxy cinnamic acid), containing 50% of acetonitrile and 0.1% of TFA. About 1 µl of protein sample (3.2 mg/mL concentration in 20mM Tris, 150 mM NaCl, pH 8.3) was mixed with 3 μL of matrix in a microcentrifuge tube to obtain a final protein concentration of 0.8 mg/mL. Then 1 μl of the sample/matrix solution was loaded onto the plate, placed in the center of the cell, and air dried. The mass spectrometer was operated in the linear mode at a 20 kV accelerating voltage, with an ion flight path of 0.68 m. The spectrum over mass/charge (*m*/*z*) ratio was acquired in linear mode averaging 10 laser shots for 25 profiles on the sample spot, at a power setting of 120 system units. The data acquisition mass range was set up from 1 to 50 kDa.

3.2.4 Circular Dichroism Spectroscopy (CD)

The CD measurements were made with AVIV Model 420 CD spectrometer (Biomedical, INC. Lakewood, NJ USA) in the wavelength range of 195-250 nm. High transparency quartz CD cuvettes with different path lengths of 0.01-1 cm were used. Each scan was recorded at the rate of 20 nm/min. Three scans were obtained for each sample with their respective baseline. The averaged baseline spectrum was subtracted from the averaged protein sample spectrum acquired. The raw ellipticity (θ) was converted to mean residue molar ellipticity ([θ]) using the following equation:

$$[\theta] = \frac{\theta \times \mathrm{MW}_i}{10000 \times C_i \times L \times N_i}$$

where MWi is the molecular weight of the protein (g/mol), C_i is the protein concentration (g/mol), L is the optical path length through solvent (cm), and N_i is the number of residues in the proteins.

3.2.5 ThT Assay for Assembled β-sheet Detection

Thioflavin T (ThT) is a fluorescent dye which is known to greatly increase its fluorescence yield upon binding to β-sheet rich structures.[4,5] The mechanism of fluorescence enhancement is attributed to the rotational immobilization of the central C–C bond connecting the benzothiazole and aniline rings since ThT binds to the side chain channels along the long axis of stacked β-sheets.[6,7] The minimal binding site of ThT is four consecutive β-strands. The fluorescence depends on the number of binding sites, affinity and quantum yield, which can specifically and uniquely respond to the amount of β-sheet assemblies in the sample. Thus, ThT assay has been used to visualize and quantify amyloid formation since 1989.[8] Prior to binding, ThT emits weakly around 427 nm. Upon binding to amyloid fibrils, ThT gives a strong fluorescence signal at approximately 482 nm when excited at 450 nm.

ThT assay on MrCPs was prepared to identify if any amyloid-like β-structure was present in the proteins. The protein samples were prepared in a 96-microwell plate (Thermo Fisher Scientific-Nuclon) with two-fold serial dilution starting from 2 mg/mL to 12th well, in volume of 80 uL. 20 µL of ThT solution was added to reach the final ThT concentration of 20 µM and the final sample solution volume of 100 µL. The fluorescence was measured with excitation at 440 nm and emission at 485 nm, at 25ºC, 9 reads per well, every 15 min followed by 5 sec orbital shaking during 24 hr, using Infinite 200 Pro (Tecan, Switzerland).

3.2.6 Dynamic Light Scattering (DLS)

The hydrodynamic radius of the cement proteins was determined by DLS, which is commonly used to detect aggregates or to determine the size of proteins and other complexes. The samples were analyzed with Malvern Zetasizer Nano ZS (Malvern, UK), using a 90° detector angle at 25 °C. Protein samples were prepared in Tris or AA at 0.05 - 1 mg/mL. Six measurement results were obtained and averaged, where each measurement was averaged over 30 readings. Each sample solution was filtered before the measurement through a sterile syringe filter with a 0.22 µm pore size.

3.2.7 Protein Charge Analysis with Zeta Potential Measurement

The zeta potentials of the proteins in solution were measured using an electrokinetic analyzer Litesizer 500 (Anton Paar, Austria). 0.5 mg/mL of each protein in Tris or AA with a reduced amount of salt was prepared in Omega Cuvette (No.225288, Anton Paar). 300 runs of measurements were carried out for each sample and the mean values were obtained.

3.3 Results and discussion

3.3.1 Protein Expression and Purification

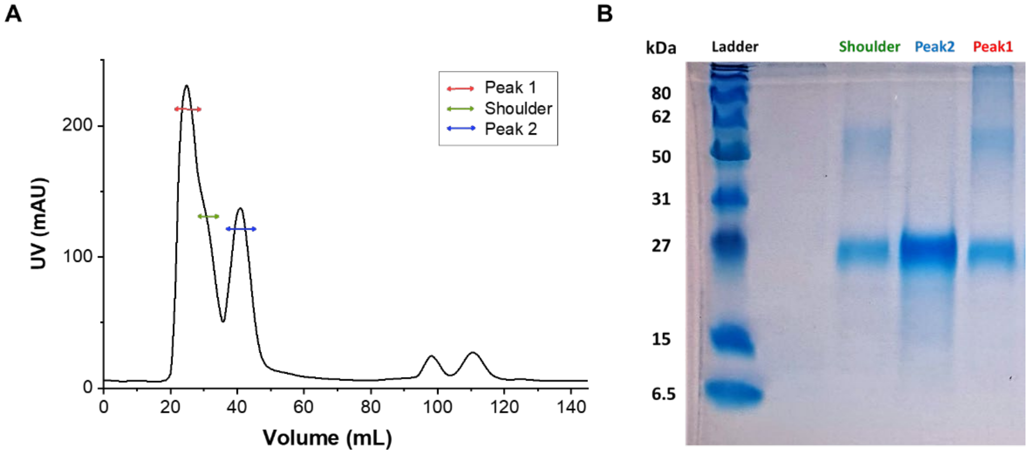

Figure 3.1 MrCP20 purification. **(A)** Representative SEC chromatogram and **(B)** the corresponding SDS-PAGE gel. Each lane corresponds to specific fractions collected during SEC purification. Elution from peak 2 (blue in the chromatogram) indicated pure monomeric form of MrCP20 protein, while elution from peak 1 (red in the chromatogram) and shoulder peak (green in the chromatogram) contained higher MW components.

MrCP20 was successfully expressed in *E. coli* BL21 (DE3) cells. As a final purification step, SEC was used to obtain highly purified monomeric protein under native conditions. Homogenously pure MrCP20 was eluted between 35-50 mL, based on the chromatogram and the SDS-PAGE analysis of the corresponding collected fractions **(Figure 3.1)**. Homogenous monomeric conformation of the protein was thus separated from the poly-disperse oligomeric conformation in this final purification step.

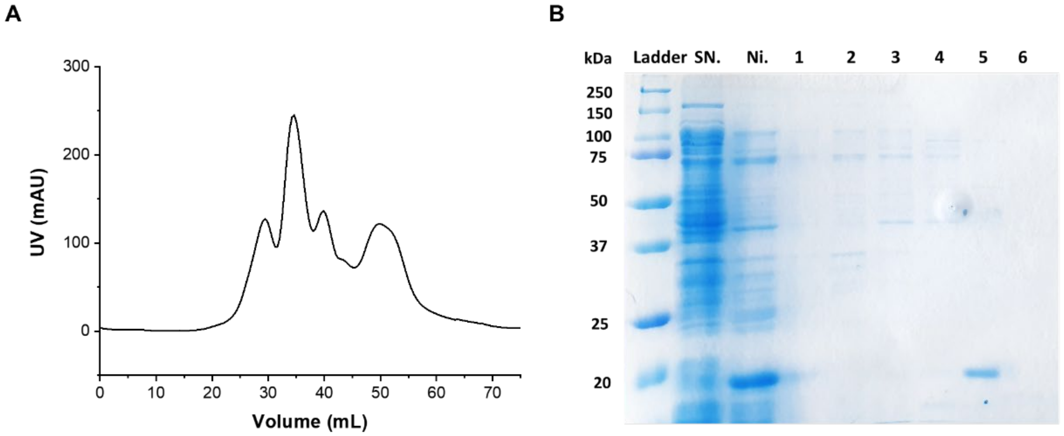

Figure 3.2 MrCP19 purification. **(A)** Representative SEC chromatogram and **(B)** the corresponding SDS-PAGE result. Each lane corresponds to different fractions collected during SEC purification. From the left to right, each row indicates MW marker, supernatant after cell lysis (SN), protein purified after Ni-NTA (Ni), and 6 different fractions from SEC elution, respectively. Only fraction 5 showed pure and good amount of MrCP19.

The recombinant MrCP19 was more difficult to obtain and the yield was less compared to MrCP20. From multiple expression and purification batches, MrCP19 was more prone to aggregation behavior than MrCP20, which could affect efficient flow of the protein through the long SEC column. Not every SEC peak could be clearly assigned to a specific oligomeric species of MrCP19, so the whole range of peaks were collected by every 1.8 mL and analyzed by SDS-PAGE (**Figure 3.2**). The monomeric form of MrCP19 could be obtained from a small fraction of the elution peaks between 48-58 mL.

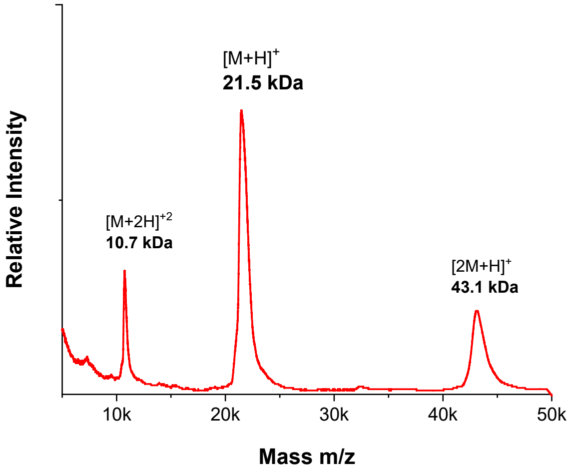

Figure 3.3 MALDI-TOF spectra of purified MrCP20 with a major peak at a MW at 21.5 kDa, corresponding to the theoretical value of 21.4 kDa.

MALDI-TOF was acquired for the purified MrCP20 (**Figure 3.3**). A single peak at 21.5 kDa was predominant, which matches the theoretical value of 21.4 kDa. Dimeric unit was present at 43.1 kDa, as well as double charged species at 10.7 kDa.

3.3.2 Secondary Structure Analysis

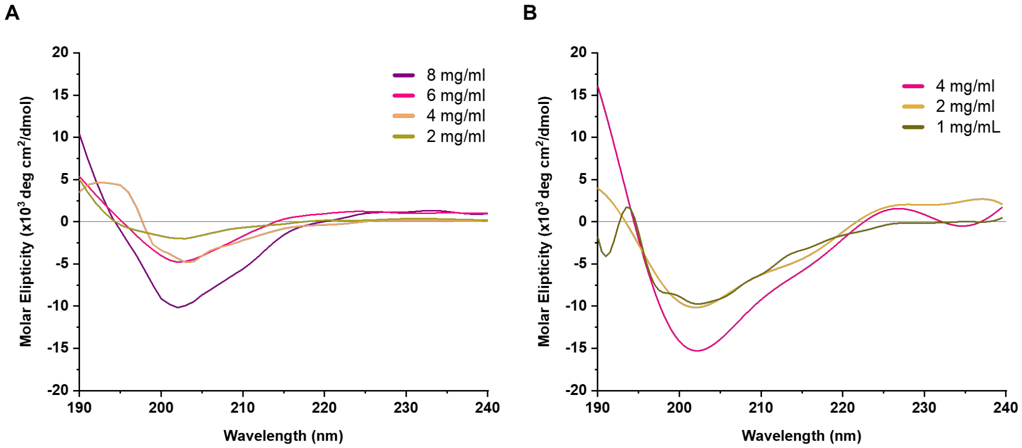

Figure 3.4 CD spectra of MrCP20 **(A)** in Tris or **(B)** in AA at different protein concentrations.

Far-UV CD spectra of recombinant MrCP20 shown in **Figure 3.4** at different protein concentrations indicates a mixture of β-sheet and random coil structure, exhibiting a minimum molar ellipticity around the wavelength of 202 nm.[9–11] These spectra match established CD data for the recombinant form of MrCP20.[12,13] The signal in the wavelength range of 200-210 nm became stronger with increasing protein concentrations. The pH shift from basic to acidic conditions did not shift the peak location but only increased its intensity.

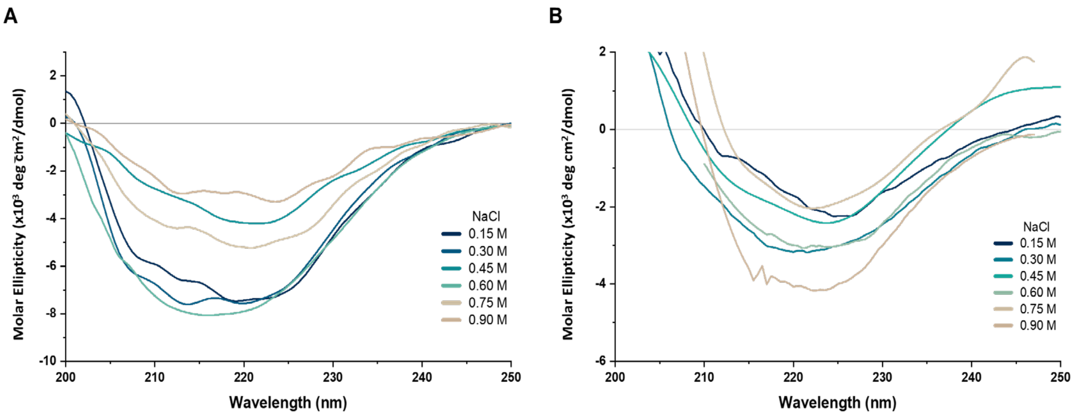

Figure 3.5 CD spectra of 1 mg/mL MrCP19 (**A**) in Tris or (**B**) in AA at different salt concentrations from 150 mM to 900 mM.

For MrCP19, it was challenging to achieve a concentration higher than 2 mg/mL due to the weak stability of the protein, which tended to aggregate. To measure the role of local dehydration of the protein without increasing the protein concentration, I conducted CD experiments with increasing salt concentration from 150 mM to 900 mM, as shown in **Figure 3.5**. The signal was not affected or slightly enhanced by the "salting in" effect at the salt concentration increasing to 450 mM. At higher amount of salt concentration in the buffer solution, the signal strongly diminished by a "salting out" effect. However, all the spectra showed the minimum molar ellipticity around the wavelength of 220 nm, which can be attributed to β-sheet structure.[9–11] The pH shift from basic to acidic conditions increased the contribution of β-sheet structure around the wavelength of 220 nm, and decreased the overall intensity and salt effect. Little hump with the 900 mM of salt and irregular edge of the curves in **Figure 3.5B** could be caused by the chloride ions adsorbing in the far UV range. The CD results indicate that MrCP19 was more likely to contain β-sheet structures expected for amyloid-like proteins, and thus more plausible to exhibit amyloid-like behavior than MrCP20.

3.3.3 Amyloid Fibrilization Investigation

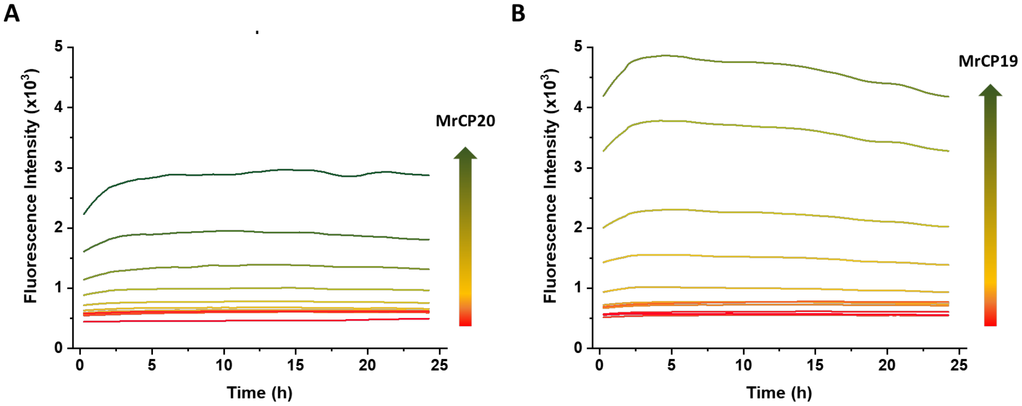

Figure 3.6 24 h fluorescence intensity measurement of **(A)** MrCP20 and **(B)** MrCP19 in Tris. The protein concentration was serially diluted in two-fold, starting from 1 mg/mL (green) to 0.002 mg/mL (red).

ThT assay was conducted to confirm β-sheet enrichment of MrCPs and the fluorescence intensity was measured. Both MrCPs showed protein concentration-dependent and time-independent result of the fluorescence intensity, and the intensity of MrCP19 was approximately double the intensity of MrCP20.

3.3.4 Homogeneity of MrCPs

To monitor the homogeneity, the protein samples in different concentration were characterized using DLS (**Figure 3.7-Figure 3.8**). The proteins had no correlated aggregation behaviour complied to the increasing protein concentration in the measurement range of 0.04 mg/mL ~ 1.0 mg/mL. MrCP19 showed already big radius in the very low concentration (**Figure 3.8B**). Different from all three other measurements which showed a coexistence of multiple populations, MrCP19 in acidic condition showed a single population at the size over 120 nm, without the presence of a smaller size distribution. Number and volume analysis of DLS confirmed that there was single population over 120 nm, while other three measurements indicated a single population around 4-5 nm for MrCP20 or 12-40 nm for MrCP19.

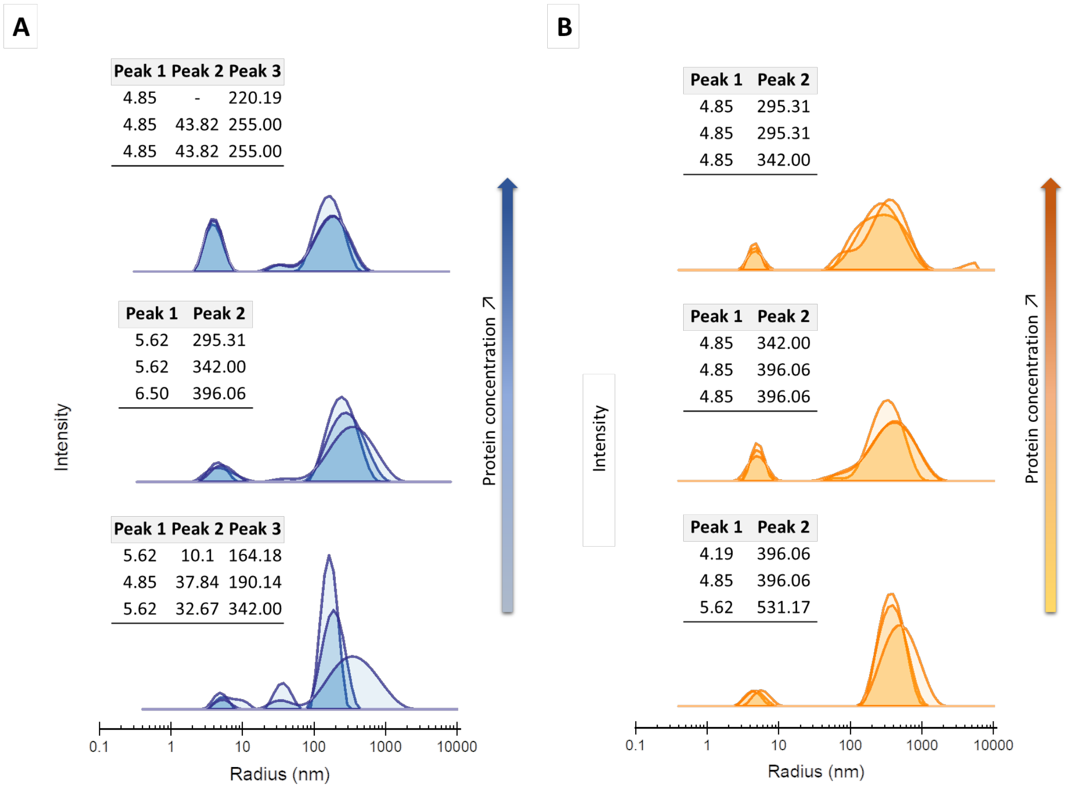

A

Peak 1	Peak 2	Peak 3
4.85	-	220.19
4.85	43.82	255.00
4.85	43.82	255.00

Peak 1	Peak 2
5.62	295.31
5.62	342.00
6.50	396.06

Peak 1	Peak 2	Peak 3
5.62	10.1	164.18
4.85	37.84	190.14
5.62	32.67	342.00

B

Peak 1	Peak 2
4.85	295.31
4.85	295.31
4.85	342.00

Peak 1	Peak 2
4.85	342.00
4.85	396.06
4.85	396.06

Peak 1	Peak 2
4.19	396.06
4.85	396.06
5.62	531.17

Figure 3.7 Hydrodynamic radius distribution of MrCP20 at (A) pH 8.3 and (B) pH 3.6. The protein concentrations are 1 mg/mL, 0.2 mg/mL, and 0.04 mg/mL from the top to the bottom,

and three measurement data are shown for each concentration. Peaks 1-3 are assigned in the order of ascending radius.

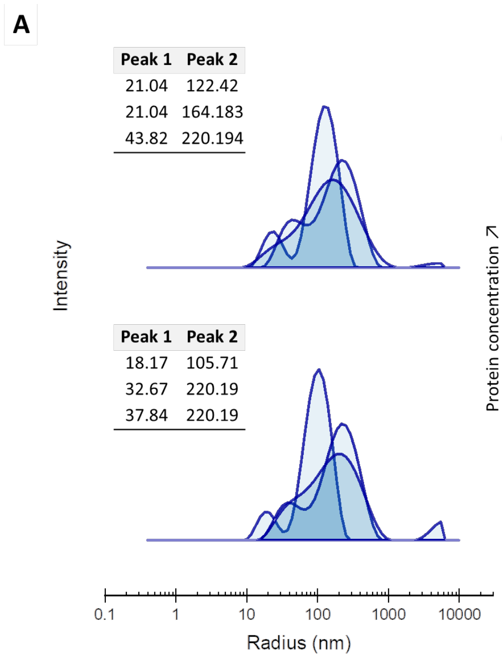

Peak 1	Peak 2
21.04	122.42
21.04	164.183
43.82	220.194

Peak 1	Peak 2
18.17	105.71
32.67	220.19
37.84	220.19

Peak 1
141.77
141.77
122.42

Peak 1	Peak 2
-	141.77
-	190.14
50.75	220.19

Figure 3.8 Hydrodynamic radius distribution of MrCP19 at (A) pH 8.3 and (B) pH 3.6. The protein concentrations are 0.2 mg/mL (**top**) and 0.04 mg/mL (**bottom**) and three measurement data are shown for each concentration. Peaks 1-2 are assigned in the order of ascending radius.

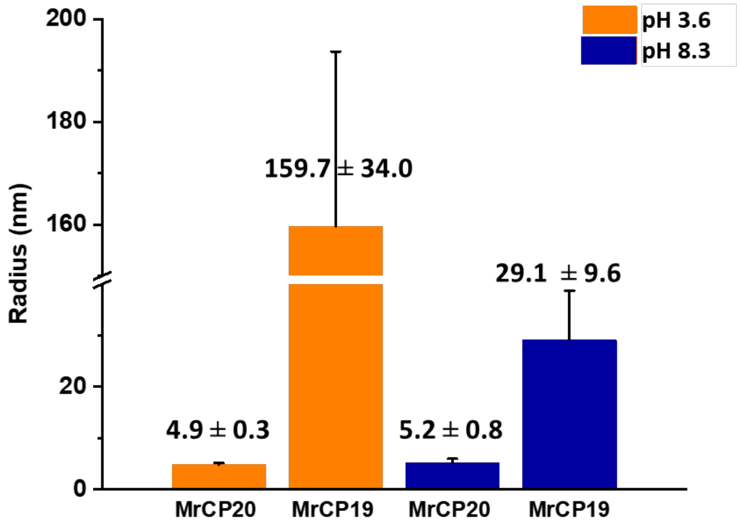

Figure 3.9 Hydrodynamic radius distribution of MrCP20 and MrCP19 at pH 3.6 in AA (orange), or at pH 8.3 in Tris (blue).

Accordingly, the hydrodynamic radius of MrCP20 in AA or Tris was recorded to be 4.9 ± 0.3 nm and 5.2 ± 0.8, respectively. (**Figure 3.9**) The hydrodynamic radius of MrCP19 in AA or Tris was estimated around 159.7 ± 34.0 nm and 29.1 ± 9.6, respectively. MrCP20 showed consistent and homogeneous hydrodynamic radius value at both pH conditions, while MrCP19 showed greatly increased value in acidic environment. MrCP19 may aggregate or exhibit amyloid fibrillation more easily than MrCP20, especially at acidic pH condition. On the other hand, MrCP19 in water (pH 7) showed multiple and broad peaks with a very large standard deviation, showing highly heterogenous solution possibly due its pI value (6.89). This value will be comparatively analyzed with the other experiments in this thesis.

3.3.5 Effect of pH on Protein Net Charge

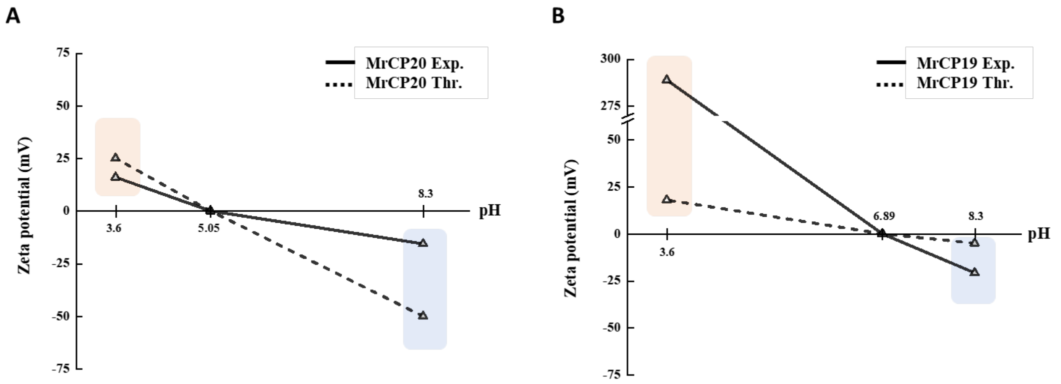

Figure 3.10 Theoretical protein net charge (dotted line added as guide to the eye) and experimental mean zeta potential (solid line added as guide to the eye) in different buffer condition obtained for (A) MrCP20 (pI = 5.05) and (B) MrCP19 (pI = 6.89). Both proteins are positively charged at pH 3.6, and negatively charged at pH 8.3.

Table 3.1 Theoretical and experimental zeta potential values of MrCP20 and MrCP19 in basic and acidic pH condition.

Protein	***MrCP20***		***MrCP19***	
Buffer	***AA***	***Tris***	***AA***	***Tris***
Theoretical zeta potential [mV]	+ 25	- 50	+ 15.6	- 5
Experimental Mean zeta potential [mV]	+ 16.0 ± 1.5	-15.6 ± 0.49	+ 288.9 ± 3.8	-20.8 ± 0.6

Prior to studying surface adsorption and adhesion behavior of MrCPs, we investigated the net surface charge the proteins compared to their theoretical values, as shown in **Figure 3.10** and **Table 3.1**. Both theoretically and experimentally, MrCPs were positively charged at pH 3.6, and negatively charged at pH 8.3. Experimental zeta potential values of MrCP20 indicated a less strongly charged protein compared to the theorical values, at both pH. On the other hand, MrCP19 tended to be strongly charged at both pH, especially at acidic pH. MrCP19 could have restructured itself upon pH drop to expose more positively charged residues at acidic pH. Together with the DLS result, this could cause exclusively great hydrodynamic radius of the protein in the solution, and the size effect on zeta potential calculation might have brought the great deviation.

3.4 Conclusion

Preliminary biophysical investigations were performed to obtain molecular features of MrCP19 and MrCP20. The proteins were soluble in Tris and AA buffer at pH 8.3 and pH 3.6, respectively. MrCP19 exhibited more β-sheet secondary structure compared to MrCP20 as observed by CD, which was also confirmed by ThT assay. Hydrodynamic radius of MrCP19 was a lot bigger than that of MrCP20 at both pH 8.3 and pH 3.6 as obtained by DLS. Zeta potential of the proteins were measured within the range of theoretical value except for MrCP19 in acidic condition, showing unusually great value, possibly related to its unique structural behavior. Taken together, CD, ThT assay, DLS, and Zeta potential allow us to conclude that MrCP19 more readily assembles into β-sheet structures than MrCP20, which is the characteristic feature of amyloid proteins. This fibrillation of MrCP19 can result in specific functionalities. Furthermore, the unique properties of MrCPs can be useful to investigate their functional roles as bioadhesives.

References

1. Reuveny, S., Kim, Y. J., Kemp, C. W. & Shiloach, J. Effect of temperature and oxygen on cell growth and recombinant protein production in insect cell cultures. *Appl Microbiol Biotechnol* **38,** (1993).
2. Ebbinghaus, S., Dhar, A., McDonald, J. D. & Gruebele, M. Protein folding stability and dynamics imaged in a living cell. *Nat Methods* **7,** 319–323 (2010).
3. Waldo, G. S., Standish, B. M., Berendzen, J. & Terwilliger, T. C. Rapid protein-folding assay using green fluorescent protein. *Nature biotechnology* **17,** 691–695 (1999).
4. Hawe, A., Sutter, M. & Jiskoot, W. Extrinsic fluorescent dyes as tools for protein characterization. *Pharmaceutical research* **25,** 1487–1499 (2008).
5. Bolder, S. G., Sagis, L. M., Venema, P. & van der Linden, E. Thioflavin T and birefringence assays to determine the conversion of proteins into fibrils. *Langmuir* **23,** 4144–4147 (2007).
6. LeVine III, H. [18] Quantification of β-sheet amyloid fibril structures with thioflavin T. *Methods in enzymology* **309,** 274–284 (1999).
7. Biancalana, M. & Koide, S. Molecular mechanism of Thioflavin-T binding to amyloid fibrils. *Biochimica et Biophysica Acta (BBA)-Proteins and Proteomics* **1804,** 1405–1412 (2010).
8. Gade Malmos, K., Blancas-Mejia, L. M., Weber, B., Buchner, J., Ramirez-Alvarado, M., Naiki, H. & Otzen, D. ThT 101: a primer on the use of thioflavin T to investigate amyloid formation. *Amyloid* **24,** 1–16 (2017).
9. Greenfield, N. J. & Fasman, G. D. Computed circular dichroism spectra for the evaluation of protein conformation. *Biochemistry* **8,** 4108–4116 (1969).
10. Brahms, S. & Brahms, J. Determination of protein secondary structure in solution by vacuum ultraviolet circular dichroism. *Journal of molecular biology* **138,** 149–178 (1980).
11. Greenfield, N. J. Using circular dichroism spectra to estimate protein secondary structure. *Nature protocols* **1,** 2876–2890 (2006).

12. Mori, Y., Urushida, Y., Nakano, M., Uchiyama, S. & Kamino, K. Calcitespecific coupling protein in barnacle underwater cement. *FEBS Journal* 11 (2007).
13. So, C. R., Liu, J., Fears, K. P., Leary, D. H., Golden, J. P. & Wahl, K. J. Self-assembly of protein nanofibrils orchestrates calcite step movement through selective nonchiral interactions. *ACS nano* **9,** 5782–5791 (2015).

Chapter 4 Surface Adsorption and Adhesion Behavior of MrCP19 and MrCP20

Barnacle has attracted significant interest for the robust and permanent attachment it confers to diverse underwater substrates through strong interaction of a multi-protein complex layer, "cement". However, the intermolecular interactions responsible for the strong adhesive properties of the barnacle cement remains poorly understood. Herein, the molecular characteristics of cement proteins (CPs) were studied to understand their contribution to the underwater adhesion properties of the cement complex. The nanoscale morphological features of recombinant cement proteins from the barnacle Megabalanus rosa (MrCP19 and MrCP20) adsorbed on metal oxide substrates were characterized using Atomic Force Microscopy (AFM) and Transmission Electron Microscopy (TEM), and their secondary structure using Attenuated Total Reflectance Fourier-Transform Infrared Spectroscopy (ATR-FTIR). The adsorption behavior of the CPs is evaluated using a Quartz Crystal Microbalance with Dissipation (QCM-D) monitoring. The adhesion force of each protein was analyzed via Surface Force Apparatus (SFA). These results demonstrated that the cement proteins exhibited the adhesion behavior according to their own molecular

structure and surface behavior, which provided fundamental insights into the molecular adhesion mechanism at interface.

4.1 Introduction

For barnacle, as one of the most efficient marine biofouling macro-organisms, adhesion is crucial for its survival during the transition from cyprid to juvenile, and necessary to maintain the permanent attachment as the juvenile grows into an adult barnacle. Adhesion is performed by deposition of an adhesive secreted from the cement glands located at the base plate. This adhesive layer, as an intermediate material between the outer substratum and the inner base plate, is required to provide strong adhesion and cohesion joining two different surfaces in aqueous environment.[1–3]

Multistep underwater adhesion involves removing weak boundary layers, wetting, establishing interfacial adhesion, and curing, which can be achieved by differently functioning components of bioadhesives.[4] Successful underwater attachment requires surface components to fulfill stable interfacial adhesion while the bulk components to develop strong bulk cohesion, as well as those components' interplay. Mussel adhesion system has been actively studied to represent a good example of the above theory.[5] There are interfacial proteins (foot protein-3 and -5) and internal linking proteins (foot protein-2 and -4), which are also cooperating each other. More interestingly, their attachment is regulated by *in-vivo* pH mediation regarding the biochemical structure of 3, 4-dihydroxyphenyl-l-alanine (DOPA).[6–10] Acid-mediated attachment is known to be not only limited to mussels but also applicable for other sessile organisms, such as sandcastle worms[11,12], cnidarian hydroids[13], and tunicates[14]. It may provide a significant potential for barnacle fouling mechanism.[15]

Recent studies on barnacles proteins have suggested some possible mechanisms behind their underwater adhesion capability. *Kamino*[16] speculated that CP19 and CP20 perform surface binding function via non-covalent interactions. *So et al.*[17,18] suggested different CP composition for *Amphibalanus Amphitrite* and *Megabalanus rosa (Mr)*, proposing that CP19 can play both interfacial adhesion and bulk cohesion roles. CP19[19] showed binding ability to wide variety of substrates, while CP20[20–23] showed specific binding to calcite base *via* chemical bonding rather than physical adhesion. CP19 abundant with positively charged groups was believed to displace surface bound water layer as well as the adsorbed cations on mineral substrates to promote the barnacle attachment.[4,10] CP19 contains a good amount of hydrophobic residues in addition to charged residues, and this heterogeneity has been proposed to achieve good asymmetric bridging between hydrophobic bulk cement and charged external substrates.[24] This supports the assumption that MrCP19 is located at the interface between cement and external substrate.

More importantly, the self-assembly behavior of MrCP19 into nanofibers in certain conditions and the resultant improved adhesive ability as well as resistance to basic and high-salinity seawater condition have been studied.[25,26] The nanofibrillar structure is observable not only from MrCP19 but throughout the barnacle cement layer as a form of amyloid fibers.[2,15,27,28] This unique molecular design is known to be beneficial for exceptional mechanical stability and resistance to enzymatic degradation.[29–32]

However, as molting and calcification of the base plate take place simultaneously with cement development and curing underneath the barnacle, the interaction between the proteinaceous secretion and external surfaces has yet to be fully investigated. The functional role of each individual cement component remains uncertain as well, due to their insoluble nature[18,27,33].

In this chapter, I aimed to understand barnacle's surface adsorption and adhesion behavior by studying MrCP20 and MrCP19, that have been suggested to play an important role in the wet resistance adhesion of barnacles. Mica and metal oxide surfaces were used to mimic the chemical environment of the immersed substrates that barnacles attach to[34,35]. The adsorption of the proteins on oxide surfaces in basic and acidic conditions was investigated using Quartz Crystal Microbalance with Dissipation monitoring (QCM-D), which is a highly suitable method to study protein-surface interactions as it allows real-time monitoring of mass and energy loss changes, providing quantitative and viscoelastic information on thin layers deposited on surfaces[36–38]. Surface morphology of the proteins with nanometer resolution was investigated *ex-situ* by atomic force microscopy (AFM) and transmission electron microscopy (TEM), whereas their secondary structure was analyzed using attenuated total reflectance Fourier-transform infrared spectroscopy (ATR-FTIR) to reveal conformational transitions upon their interaction with surfaces. Finally, the nanoscale adhesion behavior was evaluated using the surface force apparatus (SFA). Combined together, these experiments provide a deeper understanding of adsorption and adhesion behavior of MrCPs specific to their primary structures as well as the formation of nanofibrils on surfaces. This work also provides guidelines to design wet-resistant peptide adhesives inspired by barnacle CPs for biomedical applications.

4.2 Materials and Methods

4.2.1 Protein and Buffer Preparation

The codon-optimized gene encoding His6-tagged at the C-terminus of MrCP19 and MrCP20 were purchased from DNA 2.0 (Newark, California). The MrCP19 and MrCP20 genes were transformed into E. coli BL21 (DE3) competent cells with a heat shock method. Expression and purification methods for both MrCP19 and MrCP20 proteins were explained in **Chapter 3.2**. The purified proteins were dialyzed in basic buffer Tris or acidic buffer AA.

4.2.2 Protein Adsorption and Surface Secondary Structure Study by ATR-FTIR

ATR FTIR measurements were performed using a Bruker VERTEX v80 spectrometer. The spectrometer is equipped with A225/Q Platinum ATR and multiple crystals CRY diamond ATR plate. All measurements were done at a pressure of 25 Pa in the spectral range from 500 cm^{-1} to 7800 cm^{-1} with a spectral resolution 4 cm^{-1}. 1000 scans were acquired for the background, and 250 scans were acquired for each spectrum. Spectral analysis was performed using Omnic 9 software (Thermo Scientific). All samples were prepared in the same way of preparing AFM samples in **4.2.3**. Freshly cleaved mica discs (0.24 mm thickness) (JBG METAFIX, France) were used as substrate.

4.2.3 Protein Morphology Study Using AFM

The morphology and nanostructure of MrCP19 and MrCP20 on surface was investigated using AFM imaging. The micrographs were acquired with a Park system NX10 on non-contact mode in air after adsorbed in different pH conditions. Prepared samples were deposited on freshly cleaved Mica Discs (PELCO, 9.9 mm, TED PELLA), attached on round magnets. 10 µL of 0.05 mg/mL protein solution was adsorbed for 30 min and was subsequently washed with water to prevent salt crystallization. The discs were air dried. Soft tips (Non-contact or soft tapping mode Reflex coating AFM probes, NanoWorld Point probe, tip radius of curvature less than 8 nm) were used in the tapping mode. The obtained images were analyzed using SmartScanTM.

4.2.4 Protein Morphology Study Using TEM

The morphology of the protein MrCP19 was also investigated using Energy filtered Carl Zeiss TEM, LIBRA® 120 equipped with an in -column Omega spectrometer. 3 µL of the sample was applied on a grid made of copper with 400 mesh (TED PELLA, CA, USA) spacing. It was subsequently washed with a drop of water to reduce amount of salt and prevent salt crystallization on the grid, and air dried. The acceleration voltage was 120 kV.

4.2.5 Protein Adsorption Study Using QCM-D

Real time surface adsorption of MrCP19 and 20 on different oxide surfaces at different pH conditions was investigated using a QCM-D analyzer (Q-Sense, Biolin, Sweden) at 20 ± 0.05 °C. The instrument collects all the odd number harmonics from the first to the thirteenth, and the ninth harmonic of the fundamental resonance frequency was used for data analysis. Prior to the protein adsorption measurements, SiO_2 (QSX 303), TiO_2 (QSX 310), and Al_2O_3

(QSX 309) coated quartz crystals were rinsed with SDS and milliQ water following a protocol provided by the company.

The quartz crystals were inserted in the chambers and equilibrated with air and buffer flow (20 μL/min) until the signal stabilized, followed by injection of the samples with the same flow rate. MrCP19 and MrCP20 solutions at 0.1 mg/mL were prepared in either or AA. Each protein injection was followed by buffer wash for 10 min to remove weakly bound proteins. All the QCM-D measurements data were analyzed with Qtools and Origin software.

The adsorbed protein mass on the QCM sensor was calculated from the frequency shift, using the Sauerbrey equation, $\Delta m = - C\Delta f$, where Δm is mass per unit area, Δf is frequency shift (Hz), and C is the Sauerbrey constant (17.7 ng/cm^2 Hz). The frequency and dissipation data with the overtone of $n = 9$ are represented in the plots and compared to each other.

4.2.6 Protein Adhesion Study by SFA

The interaction forces between the CPs and the surface were measured by Surface Force Apparatus 2000. Freshly cleaved thin mica was used as a surface substrate, coated on reflective silver layer, and glued onto cylindrical glass disks (radius of curvature R = 2 cm) facing to each other at a right angle. The interaction force F between the two surfaces was measured as a function of the separation distance D, and the energy between the two surfaces is directly proportional to the normalized force F/R, according to the Derjaguin approximation[39].

MrCP19 and MrCP20 were prepared in Tris and AA to be 20 μg/mL. 30 μL of each sample was placed on the top mica surface, giving 30 min for protein adsorption. After gentle wash with the buffer solution to remove non-absorbed proteins, a drop of buffer solution was deposited on the bottom mica surface so that it could prevent drying of the protein sample when the two surfaces were mounted in the chamber and brought in close to form a capillary bridge without contact. The sample was thermally equilibrated for 20 min, which was monitored with FECO (fringes of equal chromatic order) by the spectrometer.

All the experiments were performed at room temperature of 22 °C in a dark room. The speed of surface approach/separation was controlled with the motor voltage of 3.5 V. This renders the speed of ~10 nm/sec for approach/separation for each run.

4.3 Results and Discussion

4.3.1 Effect of pH on Proteins' Surface Morphology

The amide I band from ATR-FTIR contains the signals from the peptide backbone, which is proportional to the adsorbed amount of proteins on the surface[40,41]. According to Yang et al.[42], the component bands of amide I band are assigned as follows: 1610-1638, 1640-1654, 1645-1662, 1663-1685, and 1685-1696 cm^{-1} for parallel β-sheet, random coil, α-helix, β-turn, and antiparallel β-sheet, respectively. In order to understand the relationship between proteins' structures and adsorption behaviors, fibrillization of each protein in each condition was assessed by quantifying the β-sheet component from the amide I band [42–45]. The original ATR-FTIR spectra of the proteins on mica (**Figure 4.1**) were obtained multiple times from different spots on surface, averaged, and background corrected with mica, between 2000 and 1200 cm^{-1}. Each spectrum was deconvoluted with secondary structure contributions of the amide I band together with the amide II band and side chains, with Gaussian profiles by using OPUS 5.5 software (**Figure 4.2**). Significant overlapping between random coil and a-helix, as well as β-turn and antiparallel β-sheet, made the assignment and separation challenging. The fitted curve (black) corresponded nicely with the original spectra (grey). The result of deconvolution is presented in **Table 4.2**.

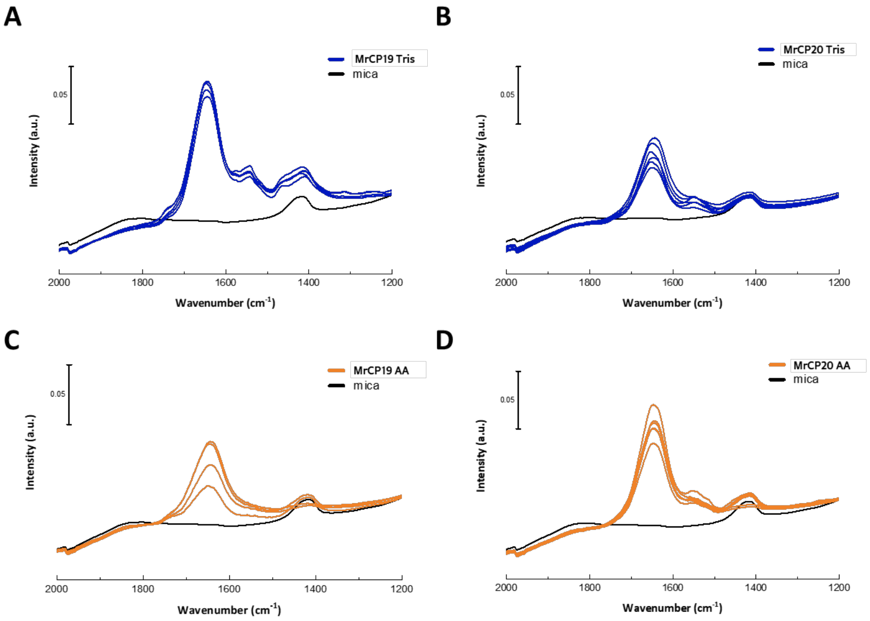

Figure 4.1 ATR-FTIR spectra of proteins adsorbed on mica surface were measured multiple times. (A) MrCP19 in Tris, (B) MrCP20 in Tris, (C) MrCP19 in AA, and (D) MrCP20 in AA.

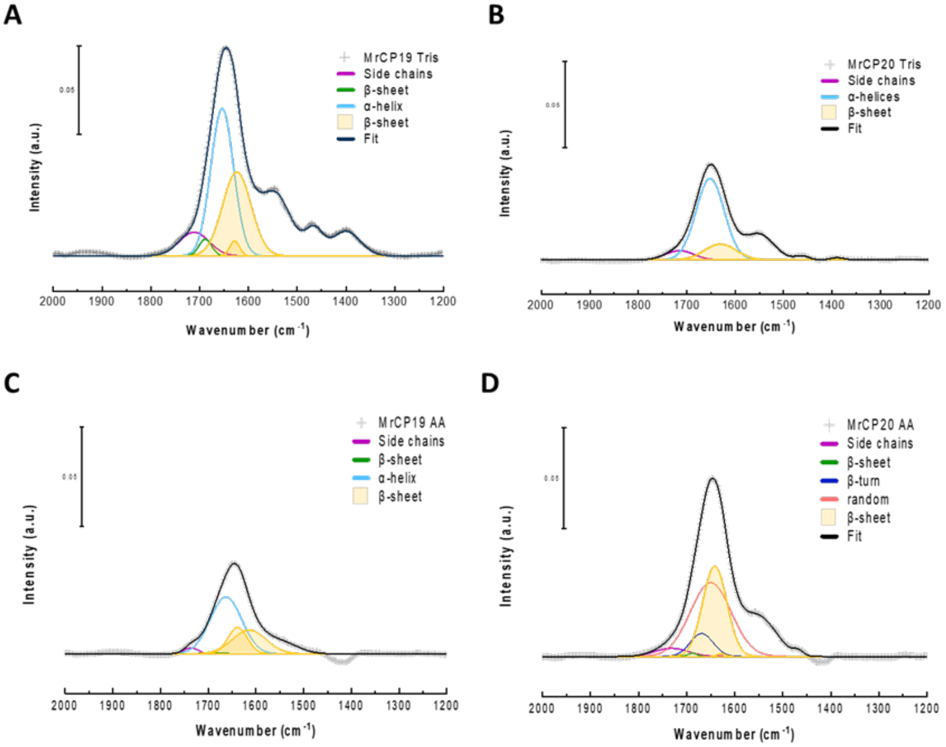

Figure 4.2 Deconvolution of amide I band from ATR-FTIR spectra of proteins adsorbed on mica surface. (A) MrCP19 in Tris, (B) MrCP20 in Tris, (C) MrCP19 in AA, and (D) MrCP20 in AA.

Table 4.1 Secondary structure content of each protein adsorbed on mica surface.

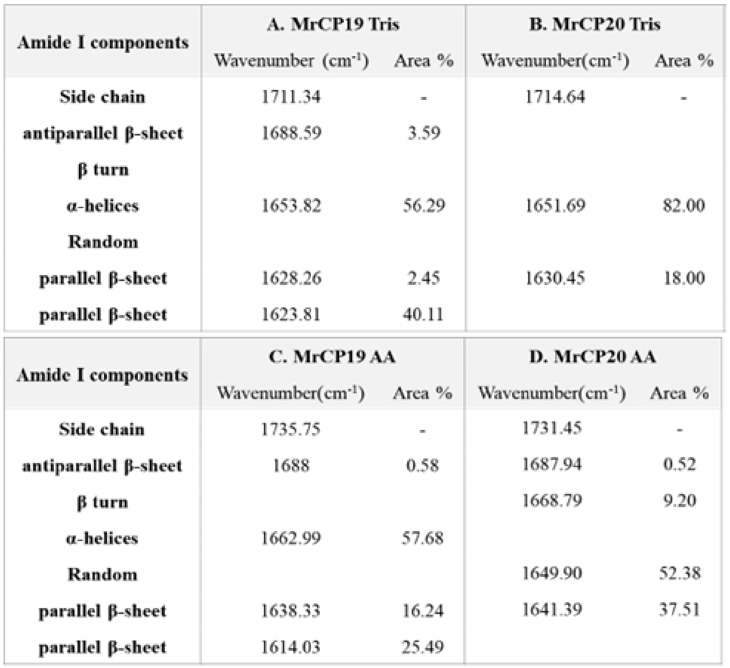

Amide I components	A. MrCP19 Tris		B. MrCP20 Tris	
	Wavenumber (cm⁻¹)	Area %	Wavenumber(cm⁻¹)	Area %
Side chain	1711.34	-	1714.64	-
antiparallel β-sheet	1688.59	3.59		
β turn				
α-helices	1653.82	56.29	1651.69	82.00
Random				
parallel β-sheet	1628.26	2.45	1630.45	18.00
parallel β-sheet	1623.81	40.11		

Amide I components	C. MrCP19 AA		D. MrCP20 AA	
	Wavenumber(cm⁻¹)	Area %	Wavenumber(cm⁻¹)	Area %
Side chain	1735.75	-	1731.45	-
antiparallel β-sheet	1688	0.58	1687.94	0.52
β turn			1668.79	9.20
α-helices	1662.99	57.68		
Random			1649.90	52.38
parallel β-sheet	1638.33	16.24	1641.39	37.51
parallel β-sheet	1614.03	25.49		

From the results above, the relative percentage of parallel β-sheet to the total amount of each protein adsorbed on surface is represented in **Figure 4.3**. Herein, the total amount of each protein was obtained by the averaged area under the amide I band. At basic pH, MrCP19 showed 2.4 fold higher adsorption than MrCP20, whereas at acidic pH MrCP20 was adsorbed 1.9 fold more than MrCP19. Accordingly, the quantity of β-sheet was calculated from the intensity of each protein adsorbed on surface and the contribution of beta sheet of each protein, to understand potential to form fibril structure. It is summarized in **Table 4.2**, and the expected potential to form fibril structure is ascending in the order of MrCP20 Tris < MrCP19 AA < MrCP20 AA < MrCP19 Tris.

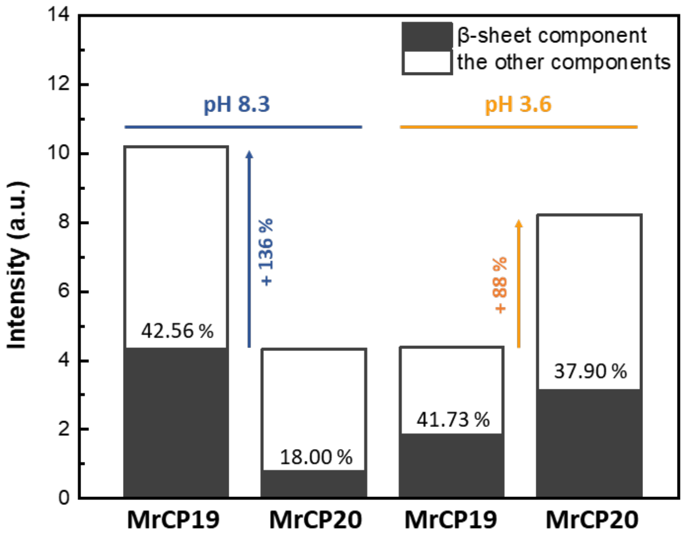

Figure 4.3 Amide I band intensity and β-sheet component obtained from ATR-FTIR. The adsorption trend of the two proteins on mica surfaces are opposite at the two different pH conditions.

Table 4.2 Amide I band intensity and β-sheet component obtained from ATR-FTIR

	Tris		AA	
	MrCP19	**MrCP20**	**MrCP19**	**MrCP20**
β-sheet (%)	42.6	18.0	41.7	37.9
Integrated area of Amide I (a.u.)	10.2	4.3	4.4	8.2
Integrated area of β-sheet (a.u.)	4.3	0.8	1.8	3.1

MrCP19 displayed a high β-sheet content > 40% at both pH conditions. For MrCP20, the β-sheet content also approached 40% at basic pH, but was significantly reduced (~ 20%) at acidic pH. These results were in good agreement with AFM observations (**Figure 4.4**), with nanofibrils observed for all three conditions where a β-sheet content in the 40% range was measured by ATR-FTIR. The height of the fibrils was mostly 2-4 nm range, while the group of fibrils observed with MrCP19 indicated the height of up to 10 nm. (**Figure 4.5**) The nanofibrils were shorter for MrCP20 in acidic conditions (**Figure 4.4D**), whereas they were more elongated for MrCP19, especially at basic pH (**Figure 4.4A**) and these results were further confirmed by TEM (**Figure 4.6**).

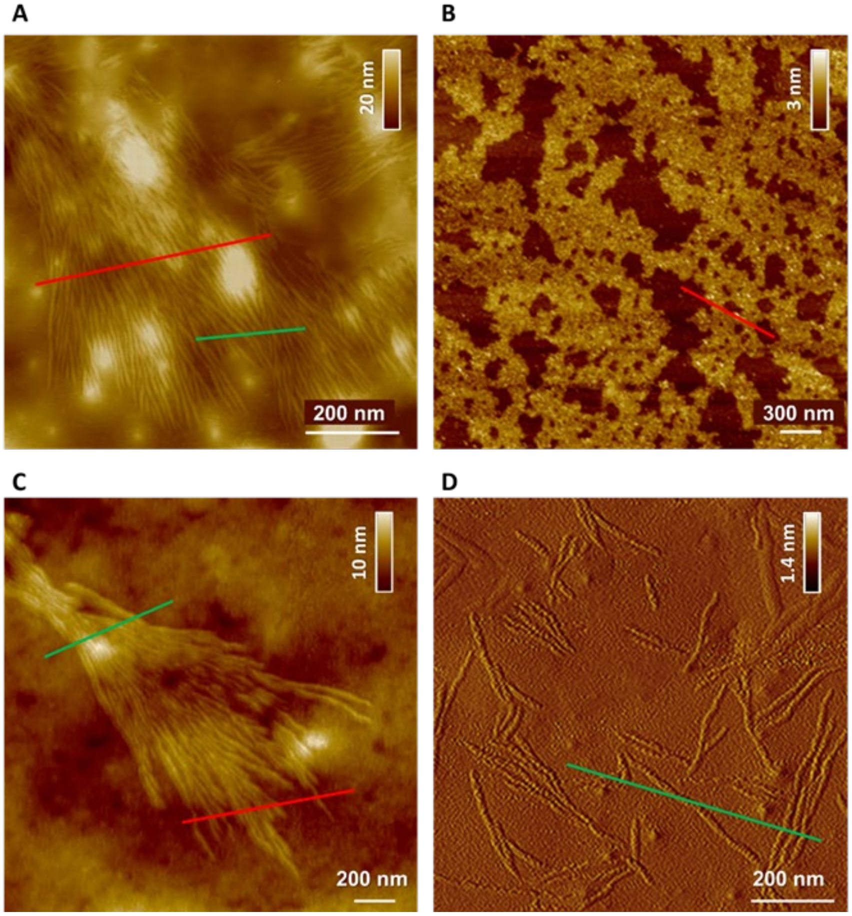

Figure 4.4 Representative AFM height images (A-C) and amplitude analysis (D) of 0.05 mg/mL of (A) MrCP19 and (B) MrCP20 in Tris, (C) MrCP19 and (D) MrCP20 in AA, adsorbed on mica surface. The red and green colored lines were drawn for height measurement.

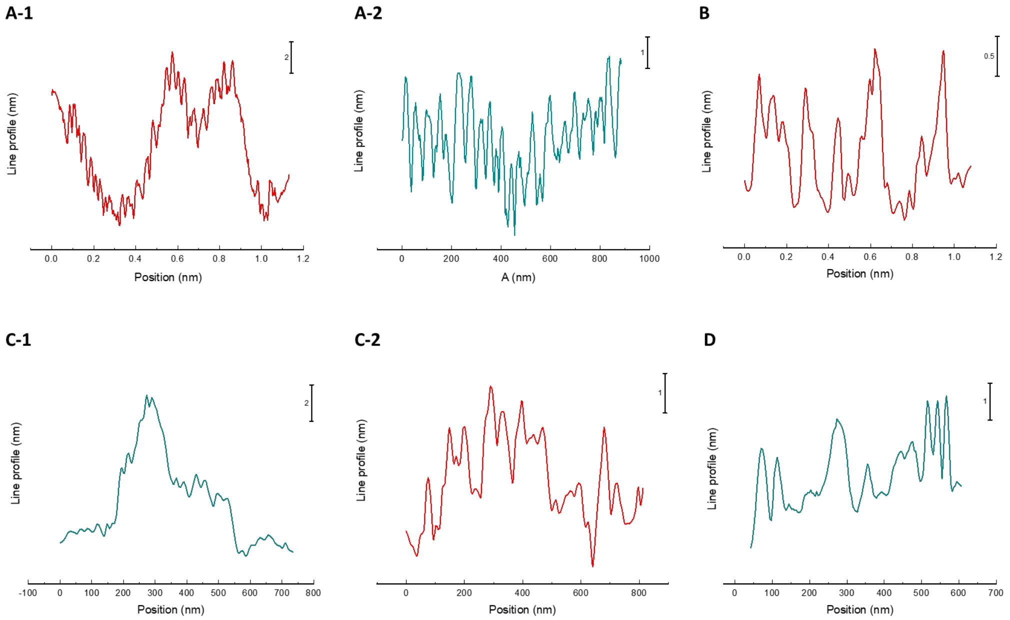

Figure 4.5 Height profiles of the protein structure from the selected region from Figure 4.4. Single fiber height was measured to be 2-4 nm.

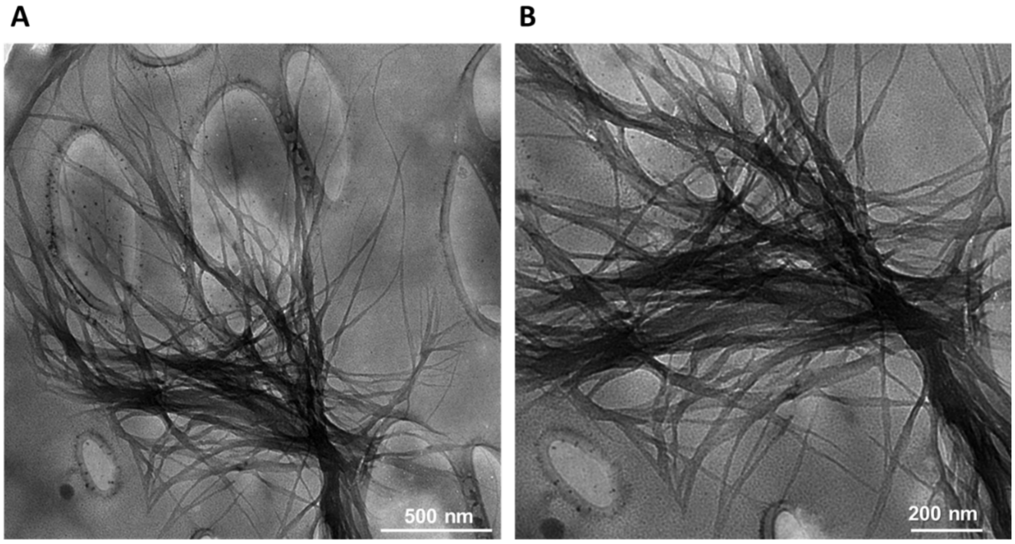

Figure 4.6 Representative TEM images of MrCP19 (0.1 mg/mL) in Tris buffer at pH 8.3, showing fibrous structure similar with the protein morphology observed by AFM.

4.3.2 Real-time Surface Adsorption and Viscoelasticity Study

Surface adsorption behavior of MrCP19 and MrCP20 on different oxide surfaces was studied by performing QCM-D measurements. **Figure 4.7** shows the shift of the resonance frequency *(Δf)* and dissipation *(ΔD)* as a function of time, which corresponds to hydrodynamically-adsorbed mass and viscoelasticity, respectively. The calculated hydrodynamic mass was represented in **Table 4.3**.

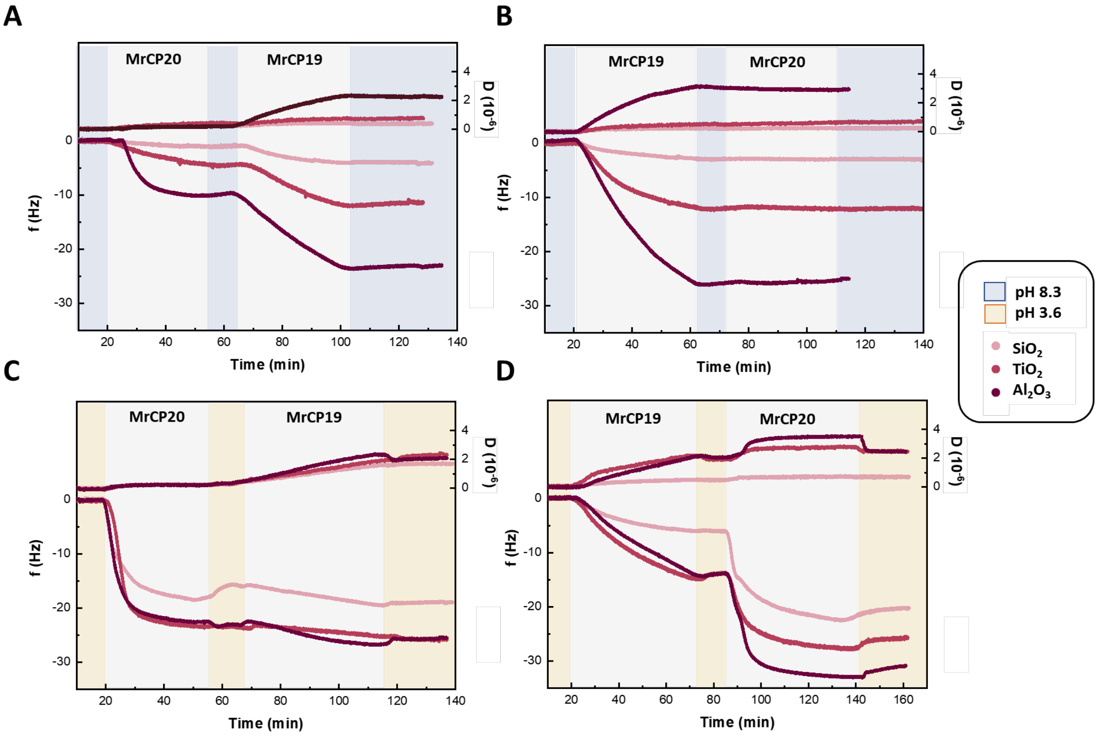

Figure 4.7 QCM-D frequency (f) and dissipation (D) shift as a function of time during adsorption of the proteins. (**A-B**) MrCP20 followed by MrCP19 (A) and MrCP19 followed by MrCP20 (B) at pH 8.3. (**C-D**) MrCP20 followed by MrCP19 (C) and MrCP19 followed by MrCP20 (D), at pH 3.6. Each protein adsorption was followed by 10 min buffer wash.

With the initial injection of MrCP20 in the basic buffer (**Figure 4.7A**), the frequency decreased by 1.5 Hz (SiO_2), 5 Hz (TiO_2), and 10 Hz (Al_2O_3), with saturation reached after 30 min, indicating the adsorption of MrCP20 on the surfaces. After rinsing with buffer, during which no protein desorption occurred, MrCP19 was flown for 40 min resulting in a further drop of the frequency to -4.5 Hz (SiO_2), -12 Hz (TiO_2), and -24 Hz (Al_2O_3), respectively. These data indicate that MrCP19 attached on the surfaces either by: *(i)* interacting with the oxide surface not covered by MrCP20, *(ii)* replacing some of surface bound MrCP20 proteins, or *(iii)* adsorbing on top of the first protein layer. The changes in the dissipation remained below 1×10^{-6}, except when MrCP19 was added on the Al_2O_3 surface.

Similarly, with the reversed order (namely MrCP19 followed by MrCP20), the frequency decreased by 4 Hz (SiO_2), 12 Hz (TiO_2), and 26 Hz (Al_2O_3) during the initial 40 min injection of MrCP19 (**Figure 4.7B**). Saturation was not reached, but the injection time was kept as 40 min for consistency with the other experiments. After buffer rinsing, MrCP20 was added without affecting both the frequency and dissipation. One of the possible reasons is that the high amount of hydrophobic residues of MrCP19 could induce strong hydrophobic interactions with each other on the surface, precluding the additional binding of the other protein. MrCP19's strong protein-protein interaction was evident in the form of nanofibril formation (**Figure 4.4-4.6**), which may prevent MrCP20 from either reaching the surface or binding to the MrCP19 protein matrix.

Comparing **Figure 4.7A** and **4.7B**, MrCP19 exhibited a higher binding affinity to all oxide surfaces than MrCP20, while the final surface coverages of the proteins after the second injection were similar. These results are consistent with the lower fraction of acidic residues in MrCP19, which should minimize electrostatic repulsion on negatively charged surfaces. Further, these results are in line with the point of zero charge (PZC) of these oxide surfaces. Indeed, the surface adsorption at pH 8.3 was the highest on Al_2O_3 (PZC = 8~9) followed by TiO_2 (PZC = 4.9), whereas it was the weakest on SiO_2 (PZC = 2.8).[46–51] The surfaces with higher PZC are more easily protonated thereby reducing electrostatic repulsion with the negatively-charged proteins.

Proteins in acidic buffer were injected with a similar sequence. When MrCP20 was injected first (**Figure 4.7C**), it adsorbed on the surfaces with frequency shifts $\Delta f = -18$ Hz (SiO_2), -24 Hz (TiO_2), and -23 Hz (Al_2O_3) respectively, with saturation reached after 30 min. Loosely bound proteins on SiO_2 were washed away after 10 min of buffer flow, reducing Δf to -16 Hz, while no desorption occurred on the other two surfaces. SiO_2 surface has a lower PZC value than TiO_2 and Al_2O_3, which is below pH 3.6 used in our experiments. Thus, the SiO_2 surface is not fully protonated and protein adsorption is weak and partially reversible, resulting in partial desorption. When MrCP19 was added for 50 min, the frequency showed a slow and linear decrease reaching -19 Hz (SiO_2), -25 Hz (TiO_2), and -27 Hz (Al_2O_3), respectively. Dissipation on all three surfaces increased in a linear fashion up to nearly 2×10^{-7}, forming relatively soft protein layers on the surface.

In the reversed order (injection of MrCP19 for 50 min followed by MrCP20, **Figure 4.7D**), the frequency initially dropped by 6 Hz on SiO_2, 16 Hz on TiO_2, and 16 Hz on Al_2O_3, while the dissipation increased up to 2×10^{-7} on TiO_2 and Al_2O_3 surfaces. Protein adsorption on TiO_2 and Al_2O_3 was showing a similar behavior as both surfaces are protonated at pH 3.6. After 10 min of rinsing, MrCP20 was added for another 50 min and the frequency dropped further to -23 Hz (SiO_2), -28 Hz (TiO_2), and -33 Hz (Al_2O_3), respectively. In contrast to basic pH conditions (**Figure 4.7B)**, MrCP20 was able to adsorb to the surfaces even if MrCP19 was initially bound. Especially upon additional binding of the second protein, the adsorbed layer on Al_2O_3 surfaces exhibited a higher dissipation up to 3.8×10^{-7}, which was recovered after the buffer rinse. These data suggest that MrCP20 could interact with the surface, resulting in a significant shift of frequency without affecting the viscoelastic property of the whole protein complex.

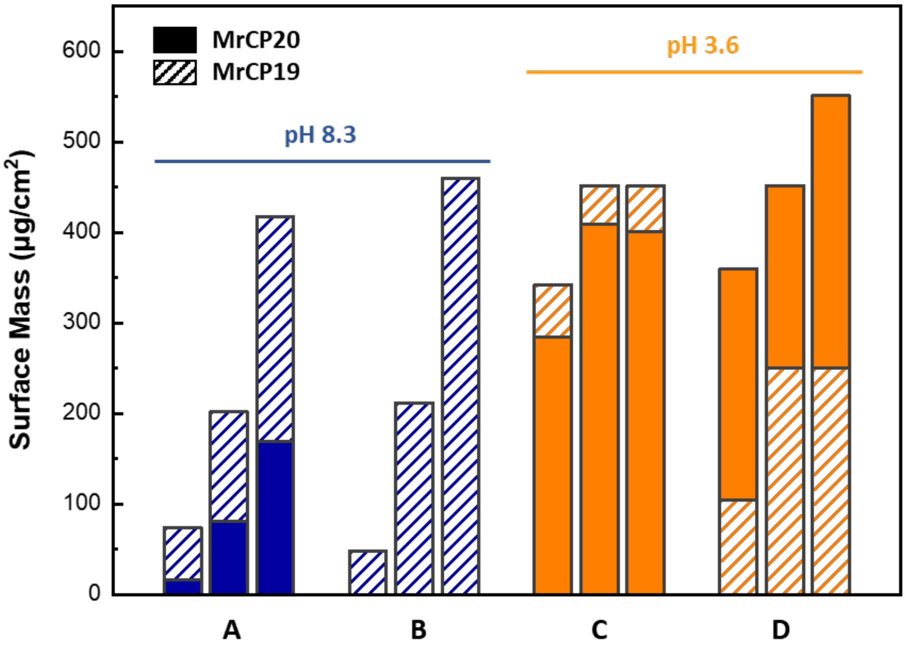

Figure 4.8 Hydrodynamic mass uptake (μg/cm2) calculated from QCM-D measurements using Sauerbrey Equation at (**A-B**) pH 8.3 and (**C-D**) pH 3.6, with the protein adsorption order of MrCP20-MrCP19 (**A, C**) and MrCP19-MrCP20 (**B, D**). The adsorption trend of the two proteins on bare oxide surfaces are opposite at the two different pH conditions. The final surface mass after the second injection is not influenced by the order of protein injection, but only by the pH conditions. Filled bar and non-filled bar represents MrCP20 and MrCP19, respectively. The three bars for each experimental condition **A-D** indicate SiO_2, TiO_2, and Al_2O_3 from left to right.

Table 4.3 Hydrodynamic mass uptake value (μg/cm^2) of adsorbed proteins on different oxide surfaces, averaged, at pH 8.3 and pH 3.6.

pH 8.3	A		B		pH 3.6	C		D	
μg/cm^2	MrCP20	+ MrCP19	MrCP19	+ MrCP20	μg/cm^2	MrCP20	+ MrCP19	MrCP19	+MrCP20
SiO_2	16	74	48	48	SiO_2	285	342	105	360
TiO_2	81	202	212	212	TiO_2	409	452	250	452
Al_2O_3	169	418	460	460	Al_2O_3	401	452	250	551
Avr.	88.67	231.33	240	240	Avr.	365	415.33	201.67	454.33
St.Dev	62.70	141.96	169.36	169.36	St.Dev	56.66	51.85	68.35	77.99

We note that the binding behavior of the two CPs on the surfaces were opposite between the two different pH conditions (**Figure 4.8** and **Table 4.3**). These relative adsorption behaviors are in a good agreement with the results obtained from ATR-FTIR experiments (**Figure 4.3**). Although the mica environment is not identical to the oxide surfaces employed in QCM -D experiments, the results are comparable to each other. Protein adsorption at basic pH showed better adsorption behavior using ATR-FTIR (static system) compared to QCM-D (dynamic system), since the protein solutions in static system was more advantageous for adsorption by providing more time until it was dried to adjust their confirmation on surface.

Higher adsorption onto the oxide surfaces was achieved for MrCP19 at basic pH, whereas MrCP20 adsorption was more pronounced at acidic pH. Indeed, adsorption of MrCP19 was similar at the two different pH conditions (**Figure 4.8B, D**), suggesting that MrCP19 surface adsorption is not strongly dependent on pH conditions and that other structural mechanisms play an important role on surface adsorption. In general, MrCP19 containing less acidic residues than MrCP20 is less affected by electrostatic repulsion at basic pH. Alternatively, MrCP20 with abundance in negatively charged residues showed stronger adsorption behavior at acidic pH.

MrCP19 mostly governed the viscoelastic properties of the protein complex at both pH, especially on positively charged surfaces showing linear increase of dissipation, while MrCP20 did not play a significant role on the dissipation. MrCP19 has flexible and dynamic structure[52] as well as hydrophobic nature and thus MrCP19 is inclined to reorient itself in favorable positions for fibril formation and protein-protein interaction on surface. As the surface coverage increased, the protein-protein interactions became the dominant parameter controlling dissipation. Rearrangement, self-assembly, or fibrillation took place which improved its capacity of surface adsorption in addition to direct interaction with the surface.[53–55] This also explains why we observed MrCP20 reaching saturation coverage much faster than MrCP19 at both pH.

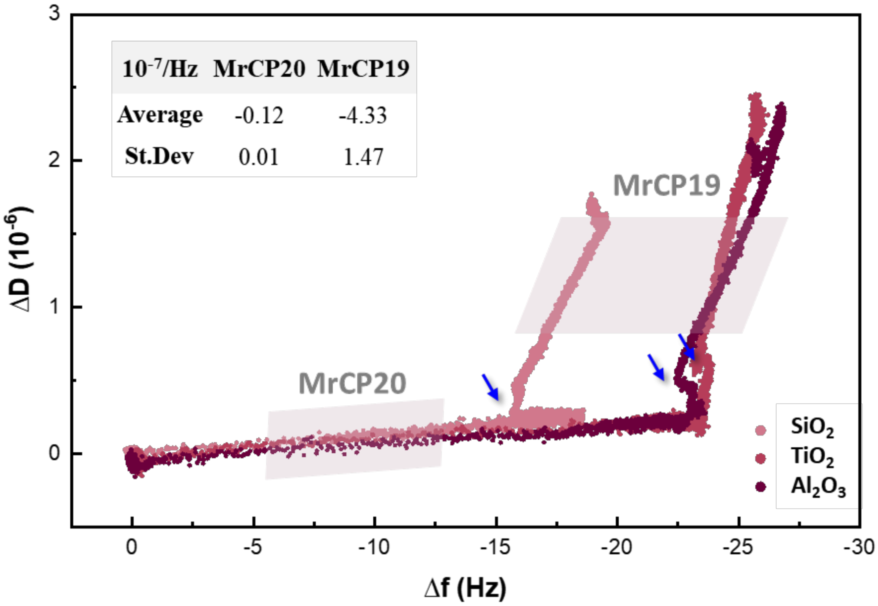

Figure 4.9 The dissipation shift (ΔD) normalized with the frequency shift (Δf) during proteins adsorption MrCP20 was injected, followed by MrCP19 at pH 3.6, and the blue arrows indicate the second protein injection.

Table 4.4 Normalized energy dissipation (ΔD/Δf) of MrCP19 on surfaces under different conditions, with **A-D** corresponding to **Figure 4.9**.

ΔD/Δf (10^{-7}/Hz)	**A**	**B**	**C**	**D**
SiO_2	0.46	0.98	3.12	0.69
TiO_2	0.47	0.46	6.36	1.25
Al_2O_3	1.8	1.3	3.52	1.5

To further analyze the viscoelasticity of MrCP19 films, the energy dissipation Δ*D* was normalized by Δ*f*, as such information provides the viscoelastic characteristics independent of adsorbed mass.[38,56] The linear fit of Δ*D*/Δ*f* slope of MrCP19 on the oxide surfaces for each condition was calculated.(**Table 4.4)** In basic pH condition, Al_2O_3 resulted in the softest MrCP19 layer among the three oxide surfaces with the highest Δ*D*/Δ*f* slope. The similar values of Δ*D*/Δ*f* slope at basic pH between **A** and **B** infers that MrCP19 attached on the oxide surfaces with a similar conformation regardless of the presence of MrCP20.

When MrCP19 was injected after MrCP20 in acidic condition, the average $\Delta D/\Delta f$ slope of the three surfaces showed a significant increase from 0.12 to 4.33 (10^{-7}/Hz), and it was the most dissipative layer from our experiments (**Figure 4.9**). Compared to the basic condition, where MrCP20 did not affect the dissipative behavior of MrCP19, the presence of MrCP20 highly enhanced the surface mobility of MrCP19 layer at acidic pH. Little amount of MrCP19 (0.9 μg/cm^2) could result in the most dissipative matrix, with the effect of substantial amount of MrCP20 on surface. Interactions with MrCP20 may have induced MrCP19 to take a more favorable conformation for fibrillization, such as exposing more hydrophobic residues. This viscoelastic behavior of the three different oxide surfaces was consistent regardless of the surface charge, and the $\Delta D/\Delta f$ slope was averaged in inserted in the **Figure 4.9**. On the other hand, MrCP19 injected first in acidic condition formed the most rigid layer on negatively charged SiO_2 compared to the other surfaces, where stronger attractive surface-protein interactions are known to inhibit fibrillization at interfaces.[57,58] The following MrCP20 contributed little to the viscoelastic property of the layer.

4.3.3 Protein Surface Adhesion Behavior

To further quantify the adhesive properties of MrCPs, we conducted SFA measurements. SFA provides the separation distance and the interaction force between two macroscopic surfaces with 0.1 nm and 10 nN resolution, respectively, and has been widely used to characterize the adhesive behavior of adsorbed layers.[59] During the experiments, the surfaces were brought together in contact and further compressed for one minute. Subsequently, the surfaces were separated by reversing the motor. Once the surfaces were separated, adhesion energy was calculated from the forces during jump-out events. The force *vs.* surface separation distance profiles were measured in different modes as shown in **Figure 4.10**, and the representative SFA curves are shown in **Figure 4.11-13**.

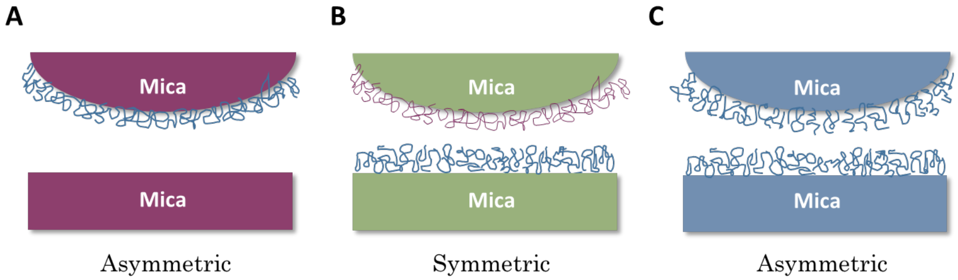

Figure 4.10 Schematic representation of symmetric and asymmetric modes of SFA. In our work, we use **A** for evaluating individual CP's surface adsorption behavior, **B** for cohesion between the two CPs, and **C** for cohesion of one protein followed by injection of the

First of all, the interactions between the proteins and bare mica surface were measured (MrCP19-mica, MrCP20-mica) (**Figure 4.11**). At pH 3.6, MrCP20 exhibited a relatively stronger adhesion energy of -1.25 mJ/m^2 in comparison to that of MrCP19 (-0.23 mJ/m^2), with values of adhesion comparable to that of DOPA-rich mussel adhesive proteins (mfp-2,3,5,6) on mica surface.[60,61] On the other hand, repulsive interactions for both proteins and the mica surface were noted at basic pH. The range of the repulsion, referred to the maximum distance where the force per radius raising above the noise level of 0.1 mN/m, was larger for MrCP19 (34.3 nm) than MrCP20 (13.3 nm). The thickness of the protein film can be inferred from the distance *D*, which is reached on approach at an applied load of 10 mN/m . It is also referred as the "hardwall", which provides information of the surface-surface separation at which the thickness of adsorbed layer becomes asymptotic upon with the increasing load.[62] The hardwall value was 9.4 nm for MrCP19 and 4.2 nm for MrCP20 at pH 8.3, and 3.4 nm for MrCP19 and 7.2 nm for MrCP20 at pH 3.6, respectively. These results agree with the relative adsorption amount of proteins measured at each pH condition. Moreover, MrCP19 adsorbed in basic pH condition formed the thickest layer, in agreement with the surface morphology observed from AFM as well as ATR-FTIR results, both of which indicating the largest amount of nanofibrillar morphologies on the surface. Considering that the thickness obtained by AFM measurements of single protein nanofibrils was 2-4 nm and group of protein fibrils was up ~10 nm (**Figure 4.4-5**), these results confirmed that MrCP19 does not form a uniform monolayer.

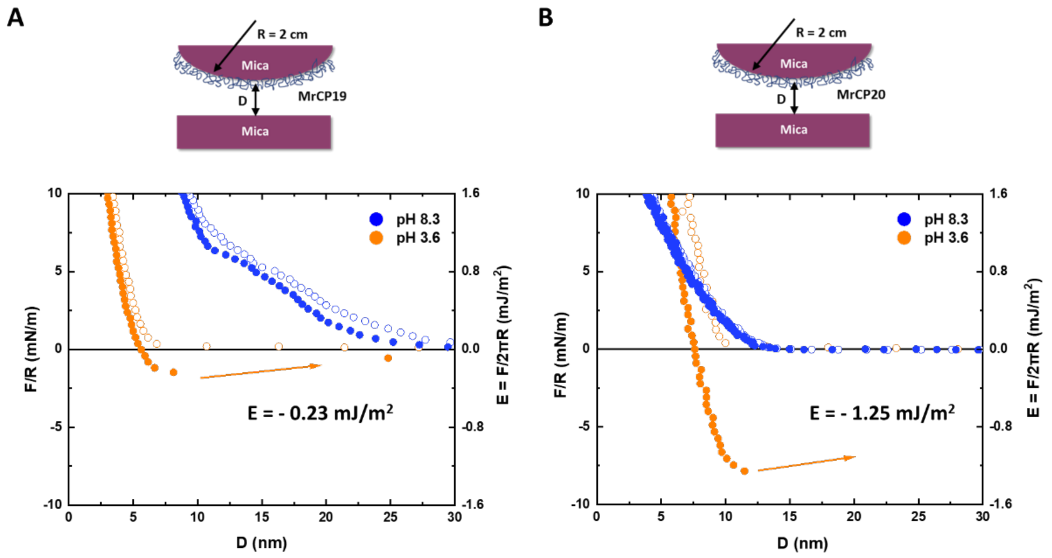

Figure 4.11 Representative normalized force (F/R) measured as a function of the mica-mica distance *D* with **(A)** MrCP19 and **(B)** MrCP20 deposited on the top surface at both basic (blue) and acidic (orange) pH conditions. Force curves measured on approach are indicated with open dots (○) and on separation with solid dots (●). No adhesion was observed for both proteins on mica in basic condition, but adhesion energy of -0.23 mJ/m^2 (MrCP19) and -1.25 mJ/m^2 (MrCP20) were measured in acidic conditions.

Both QCM-D and ATR-FTIR measurements showed that the adsorption of MrCP19 was stronger than MrCP20 at basic pH, whereas the opposite was observed at acidic pH and the SFA results corroborate these trends. At pH 8.3, no electrostatic attraction is expected between the negatively charged proteins and the negatively charged surfaces. Therefore, mica coated with MrCP19 (**Figure 4.11A**) showed stronger repulsive interactions than mica coated with MrCP20 (**Figure 4.11B**), as evidenced by repulsive forces occurring over a broader range of separation distances. Furthermore, repulsive interactions were further enhanced by steric repulsion arising due to the formation MrCP19 nanofibrils observed by AFM (**Figure 4.4**). At pH 3.6, on the other hand, the proteins are positively charged and SFA measurements indicate attractive interactions taking place upon surface separation between the proteins adsorbed on mica and the counter bare mica surface, with MrCP20 exhibiting almost 5-fold times stronger adhesion than MrCP19, attributed to higher hydrophilicity of the primary structure and stronger adsorption behavior observed by ATR-FTIR and QCM-D.

There are other surface interactions taking place between mica surfaces. In general, mica attracts each other with van der Waals (VdW) interactions[63] and ions and proteins in the solution can mitigate these attractive interactions. As the ionic strength of buffer solutions used for all our SFA measurements was 150 mM, hydrated Na^+ cations were expected to adsorb onto mica as outer-sphere species in basic pH, resulting in short-range (~1 nm) hydration forces.[64] It is possible that a small proportion of proteins formed complexes with these ions through the negatively charged domains of MrCP20 and hydrophilic domains of MrCP19. At acidic pH, there is less steric hydration repulsion occurring at the surface due to the neutralized surface charge.[63]

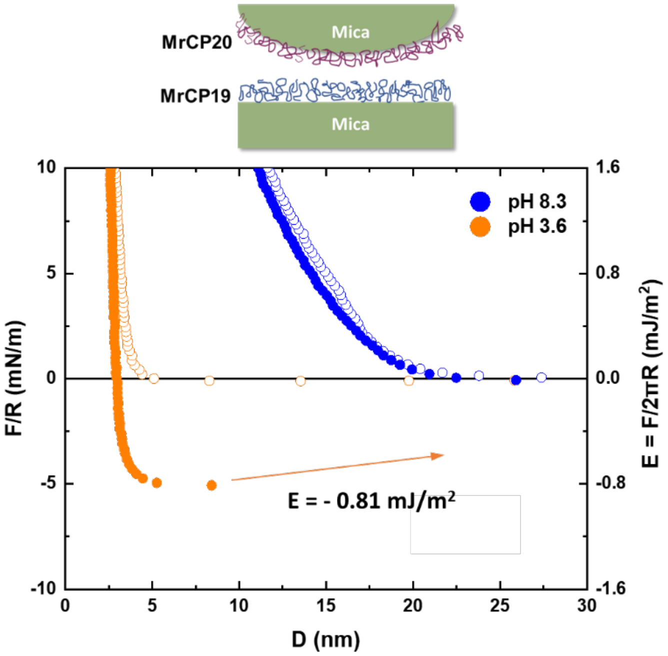

Figure 4.12 Interaction between MrCP19 and MrCP20 was measured at basic (blue) and acidic (orange) pH conditions. There was no adhesion observed at basic pH, with only repulsive interaction starting from 20 nm distance of approach. Adhesion energy of -0.81 mJ/m^2 was observed at acidic pH.

To identify possible interactions between MrCP19 and MrCP20, further experiments were conducted by adsorbing Mrcp19 on the bottom surface and MrCP20 on the top surface at pH 3.6 and pH 8.3 (MrCP19-MrCP20) (**Figure 4.12**). The SFA curves showed jump with adhesion energy of -0.81 mJ/m^2 at acidic pH, which is slightly weaker than that of MrCP20 deposited on one surface. On the other hand, there was no adhesion at basic pH between the two proteins on each surface, similar to the results of single deposition at basic pH.

The jumping stage of each experiment corresponds to full separation between two surfaces bridged by the adhesive proteins. It can be considered as the protein's maximum extension until it is fully detached from the surface. The distance at the instant of jumping instability may indicate the contour length of the protein in the case of monolayer deposition. MrCP19 and MrCP20 jumped when they stretched to 9 nm and 12 nm of length, respectively (**Figure 4.11**). This is a smaller value than the rough estimation for the linear chain of the proteins, which is about 70 nm for both (with an assumption of 3.5 Å per amino acid). At the same time, the SFA results of asymmetric deposition of the two proteins also showed a similar value of ~9 nm at the start of the jump-in instability (**Figure 4.12**). Considering the contour length, similar values of hardwall, and "jump-off" distance, **Figure 4.12** is comprehended as: *(i)* when both proteins are deposited and compressed upon approach, a dense compact layer composed of two proteins is formed. This is possible because of imperfect surface coverage of the proteins, leaving the mica surfaces partially uncovered; *(ii)* both surfaces are covered by positively charged proteins and possess electrostatic repulsion, which affects separation curves, and jump-off will occur before the proteins reach their maximum stretch length.

The three asymmetric adhesion measurements at basic pH **(Figure 4.11-12)** shows that the range of repulsion between MrCP19 and mica was twice larger than the other two measurements. Accordingly, the slope of the force-distance curve during the approach was showing the highest value for MrCP20-mica, and smaller values for MrCP19-MrCP20, and MrCP19-mica in descending order. It is possible to conclude that the compressibility of the MrCP20 film is larger since there are other factors affecting repulsion between the surfaces: *(i)* proteins' surface coverage on mica surface differs from each other; *(ii)* entropic repulsion is inevitable due to the loss of entropy during compression, also called steric repulsion[65,66]; and *(iii)* electrostatic repulsion also stems from the electrolytes of the buffer (NaCl in this case). Thus, the comparison of repulsive interaction will not be discussed in this report.

Critically, it is only possible to conclude that the slope of the force-distance profile is roughly proportional to the compressibility of the films.

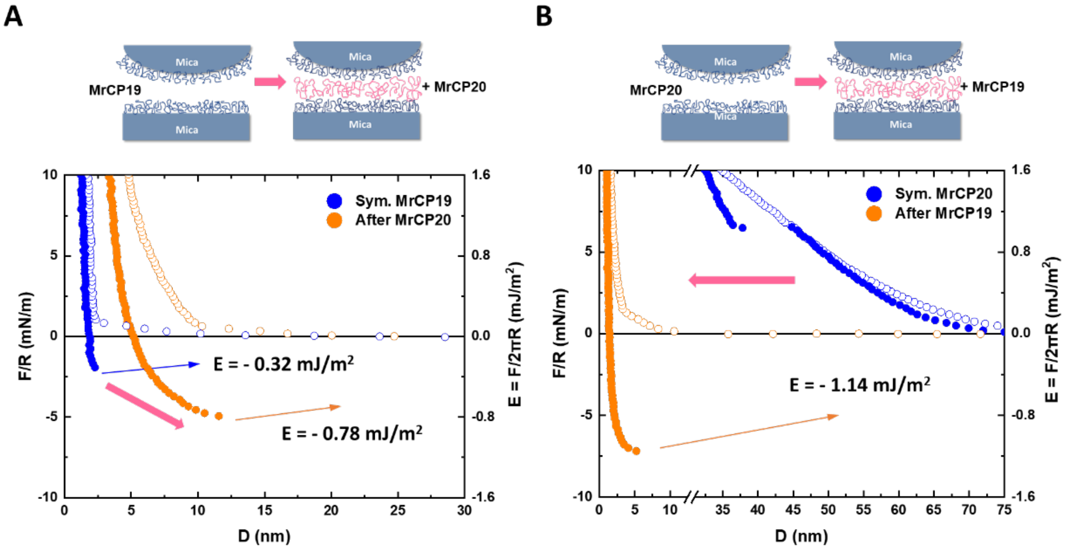

Figure 4.13 Interactions between MrCP19 and MrCP20 measured at pH3.6. **(A)** Geometry of the symmetric SFA measurement followed by injection of another protein. **(B)** Symmetric interaction of MrCP19 films showing interaction energy of -0.32 mJ/m^2, followed by Mrcp20 injection in between the surfaces, which increased the interaction energy to -0.78 mJ/m^2. **(C)** Symmetric interaction of MrCP20 films showing no adhesion but only thick repulsive interaction distance from 80 nm of approach. Adding MrCP19 in between the surfaces decreased the hardwall to 1 nm range and showed high adhesion energy of -1.14 mJ/m^2.

Further investigations on intermolecular interaction of each protein were conducted with symmetric deposition of each protein under acidic conditions (MrCP19-MrCP20-MrCP19 and MrCP20-MrCP19-MrCP20). Firstly, when Mrcp19 was deposited on both surfaces **(Figure 4.13A)**, adhesion energy of -0.32 mJ/m^2 was measured. Despite of the same charge of the protein films on both surfaces, protein-protein or fibril-fibril interaction took place and it enhanced the adhesion energy through strong cohesion, as amyloid fibrils are reported to significantly enhance mechanical stability[31,67–69].

Afterwards, MrCP20 in acidic condition was injected in between the surfaces, which brought stronger adhesion of E = -0.78 mJ/m^2. The hardwall increased from 2-4 nm to 6-8 nm range, as well as the range of repulsion during the approach from ~2 nm to ~11 nm. It shows that MrCP20 cannot fully infuse into the MrCP19 matrix, decreasing the compressibility. The adhesion could be favored even more strongly due to enhanced cohesive interactions between the proteins and entropy increase from depletion energy.[65]

On the other hand, when MrCP20 was deposited on both surfaces **(Figure 4.13B)**, the force curve showed different patterns from any other condition, with discontinuity in the repulsive force region. There was no adhesion between the symmetric films of MrCP20. Different from MrCP19, there was no specific structural behavior to compensate electrostatic repulsion between positively charged MrCP20. Huge repulsion range was observed, and the break point could be caused by the baseline correction or movement of the pathway. However, adhesion energy of -1.14 mJ/m^2 was measured after the injection of MrCP19 in between the surfaces. In addition to the previous discussion about increased cohesive interactions and entropy from depletion energy, MrCP19 possibly mediated bridging between the protein layers or moreover, flushed out MrCP20, and achieved thinner hardwall. MrCP19 possesses alternating binary patterns of charged residues and it can readily change and adjust its structure to favor self-assembly, which might minimize hydrophobic residues exposure to water molecules. As the self-assembled fibrils covered large amount of surface area, they dehydrated the surface efficiently. Surface dehydration (initially ordered water molecules being displaced from the surface) drove entropy gain and thus thermodynamically favored protein adsorption as a spontaneous and irreversible process, together with conformational changes.[70–72]

The summary of all the measurements with expected results and experimental results is shown in the **Table 4.5**.

Table 4.5 Summary of SFA measurements of MrCP19 and MrCP20 under different conditions

	Condition	**Adhesion Energy (-mJ/m^2)**		**Hardwall (nm)**	
	20 µg/mL	**pH 3**	**pH 8**	**pH 3**	**pH 8**
MrCP19-mica	Deposit	0.23	Repulsion	3-6	9-12
MrCP20-mica		1.25	Repulsion	8-10	4-6
MrCP19-MrCP20	Deposit each	0.81	Repulsion	2-4	12-14
	pH 3	**Deposit one**	**Inject another**	**Deposit**	**Inject**
MrCP19-20-19	Deposit - Wash - Inject	0.32	0.78	2-4	5-8
MrCP20-19-20		Repulsion	1.14	35-38	2-4

4.4 Conclusion

Protein adsorption and adhesion are complex processes, and it is essential to consider the nature of protein-surface interaction and kinetics, energetics, material chemistry, solution conditions (pH, ionic force, protein concentration, temperature), hydration layer, and so on. Thus, we evaluated surface adsorption and adhesion by analyzing basic protein properties and their morphology beyond chemical binding.

Our comparative studies of the two barnacle cement proteins MrCP19 and MrCP20 indicate that they exhibit specific structures on oxide and mica surfaces, with surface adhesion largely governed by electrostatic interactions. Under basic pH condition, no electrostatic attraction was observed between the negatively charged mica surface and the negatively charged proteins. Adsorption of MrCP19 on oxide surfaces was larger than MrCP20, with the formation of long nanofibrils, resulting in larger repulsive interactions compared to MrCP20. Under acidic pH condition, MrCP19 and MrCP20 are positively-charged and adhesion was detected on mica surface by SFA. The adsorption of MrCP20 on oxide surfaces was larger than MrCP19, due to electrostatic interactions via the acidic amino acid residues of MrCP20. For both pH conditions, MrCP19 self-assembled into larger nanofibrils owing to its primary structure and secondary structure abundant in β-sheet, thereby enhancing the overall dissipation of the adsorbed protein film on oxide surfaces. The nanofibrils of MrCP19 contribute not only to the viscoelastic behavior of the adsorbed protein layer but also to adhesion on mica with the effects of structure and entropy. From the barnacle's perspective, it is possible to have its own *in-vivo* mechanism to create an acidic environment during the cement secretion, before or even never getting exposed to the sea water condition. It is also interesting to observe the two proteins' collaborative adhesion activity between mica surfaces, which can provide an idea for designing a cement layer adhesion model as a whole composite. Our results cannot directly infer that fibrillation occurs upon the protein deposition on surface. However, the possibility that the fibrillation takes place after the deposition on the surface or upon dehydration cannot be ignored, as well as the possibility that reactions under the barnacle base plate in nature derives fibrillation. This can bring insights into the adsorption, adhesion and self-assembly characteristics of barnacle cement proteins on underwater mineral mimicking surfaces encountered in their natural environments.

References

1. Yule, A. B. & Walker, G. Settlement of Balanus Balanoides: The Effect of Cyprid Antennular Secretion. *Journal of the Marine Biological Association of the United Kingdom* **65,** 707–712 (1985).
2. Sullan, R. M. A., Gunari, N., Tanur, A. E., Chan, Y., Dickinson, G. H., Orihuela, B., Rittschof, D. & Walker, G. C. Nanoscale structures and mechanics of barnacle cement. *null* **25,** 263–275 (2009).
3. Burden, D. K., Spillmann, C. M., Everett, R. K., Barlow, D. E., Orihuela, B., Deschamps, J. R., Fears, K. P., Rittschof, D. & Wahl, K. J. Growth and development of the barnacle *Amphibalanus amphitrite*: time and spatially resolved structure and chemistry of the base plate. *Biofouling* **30,** 799–812 (2014).
4. Waite, J. H. Nature's underwater adhesive specialist. *International Journal of Adhesion and Adhesives* **7,** 9–14 (1987).
5. Waite, J. H. Mussel adhesion–essential footwork. *Journal of Experimental Biology* **220,** 517–530 (2017).
6. Niels Holten-Andersen, Harrington, M. J., Birkedal, H., Lee, B. P., Messersmith, P. B., Lee, K. Y. C. & Waite, J. H. pH-induced metal-ligand cross-links inspired by mussel yield self-healing polymer networks with near-covalent elastic moduli. *Proceedings of the National Academy of Sciences* **108,** 2651–2655 (2011).
7. Danner, E. W., Kan, Y., Hammer, M. U., Israelachvili, J. N. & Waite, J. H. Adhesion of mussel foot protein Mefp-5 to mica: an underwater superglue. *Biochemistry* **51,** 6511–6518 (2012).
8. Martinez Rodriguez, N. R., Das, S., Kaufman, Y., Israelachvili, J. N. & Waite, J. H. Interfacial pH during mussel adhesive plaque formation. *null* **31,** 221–227 (2015).
9. Razvag, Y., Gutkin, V. & Reches, M. Probing the interaction of individual amino acids with inorganic surfaces using atomic force spectroscopy. *Langmuir* **29,** 10102–10109 (2013).
10. Maier, G. P., Rapp, M. V., Waite, J. H., Israelachvili, J. N. & Butler, A. Adaptive synergy between catechol and lysine promotes wet adhesion by surface salt displacement. *Science* **349,** 628–632 (2015).

11. Stewart, R. J., Weaver, J. C., Morse, D. E. & Waite, J. H. The tube cement of Phragmatopoma californica: a solid foam. *Journal of experimental biology* **207,** 4727–4734 (2004).
12. Waite, J. H., Jensen, R. A. & Morse, D. E. Cement precursor proteins of the reef-building polychaete Phragmatopoma californica (Fewkes). *Biochemistry* **31,** 5733–5738 (1992).
13. Hwang, D. S., Masic, A., Prajatelistia, E., Iordachescu, M. & Waite, J. H. Marine hydroid perisarc: A chitin-and melanin-reinforced composite with DOPA–iron (III) complexes. *Acta biomaterialia* **9,** 8110–8117 (2013).
14. Dorsett, L. C., Hawkins, C. J., Grice, J. A., Lavin, M. F., Merefield, P. M., Parry, D. L. & Ross, I. L. Ferreascidin: a highly aromatic protein containing 3, 4-dihydroxyphenylalanine from the blood cells of a stolidobranch ascidian. *Biochemistry* **26,** 8078–8082 (1987).
15. Nakano, M. & Kamino, K. Amyloid-like conformation and interaction for the self-assembly in barnacle underwater cement. *Biochemistry* **54,** 826–835 (2015).
16. Kamino, K. in *Biological Adhesives* (ed. Smith, A. M.) 153–176 (Springer International Publishing, 2016). doi:10.1007/978-3-319-46082-6_7
17. So, C. R., Fears, K. P., Leary, D. H., Scancella, J. M., Wang, Z., Liu, J. L., Orihuela, B., Rittschof, D., Spillmann, C. M. & Wahl, K. J. Sequence basis of Barnacle Cement Nanostructure is Defined by Proteins with Silk Homology. *Sci Rep* **6,** 36219 (2016).
18. So, C. R., Scancella, J. M., Fears, K. P., Essock-Burns, T., Haynes, S. E., Leary, D. H., Diana, Z., Wang, C., North, S., Oh, C. S., Wang, Z., Orihuela, B., Rittschof, D., Spillmann, C. M. & Wahl, K. J. Oxidase Activity of the Barnacle Adhesive Interface Involves Peroxide-Dependent Catechol Oxidase and Lysyl Oxidase Enzymes. *ACS Appl. Mater. Interfaces* **9,** 11493–11505 (2017).
19. Urushida, Y., Nakano, M., Matsuda, S., Inoue, N., Kanai, S., Kitamura, N., Nishino, T. & Kamino, K. Identification and functional characterization of a novel barnacle cement protein. *The FEBS journal* **274,** 4336–4346 (2007).
20. Mori, Y., Urushida, Y., Nakano, M., Uchiyama, S. & Kamino, K. Calcitespecific coupling protein in barnacle underwater cement. *FEBS Journal* 11 (2007).

21. Kamino, K. Novel barnacle underwater adhesive protein is a charged amino acid-rich protein constituted by a Cys-rich repetitive sequence. 5 (2001).
22. So, C. R., Liu, J., Fears, K. P., Leary, D. H., Golden, J. P. & Wahl, K. J. Self-assembly of protein nanofibrils orchestrates calcite step movement through selective nonchiral interactions. *ACS nano* **9,** 5782–5791 (2015).
23. Lin, H.-C., Wong, Y. H., Tsang, L. M., Chu, K. H., Qian, P.-Y. & Chan, B. K. First study on gene expression of cement proteins and potential adhesion-related genes of a membranous-based barnacle as revealed from Next-Generation Sequencing technology. *Biofouling* **30,** 169–181 (2014).
24. Raman, S., Malms, L., Utzig, T., Shrestha, B. R., Stock, P., Krishnan, S. & Valtiner, M. Adhesive barnacle peptides exhibit a steric-driven design rule to enhance adhesion between asymmetric surfaces. *Colloids and Surfaces B: Biointerfaces* **152,** 42–48 (2017).
25. Liu, X. Amyloid fibril aggregation: An insight into the underwater adhesion of barnacle cement. *Biochemical and Biophysical Research Communications* 6 (2017).
26. Liang, C., Ye, Z., Xue, B., Zeng, L., Wu, W., Zhong, C., Cao, Y., Hu, B. & Messersmith, P. B. Self-assembled nanofibers for strong underwater adhesion: the trick of barnacles. *ACS applied materials & interfaces* **10,** 25017–25025 (2018).
27. Kamino, K., Inoue, K., Maruyama, T., Takamatsu, N., Harayama, S. & Shizuri, Y. Barnacle Cement Proteins. *Journal of Biological Chemistry* **275,** 27360–27365 (2000).
28. Barlow, D. E., Dickinson, G. H., Orihuela, B., Kulp III, J. L., Rittschof, D. & Wahl, K. J. Characterization of the adhesive plaque of the barnacle Balanus amphitrite: amyloid-like nanofibrils are a major component. *Langmuir* **26,** 6549–6556 (2010).
29. Fukuma, T., Mostaert, A. S. & Jarvis, S. P. Explanation for the mechanical strength of amyloid fibrils. *Tribology Letters* **22,** 233–237 (2006).
30. Smith, J. F., Knowles, T. P. J., Dobson, C. M., MacPhee, C. E. & Welland, M. E. Characterization of the nanoscale properties of individual amyloid fibrils. *Proc Natl Acad Sci USA* **103,** 15806 (2006).
31. Fowler, D. M., Koulov, A. V., Balch, W. E. & Kelly, J. W. Functional amyloid–from bacteria to humans. *Trends in biochemical sciences* **32,** 217–224 (2007).
32. Knowles, T. P. J. & Buehler, M. J. Nanomechanics of functional and pathological amyloid materials. *Nature Nanotechnology* **6,** 469–479 (2011).

33. Fears, K. P., Orihuela, B., Rittschof, D. & Wahl, K. J. Acorn Barnacles Secrete Phase-Separating Fluid to Clear Surfaces Ahead of Cement Deposition. *Adv. Sci.* **5,** 1700762 (2018).
34. Israelachvili, J. N., Alcantar, N. A., Maeda, N., Mates, T. E. & Ruths, M. Preparing Contamination-free Mica Substrates for Surface Characterization, Force Measurements, and Imaging. *Langmuir* **20,** 3616–3622 (2004).
35. Israelachvili, J. N. & Adams, G. E. Measurement of forces between two mica surfaces in aqueous electrolyte solutions in the range 0–100 nm. *J. Chem. Soc., Faraday Trans. 1* **74,** 975 (1978).
36. Dixon, M. C. Quartz Crystal Microbalance with Dissipation Monitoring: Enabling Real-Time Characterization of Biological Materials and Their Interactions. **19,** 8 (2008).
37. Hemmersam, A. G., Foss, M., Chevallier, J. & Besenbacher, F. Adsorption of fibrinogen on tantalum oxide, titanium oxide and gold studied by the QCM-D technique. *Colloids and Surfaces B: Biointerfaces* **43,** 208–215 (2005).
38. Hemmersam, A. G., Rechendorff, K., Foss, M., Sutherland, D. S. & Besenbacher, F. Fibronectin adsorption on gold, Ti-, and Ta-oxide investigated by QCM-D and RSA modelling. *Journal of colloid and interface science* **320,** 110–116 (2008).
39. Claesson, P. M., Ederth, T., Bergeron, V. & Rutland, M. W. Techniques for measuring surface forces. *Advances in colloid and interface science* **67,** 119–183 (1996).
40. Krimm, S. & Bandekar, J. in *Advances in Protein Chemistry* (eds. Anfinsen, C. B., Edsall, J. T. & Richards, F. M.) **38,** 181–364 (Academic Press, 1986).
41. Bandekar, J. Amide modes and protein conformation. *Biochimica et Biophysica Acta (BBA) - Protein Structure and Molecular Enzymology* **1120,** 123–143 (1992).
42. Yang, H., Yang, S., Kong, J., Dong, A. & Yu, S. Obtaining information about protein secondary structures in aqueous solution using Fourier transform IR spectroscopy. *Nat Protoc* **10,** 382–396 (2015).
43. Arrondo, J. L. R., Muga, A., Castresana, J. & Goñi, F. M. Quantitative studies of the structure of proteins in solution by fourier-transform infrared spectroscopy. *Progress in Biophysics and Molecular Biology* **59,** 23–56 (1993).
44. Kong, J. & Yu, S. Fourier Transform Infrared Spectroscopic Analysis of Protein Secondary Structures. *Acta Biochim Biophys Sinica* **39,** 549–559 (2007).

45. *Infrared Analysis of Peptides and Proteins: Principles and Applications*. **750,** (American Chemical Society, 1999).
46. McCafferty, E. The electrode kinetics of pit initiation on aluminum. *Corrosion Science* **37,** 481–492 (1995).
47. Balderas-Hernandez, P., Ibanez, J. G. & Godinez-Ramirez, J. J. Microscale Environmental Chemistry: Part 7. Estimation of the Point of Zero Charge (pzc) for Simple Metal Oxides by a Simplified Potentiometric Mass Titration Method. *The Chemical Educator* 4 (2006).
48. Yopps, J. A. & Fuerstenau, D. W. The zero point of charge of alpha-alumina. *Journal of Colloid Science* **19,** 61–71 (1964).
49. Vordonis, L., Koutsoukos, P. & Lycourghiotis, A. Determination of the point of zero charge, surface acidity constants, and relative concentration of the charged surface groups of γ-aluminas used as carriers. *Langmuir* **2,** 281–283 (1986).
50. Bourikas, K., Vakros, J., Kordulis, C. & Lycourghiotis, A. Potentiometric Mass Titrations: Experimental and Theoretical Establishment of a New Technique for Determining the Point of Zero Charge (PZC) of Metal (Hydr)Oxides. *J. Phys. Chem. B* **107,** 9441–9451 (2003).
51. Hervier, A., Blanchard, J., Costentin, G., Regalbuto, J., Louis, C. & Boujday, S. The genesis of a heterogeneous catalyst: in situ observation of a transition metal complex adsorbing onto an oxide surface in solution. *Chem. Commun.* **50,** 2409–2411 (2014).
52. So, C. R., Yates, E. A., Estrella, L. A., Fears, K. P., Schenck, A. M., Yip, C. M. & Wahl, K. J. Molecular Recognition of Structures Is Key in the Polymerization of Patterned Barnacle Adhesive Sequences. *ACS Nano* **13,** 5172–5183 (2019).
53. Rabe, M., Verdes, D. & Seeger, S. Understanding protein adsorption phenomena at solid surfaces. *Advances in Colloid and Interface Science* **162,** 87–106 (2011).
54. Déjardin, P. & Vasina, E. N. in *Proteins at Solid-Liquid Interfaces* (ed. Déjardin, P.) 51–73 (Springer Berlin Heidelberg, 2006). doi:10.1007/3-540-32658-8_3
55. Wertz, C. F. & Santore, M. M. Adsorption and Reorientation Kinetics of Lysozyme on Hydrophobic Surfaces. *Langmuir* **18,** 1190–1199 (2002).

56. Hemmersam, A. G., Foss, M., Chevallier, J. & Besenbacher, F. Adsorption of fibrinogen on tantalum oxide, titanium oxide and gold studied by the QCM-D technique. *Colloids Surf B Biointerfaces* **43,** 208–215 (2005).
57. Lin, Y.-C., Petersson, E. J. & Fakhraai, Z. Surface effects mediate self-assembly of amyloid-β peptides. *ACS nano* **8,** 10178–10186 (2014).
58. Shen, L., Adachi, T., Vanden Bout, D. & Zhu, X.-Y. A mobile precursor determines amyloid-β peptide fibril formation at interfaces. *Journal of the American Chemical Society* **134,** 14172–14178 (2012).
59. Israelachvili, J., Min, Y., Akbulut, M., Alig, A., Carver, G., Greene, W., Kristiansen, K., Meyer, E., Pesika, N., Rosenberg, K. & Zeng, H. Recent advances in the surface forces apparatus (SFA) technique. *Rep. Prog. Phys.* 17 (2010).
60. Yu, J., Wei, W., Danner, E., Ashley, R. K., Israelachvili, J. N. & Waite, J. H. Mussel protein adhesion depends on interprotein thiol-mediated redox modulation. *Nature chemical biology* **7,** 588–590 (2011).
61. Hwang, D. S., Zeng, H., Masic, A., Harrington, M. J., Israelachvili, J. N. & Waite, J. H. Protein- and Metal-dependent Interactions of a Prominent Protein in Mussel Adhesive Plaques*. *Journal of Biological Chemistry* **285,** 25850–25858 (2010).
62. Lu, Q., Wang, J., Faghihnejad, A., Zeng, H. & Liu, Y. Understanding the molecular interactions of lipopolysaccharides during E. coli initial adhesion with a surface forces apparatus. *Soft Matter* **7,** 9366–9379 (2011).
63. Dziadkowiec, J. & Røyne, A. Nanoscale Forces between Basal Mica Surfaces in Dicarboxylic Acid Solutions: Implications for Clay Aggregation in the Presence of Soluble Organic Acids. *Langmuir* **36,** 14978–14990 (2020).
64. Zachariah, Z., Espinosa-Marzal, R. M. & Heuberger, M. P. Ion specific hydration in nano-confined electrical double layers. *Journal of Colloid and Interface Science* **506,** 263–270 (2017).
65. Israelachvili, J. N. *Intermolecular and surface forces*. (Academic press, 2015).
66. Leckband, D. & Israelachvili, J. Intermolecular forces in biology. *Quarterly reviews of biophysics* **34,** 105–267 (2001).
67. Fukuma, T., Mostaert, A. S. & Jarvis, S. P. Explanation for the mechanical strength of amyloid fibrils. *Tribology Letters* **22,** 233–237 (2006).

68. Smith, A. M., Jahn, T. R., Ashcroft, A. E. & Radford, S. E. Direct observation of oligomeric species formed in the early stages of amyloid fibril formation using electrospray ionisation mass spectrometry. *Journal of molecular biology* **364,** 9–19 (2006).
69. Knowles, T. P. & Buehler, M. J. Nanomechanics of functional and pathological amyloid materials. *Nature nanotechnology* **6,** 469–479 (2011).
70. Desroches, M. J., Chaudhary, N. & Omanovic, S. PM-IRRAS investigation of the interaction of serum albumin and fibrinogen with a biomedical-grade stainless steel 316LVM surface. *Biomacromolecules* **8,** 2836–2844 (2007).
71. Huh, C. Interfacial tensions and solubilizing ability of a microemulsion phase that coexists with oil and brine. *Journal of colloid and interface science* **71,** 408–426 (1979).
72. Norde, W. Energy and entropy of protein adsorption. *Journal of dispersion science and technology* **13,** 363–377 (1992).

Chapter 5 Biomineralization and MrCP20

MrCP20 present within the calcareous base plate of the barnacle Megabalanus rosa (M. rosa) was investigated for its role in regulating biomineralization and growth of the barnacle base plate, as well as the influence of the mineral on the protein structure and corresponding functional role. I followed calcium carbonate growth on gold surfaces modified by mercaptoundecanoic acid (MUA/Au) with or without the protein using quartz crystal microbalance with dissipation (QCM-D) and identified the grown crystal morphology with Raman spectroscopy. I find that MrCP20 either in solution or on surface affects the kinetics of nucleation and growth of the crystal and stabilizes the metastable vaterite morphology of $CaCO_3$*. A comparative study using QCM-D Sauerbrey mass equation and quantitative X-ray photoelectron spectroscopy (XPS) determined that the final surface mass of the crystals as well as the crystallization kinetics is influenced by MrCP20. In addition, polarization modulated infrared reflection absorption spectroscopy (PM-IRRAS) study on MrCP20 amide band established that during crystal growth, the amount of β-sheet in MrCP20 increases, in line with evidence for amyloid-like fibril formation. The results provide insights into the molecular strategy by which MrCP20 regulate the overall biomineralization process at the cement layer, whilst* *favoring fibril formation which is advantageous for other functional roles such as adhesion and cohesion.*

5.1 Introduction

Barnacle's lifecycle begins with free-swimming nauplius larva stages. An early transition to the cyprid larva stage readies the organism to explore potential surfaces to settle down.[1,2] Once the cyprid (planktonic phase) successfully locates a conductive surface, it undergoes dramatic metamorphosis in the adhered state, first transforming into a juvenile barnacle (sessile phase) state, growing ultimately into the adult stage by expanding its base and side plates via processes of molting and calcification.[3–7] These hard calcareous shell plates are structurally robust and mechanically hard, evolved to not only protect the soft body tissue of the barnacle from the harsh, and often extreme, marine environment but also secrete an adhesive layer, which permanently binds the organism to foreign surface.[8]

Adhesion is crucial for barnacles' survival during the transition from cyprid to juvenile, and necessary to maintain the permanent attachment as the juvenile grows into an adult barnacle.[9–11] Adhesion is achieved by the deposition and curing of the adhesive cement layer, which exudes from the cement glands located at the base plate.[12–19] Acting as an intermediate material between the outer substratum and the inner base plate, this adhesive layer is also called upon to perform additional functional roles including surface binding and bulk cohesion, as well as coupling with the expanding base plate and the cuticle layer.[20,21]

Megabalanus rosa (M. rosa) is an acorn barnacle that has been extensively investigated. Its adhesive cement layer is composed of at least five different cement proteins (CPs).[22–25] Among these, the 20 kDa cement protein (MrCP20) has been suggested to play important roles in facilitating a robust attachment to the basal plate. The protein MrCP20 contains significant percentages of both negatively charged (Asp 11% and Glu 10%) and positively charged (Lys 5% and Arg 2%) residues. Together, these molecular features confer a high degree of conformational flexibility to the protein as revealed previously by solution-state nuclear magnetic resonance (NMR) spectroscopy and molecular dynamics (MD) simulations.[26,27] It appears that these same molecular attributes – namely the intrinsic balance of charged amino acids and the accompanying conformational flexibility – might also enable this protein to assume a critical role in facilitating the barnacle's underwater attachment, including regulation of biomineralization.

Recent studies on the interaction between MrCP20 and calcium carbonate base plate reveal the protein's major function on the barnacle's biomineralization.[21,22,28–32] *Kamino et al.*[24] suggested that MrCP20 promotes adsorption and adhesion binding the adhesive layer with the calcareous base plate through noncovalent and electrostatic interactions. *Mori et al.*[33] noted that MrCP20 adheres to calcite better than other minerals in marine environment. *So et al.*[34] revealed that MrCP20 exhibits special morphology on the {1014} face of the calcite surface and subsequently assembles into fibril formation with average thickness of 1.5 nm. *Kumar et al.*[27] performed molecular dynamic (MD) simulations of calcium carbonate ions surrounding MrCP20 protein, identifying electrostatic and water-mediated interaction between the calcium and carbonate ions, and charged amino acid residues. However, as molting and calcification of the base plate take place concurrently with the cement development and curing – which are all hidden underneath the barnacle – the molecular level interactions between the proteinaceous secretion and mineral surfaces has yet to be fully investigated.[15,21,35]

In this Chapter, I sought to examine the association of MrCP20 with calcium and carbonate ions during the entire mineralization process starting from the nucleation to the final phase transition, which determines the crystal habit. In order to achieve a high control over the $CaCO_3$ crystal growth on surface, self-assembled monolayers (SAMs) of 11-mercaptoundecanoic acid (MUA) with acidic functional group (-COOH) were formed on gold surfaces. MUA/Au surfaces are chemically well defined, and the crystal growth can be controlled by orientation of the terminal group.[36–38] The MUA possesses an even number of carbon chain that is known to orient the $CaCO_3$ crystal growth with (113) nucleating plane[39,40]. On these surfaces, I monitored $CaCO_3$ growth in the presence or absence of MrCP20 using quartz crystal microbalance with dissipation facility (QCM-D), and the surface mass of $CaCO_3$ was estimated using X-ray photoelectron spectrometry (XPS). The crystallographic structure of the $CaCO_3$ crystals was characterized by Raman spectroscopy. Molecular structure information of MrCP20 adsorbed on surfaces upon the crystal growth was studied with polarization modulated infrared reflection absorption spectroscopy (PM-IRRAS).

5.2 Materials and Methods

5.2.1 Protein and buffer preparation

The codon-optimized gene encoding His6-tagged at the C-terminus of mr19 and MrCP20 were purchased from DNA 2.0 (Newark, California). The MrCP20 genes was transformed into E. coli BL21 (DE3) competent cells with a heat shock method[41]. Expression and purification methods for both MrCP19 and MrCP20 proteins were performed following the protocol mentioned in *Mohanram et al*[26]. The purified proteins were dialyzed from basic buffer (20 mM Tris, 150 mM NaCl, pH 8.3) into $CaCl_2$ 10mM solution, and kept at 4˚C.

5.2.2 Surface functionalization

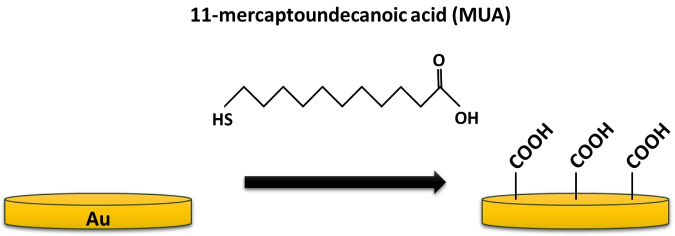

Figure 5.1 Schematic representation of gold surface functionalization with carboxylic acid-terminated alkanethiol, 11-mercaptoundecanoic acid (MUA)

QCM sensors from Biolin Scientific (Sweden) of a fundamental frequency of 5 MHz with a diameter of 14 mm, and gold coated substrates (Arrandee, Werther, Germany) with a width of 11 mm were used. Before they were functionalized, fresh gold coated substrates were rinsed in absolute ethanol, dried with nitrogen gas, and annealed in a butane/propane flame to obtain (111) crystalline surface direction. Then the surfaces were washed with water, dried with nitrogen gas, and exposed to ultraviolet radiation (UV ozone cleaner, ProCleaner™ Plus, BioForce Nanosciences) for 30 min. The gold coated substrates were immersed in solution of 11-mercaptoundecanoic acid (MUA) (95%, 450561, Sigma-Aldrich) in ethanol (1 mM, 5 mL/substrate) and left covered overnight with gentle agitation. The surfaces were then washed with ethanol, ultrasonicated for 30 s to remove thiol molecules not covalently bound to the gold surfaces and washed once again with ethanol followed by water.

5.2.3 $CaCO_3$ Mineralization by Vapor Diffusion

Slow-growth mineralization experiments were performed on MUA/Au (**Figure 5.2A**) following the well-established techniques of introducing ammonium carbonate vapor diffusion into calcium chloride solution, with the initial pH of 4.5.[36] This method is widely used for a slow crystallization, stable temperature, and great control of ion concentration.[42,43] The CO_2 gas was supplied by excessive amount of $(NH_4)_2CO_3$ powder located on a grove surrounding the surface (**Figure 5.2B**). The custom cuvette presented in the top figure was 3D printed in polylactic acid (PLA) using an Ultimaker 3 printer (Ultimaker, Utrecht, Netherlands). The CO_2 was diffused into 20 µL of 10 mM calcium chloride solution with MrCP20 or without MrCP20, and induced solid $CaCO_3$ formation.

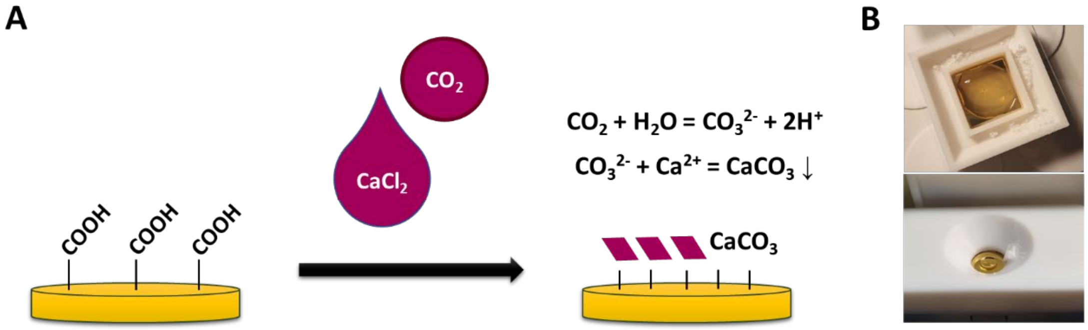

Figure 5.2 (A) Schematic representation of calcium carbonate formation on MUA/Au surface using vapor diffusion method. **(B)** 3D printed cuvette (top) and QCM-D open

module (bottom) for the experimental setup comprising a grove for $(NH_4)_2CO_3$ powder and sample on surface.

5.2.4 PM-IRRAS measurements

The samples were placed in the external beam of a Nicolet Nexus 5700 FT-IR spectrometer (Thermo Electron Scientific Instruments Corporation, Madison, WI USA). A ZnSe grid polarizer and ZnSe photo-elastic modulator were used to modulate the incident beam between *p* and *s* polarization of the sample. The spectrometer was interfaced to the UHV chamber via ZnSe windows. The reflected light was focused on a liquid nitrogen cooled Mercury-Cadmium-Telluride (MCT) wide-band detector at an optimal incident angle of 85°. The detector output was processed and undergo Fourier transformation to produce the PM-IRRA signal $(\Delta R/R0) = (Rp - Rs) / (Rp + Rs)$. All spectra were obtained with 128 and 256 scans at 8 cm^{-1} resolutions. The references for the peaks are taken from literatures and the peaks we used are shown in the **Table 5.1**.

Table 5.1 Vibrational assignment for different adsorption bands observed on PM-IRRAS spectrum.[44–48]

Chemical bonding	**Wavenumber (cm^{-1})**	**Assignment**
ν_{as} (CH_3)	2977-2985	Asymmetric stretch
ν_s (CH_3)	~2880	Symmetric stretch
ν_{as} (CH_2)	2920	Asymmetric stretch
ν_s (CH_2)	2852	Symmetric stretch
$\nu_{c=o}$ (COOH)	1740	Free carboxylic acid stretch
$\nu_{c=o}$(COOH)	1720	H-bonded carboxylic acid stretch
δ_{def}(NH)	1638	deformation of the NH end groups
ν_{as} (COO^-)	1600	Asymmetric carboxylate stretch
$\delta_{def}(NH_3^+)$	1565	deformation of NH3+ end groups
ν_{as} $(CO_3)^{2-}$	1500	Asymmetric stretching in ab plane

$\delta_s\,(CH_2)$	1468	Methylene scissors deformation
$\nu_s\,(COO^-)$	1400	Symmetric carboxylate stretch
$\delta_s\,(CO_3)^{2-}$	860	Out of plane bending vibration along c
$\delta_{as}\,(CO_3)^{2-}$	710	Out of plane bending vibration in ab

5.2.5 QCM-D

The growth of crystals on the SAM-modified QCM sensor surface was performed using Q-Sense explorer (Biolin, Sweden). Upon starting the measurement using Qsoft, the quartz crystal was embedded in the open module (QCM 401) and equilibrated with air until the signal stabilized. Once the resonant frequency stabilized at ±1 Hz in air, 20 μL of 10 mM $CaCl_2$ solution was injected into the open cell. After stabilization of the solution, excess $(NH_4)_2CO_3$ was located aside the solution to supply CO_2. The response of the QCM sensor was recorded and analyzed using Qtools and Origin software. The adsorbed mass on the QCM sensor was calculated following Saurbrey equation (**eq. 1**), which is applicable when the adsorbed layer is rigid.

$$\Delta m = -\frac{C}{N}\Delta f \qquad \textbf{(eq. 1)}$$

Where C is the Sauerbrey constant (17.7 ng/cm^2Hz for an AT-cut quartz crystal with a fundamental frequency of 5 MHz) and N is the number of harmonic waves. In this study, the third resonance ($N = 3$) is shown in the figures and used for all mass calculations, which was comparable to Kelvin-Voigt model calculation.[49–51]

5.2.6 Raman spectroscopy

The Raman spectra were recorded on a commercial RAMAN RXN1 analyzer (Kaiser Optical Systems, Inc.) equipped with a high-powered near-IR laser diode working at 785 nm.

A CCD detector with 1024×256 pixels provides full spectral collection of Raman data from 100 to 3450 cm^{-1} with a resolution of 4 cm^{-1} and holographic notch filters. Before spectra acquisition, an optical microscope (Leica, objective x50) was used to focus the laser beam on the surface. The laser output power was 100 mW. For each spectrum, 16 acquisitions of 40 s were recorded to improve the signal-to-noise ratio. To ensure a representative characterization of surfaces, a minimum of ten measurements were taken on different crystal structures on the surface.

5.2.7 Optical Microscopy

Optical microscope images of $CaCO_3$ crystals were taken using Olympus Microscope (U-CMAD3 and BX51M, Japan) and TopView software.

5.2.8 X-ray photoelectron spectrometer (XPS)

XPS analysis was performed by using a PHOIBOS 100 X-ray photoelectron spectrometer from SPECS GmbH (Berlin, Germany) with a monochromatic Al Kα X-ray source (hν =1486.6 eV) operating at 1×10^{-10} Torr. The spectra were recorded with a 100 eV pass energy for the survey scan and a 20 eV pass energy for the Ca 2s, C 1s, O 1s, N 1s, S 2p, and Au 4d regions. The photoelectron collection angle θ between the normal to the sample surface and the analyzer axis was 0˚. The data treatment was carried out using Casa XPS software (Casa Software Ltd., UK). The Ca 2s peak was decomposed using a linear baseline, and the Au $4d_{5/2}$ peak was decomposed using a U2 Tougaard baseline and applied with Gaussian/Lorentzian ratio (G/L) of 92 and asymmetric Gelius function of (0.2,0.1,0).

Quantitative information of surface mass can be obtained from Beer-Lambert law (**eq. 2**) and structural modeling of the crystals (**eq. 3**). The parameters are as follow: I is photoelectron intensity, A is the analyzed area, n is the number density of atoms, C is a constant involving sensitivity and geometric factors, $\exp(-\frac{z}{\lambda\cos\theta})$ is a contribution of part of the electrons that have not suffered inelastic collisions, where z is the thickness of the material, λ ,the attenuation length for a photoelectron emitted within a uniform material, and θ the photoelectron collection angle (0° in this work).

$$I = A\, n\, \sigma\, C\, exp\left(-\frac{z}{\lambda\, cos\theta}\right) dz \qquad \textbf{(eq. 2)}$$

A cubic model was chosen for the $CaCO_3$ crystals rather than sphere or hemisphere models, which is closer to the actual crystal structure. The parameters in the equation are as follow: m is the surface mass, l is the cubic length of crystal , Θ is the $CaCO_3$ coverage, and ρ is density.

$$m_{CaCO3} = \Theta l \rho_{CaCO_3} \qquad \textbf{(eq. 3)}$$

The crystal surface mass value can be estimated by using the ratio of photoelectron intensity coming from $CaCO_3$ and Au surface with **eqs. 2-3**. Especially the intensity ration of Ca 2s to Au 4d was used as the mean free path of the electrons from Ca 2s and Au 4d are similar and the result is not affected by the carbon layer. The intensity values were taken from the areas of the Ca 2s and Au $4d_{5/2}$ peaks.

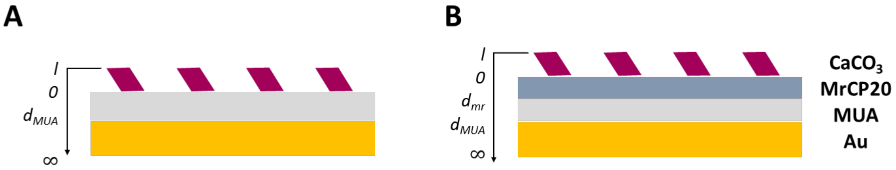

Figure 5.3 Schematic representation of two different surface models of XPS measurements, (**A**) without or (**B**) with the homogenous protein layer on the outermost surface. The different layers are indicated on the left side of each scheme. l is the cubic length of $CaCO_3$ crystal, d_{mr} is the thickness of protein adsorbed layer, d_{MUA} is the thickness of MUA layer. The maximum XPS depth analysis (with photoelectron collection angle of 0°) is around 10 nm.

According to the model A (**Figure 5.3**), the I_{Ca2s}/I_{Au4d} can be calculated as follows (**eqs. 4-6**). The parameters in the following equations represent; M_x is molecular weight of x (g/mol), σ_x is the sensitivity factor including scofield photoionization cross section and transmission function, d is the layer thicknes, θ is the photoelectron collection angle (0° in this work), and λ_x^y is inelastic mean free paths of electrons x in the matrix y, calculated using the Quases program based on the TPP2M formula.[52] The analyzed area of gold surface is $1 - \Theta$ since $CaCO_3$ crystallites are thick enough to screen Au 4d photoelectrons emitted beneath $CaCO_3$ particles and not to be detected by the XPS analyzer.

$$I_{Ca2s} = \int_0^l dI \ = A_{CaCO_3}\, n_{CaCO_3}\, \sigma_{Ca2s}\, C \int_0^l exp\left(-\frac{z}{\lambda\, cos\theta}\right) dz$$

$$= \Theta\, \frac{\rho_{CaCO_3}}{M_{CaCO_3}}\, \sigma_{Ca2s}\, \lambda_{Ca2s}^{CaCO_3}\, C(1 - exp\left(-\frac{l}{\lambda_{Ca2s}^{CaCO_3}}\right)) \qquad \textbf{(eq. 4)}$$

$$I_{Au4d} = \int_{d_{MUA}}^{\infty} dI \ = A_{Au}\, n_{Au}\, \sigma_{Au}\, C \int_{d_{MUA}}^{\infty} exp\left(-\frac{z}{\lambda\, cos\theta}\right) dz$$

$$= (1 - \Theta)\, \frac{\rho_{Au}}{M_{Au}}\, \sigma_{Au4d}\, \lambda_{Au4d}^{Au}\, C\, exp\left(-\frac{d_{MUA}}{\lambda_{Au4d}^{MUA}}\right) \qquad \textbf{(eq. 5)}$$

$$\frac{I_{Ca2s}}{I_{Au4d}} = \frac{\Theta \frac{\rho_{CaCO_3}}{M_{CaCO_3}}\, \sigma_{Ca2s}\, \lambda_{Ca2s}^{CaCO_3}}{(1-\Theta) \frac{\rho_{Au}}{M_{Au}}\, \sigma_{Au4d}\, \lambda_{Au4d}^{Au}\, exp\left(-\frac{d_{MUA}}{\lambda_{Au4d}^{MUA}}\right)} \qquad \textbf{(eq. 6)}$$

According to the model B (**Figure 5.3**) on the other hand, the I_{Ca2s}/I_{Au4d} can be calculated with consideration of protein layer, whose thickness value can be calculated from I_{N1s} signal as follows (**eq. 7-10)**.

$$I_{Ca2s} = \int_0^l dI \ = A_{CaCO_3}\, n_{CaCO_3}\, \sigma_{Ca2s}\, C \int_0^l exp\left(-\frac{z}{\lambda\, cos\theta}\right) dz$$

$$= \Theta\, \frac{\rho_{CaCO_3}}{M_{CaCO_3}}\, \sigma_{Ca2s}\, \lambda_{Ca2s}^{CaCO_3}\, C(1 - exp\left(-\frac{l}{\lambda_{Ca2s}^{CaCO_3}}\right)) \qquad \textbf{(eq. 7)}$$

$$I_{N1s} = \int_0^{d_{mr}} dI \ = A_{mr}\, n_{mr}\, \sigma_{N1s}\, C \int_0^{d_{mr}} exp\left(-\frac{z}{\lambda\, cos\theta}\right) dz$$

$$= (1 - \Theta)\, \frac{\rho_{mr}}{M_{mr}}\, \sigma_{Ca2s}\, \lambda_{N1s}^{mr}\, C\, (1 - exp\left(-\frac{d_{mr}}{\lambda_{N1s}^{mr}}\right)) \qquad \textbf{(eq. 8)}$$

$$I_{Au4d} = \int_{d_{MUA}+dmr}^{\infty} dI \ = A_{Au}\, n_{Au}\, \sigma_{Au4d}\, C \int exp\left(-\frac{z}{\lambda\, cos\theta}\right) dz$$

$$= (1 - \Theta)\, \frac{\rho_{Au}}{M_{Au}}\, \sigma_{Au4d}\, \lambda_{Au4d}^{Au}\, C\, exp\left(-\frac{d_{MUA}}{\lambda_{Au4d}^{MUA}}\right) \qquad \textbf{(eq. 9)}$$

$$\frac{I_{Ca2s}}{I_{Au4d}} = \frac{\Theta \frac{\rho_{CaCO_3}}{M_{CaCO_3}} \sigma_{Ca2s} \lambda_{Ca2s}^{CaCO_3}}{(1-\Theta) \frac{\rho_{Au}}{M_{Au}} \sigma_{Au4d} \lambda_{Au4d}^{Au} \, exp\left(-\frac{d_{MUA}}{\lambda_{Au4d}^{MUA}}\right) exp\left(-\frac{d_{mr}}{\lambda_{Au4d}^{mr}}\right)} \qquad \textbf{(eq. 10)}$$

5.3 Results and Discussion

5.3.1 Surface Functionalization with SAM

The surface characteristic of Au/MUA was assessed by PM-IRRAS before and after the functionalization. QCM-D quartz surfaces were prepared in the same thiol solution together with Au slides, and their surface property could be followed up by referencing the Au slides.

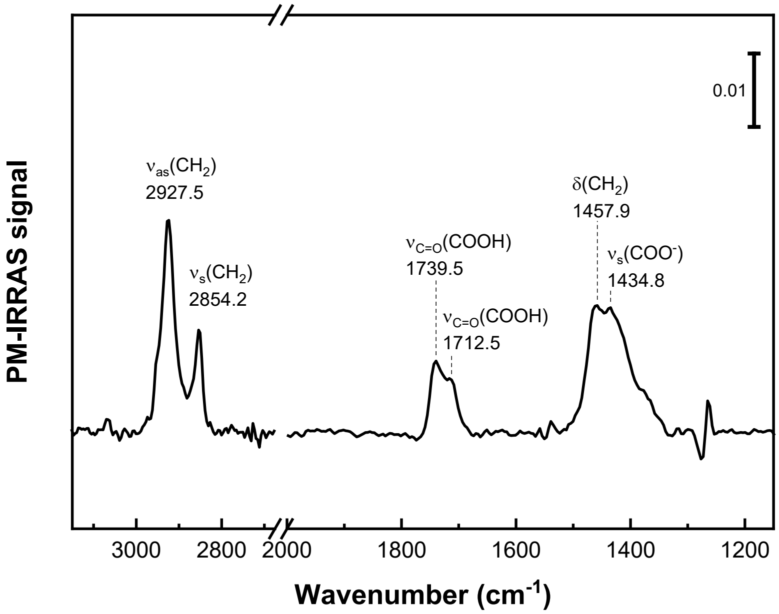

Figure 5.4 PM-IRRAS measurements after MUA adsorption on gold substrate.

Bands at 2927.5 cm^{-1} and 2854.2 cm^{-1} of **Figure 5.4** are attributed to the asymmetric and symmetric stretches of CH_2 in the alkyl chain, respectively. Bands at 1739.5 cm^{-1} and 1712.5 cm^{-1} are attributed to free and H-bonded C=O stretch of COOH, respectively. Band at 1457.9 cm^{-1} arises from the scissoring mode of CH_2 in the alkyl chain. Band at 1434.8 cm^{-1} indicates the symmetric stretching of COO^-. It indicates that carboxylic groups coexist in the protonated form and carboxylated forms. Since pKa value of MUA/Au surface is 6.2,[53] the surface was more oxidized upon the crystallization reaction during which the pH increased due to NH_3.

5.3.2 Crystallization with Proteins

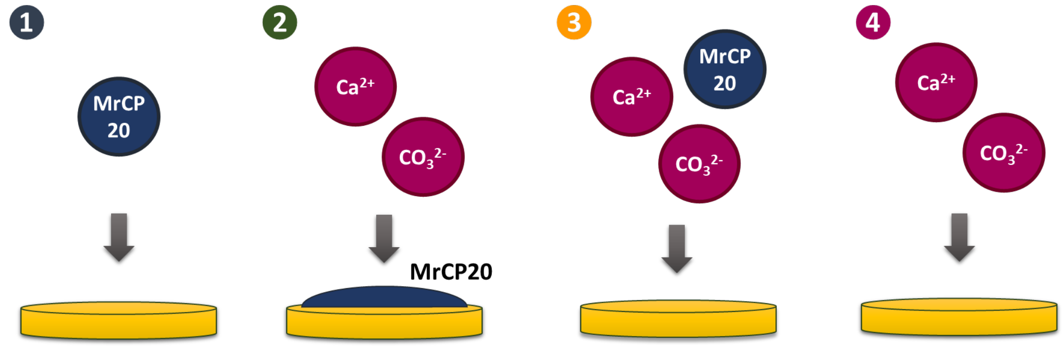

Figure 5.5 Different MUA/Au surface preparations with protein and calcium carbonate. **1** MrCP20 adsorbed on MUA/Au surface and dried (protein control). **2** Calcium ions solution and carbonate ions from CO_2 introduced to the MUA/Au surface which has adsorbed layer of MrCP20 (MrCP20/MUA/Au), $CaCO_3$ crystal formation occurs on top of the adsorbed protein layer. **3** Calcium ions solution with the presence of protein is introduced on MUA/Au with CO_2 supply. **4** Calcium ions solution without the protein is introduced on MUA/Au with CO_2 supply ($CaCO_3$ control).

To observe crystal growth with the effect of the proteins, I prepared four different surfaces (**Figure 5.5**) including: **1** control protein adsorbed surface; **2** crystal grown on top of adsorbed protein layer on surface; **3** crystal grown with the existence of protein in solution; and **4** control calcium carbonate grown surface.

5.3.3 Crystal Morphology

5.3.3.1 Optical Microscopy

Optical microscope images were taken after crystal growth (**Figure 5.6**). $CaCO_3$ grown without MrCP20 protein showed stable rhombohedral-shaped crystal structures (**Figure 5.6A**). $CaCO_3$ grown with MrCP20 protein (**Figure 5.6B**) showed mixture of rhombohedral- and spherical- shaped crystals, whose crystal morphology will be confirmed further with Raman spectroscopy in **5.3.3.2**. The crystals were not homogeneously spread, forming several clusters. Proteins were not observable by optical microscopy, but they may have attracted the ions by electrostatic interaction, interfering the mineralization process, and consequently affecting the distribution of the crystals. Interestingly, after 4 days, the crystals showed damaged, shattered, or even decomposed structures from the outer surface of the crystal (**Figure 5.6C-D**).

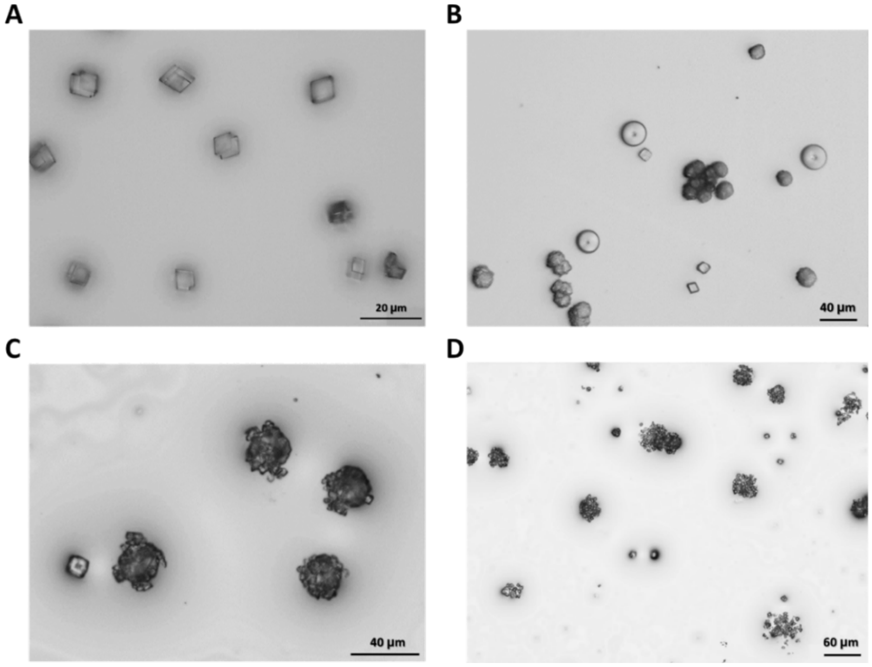

Figure 5.6 Optical microscopy images of CaCO3 crystals grown (**A**) without MrCP20 (control) and (**B-D**) with MrCP20. (**A**) The control crystals showed exclusively rhombohedral structure, from 2 hours after the start of growth reaction. (**B**) Crystals grown

in the presence of MrCP20 showed the existence of round structure 2 hours after the reaction. (**C-D**) The crystals also contained damaged, shattered, or decomposed structures after 4 days.

5.3.3.2 Raman Spectroscopy

Calcium carbonate crystallization includes nucleation, growth, and the phase transition from amorphous through metastable vaterite (hexagonal) to the most stable calcite (trigonal). Nucleation mainly takes place in the early stage after an induction time, followed by growth process. During this mineralization, they undergo phase transformation from one morphology to another, towards the most stable phase. Amorphous $CaCO_3$ (ACC) is the thermodynamically least stable phases, followed by metastable vaterite and aragonite phases, and the thermodynamically most stable phase, calcite. Multistep transformation of the morphology derives from successive dissolution and recrystallization processes in the aqueous system[54,55].

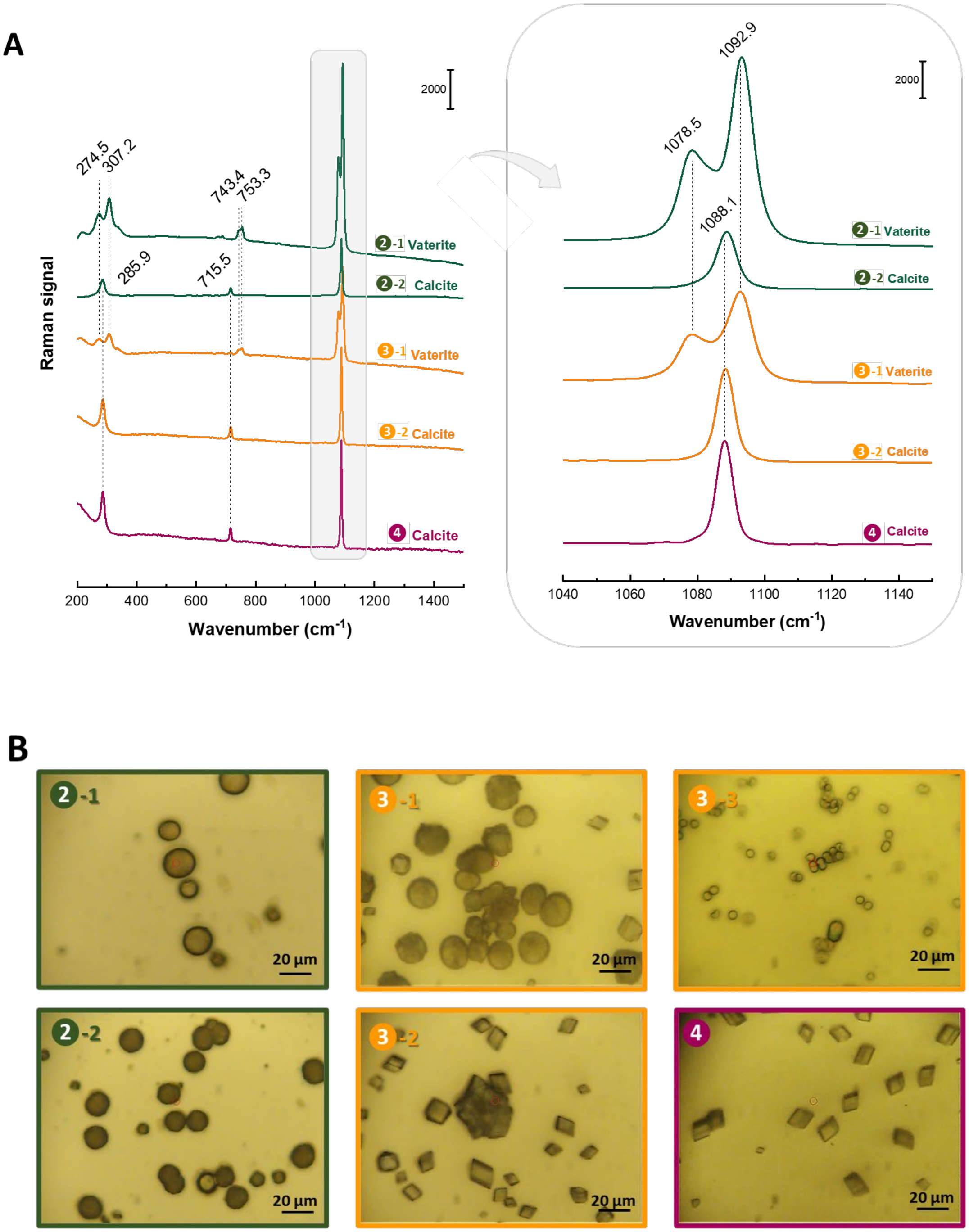

Figure 5.7 Characterization of CaCO3 microcrystals. **(A)** Raman spectra of crystals grown in the presence of MrCP20 either on surface (2) or in solution (3) showed both vaterite and calcite morphologies, while it had only calcite in the absence of MrCP20 (4). **(B)** Optical microscopy images (the microscope connected to the Raman equipment) showed rhombohedral shape crystals exclusively in the absence of MrCP20 (4), and both

rhombohedral and spherical shape crystals in the presence of MrCP20 on surface (**2**) or in solution (**3**).

The effect of the protein on the crystal morphology was studied using Raman spectroscopy (**Figure 5.7**). $CaCO_3$ crystals formed in the absence of MrCP20 (**4**) in rhombohedral shape were exclusively calcite, according to the Raman spectra showing the bands at 285.9 cm^{-1}, 715.5 cm^{-1}, and 1088.1 cm^{-1}.[56–64] $CaCO_3$ crystals formed in the presence of 2 µg of MrCP20 showed both (**3-1**) spherical- and (**3-2**) rhombohedral- shape crystals and the corresponding Raman signal was attributed to vaterite and calcite phases, where vaterite exhibits bands at 274.5 cm^{-1}, 307.2 cm^{-1}, 743.4 cm^{-1}, 753.3 cm^{-1}, 1078.5 cm^{-1}, 1092.9 cm^{-1}.[56–64] $CaCO_3$ crystals formed in the presence of 20 µg of MrCP20 showed smaller and more spherical shaped crystals (**3-3**) at the same incubation time, dominated by vaterite Raman bands. These results indicate that high quantity of protein in solution had the strongest effect regarding stabilization of vaterite. The crystal morphology was also studied when the calcium carbonate was grown on surfaces initially adsorbed with 20 µg of MrCP20 (**2**). The crystal shape was mostly spherical based on the microscope connected to the Raman equipment, but the Raman spectra indicated that both vaterite and calcite were present. The protein layer on top of the MUA surface hindered controlled growth of (113) nucleating calcite, but it did not completely inhibit phase transition towards thermodynamically the most stable calcite morphology. All the Raman spectra represented were taken after one day when the crystal growth was stabilized. Although the vaterite morphology did not last for more than a week, the data strongly suggested that MrCP20 has a significant influence on the Ostwald's steps[65], representing successive phase transformation and recrystallization of $CaCO_3$ polymorphs. The theoretical scheme (**Figure 5.8**) is suggested for the potential effect of MrCP20 on Ostwald's steps.

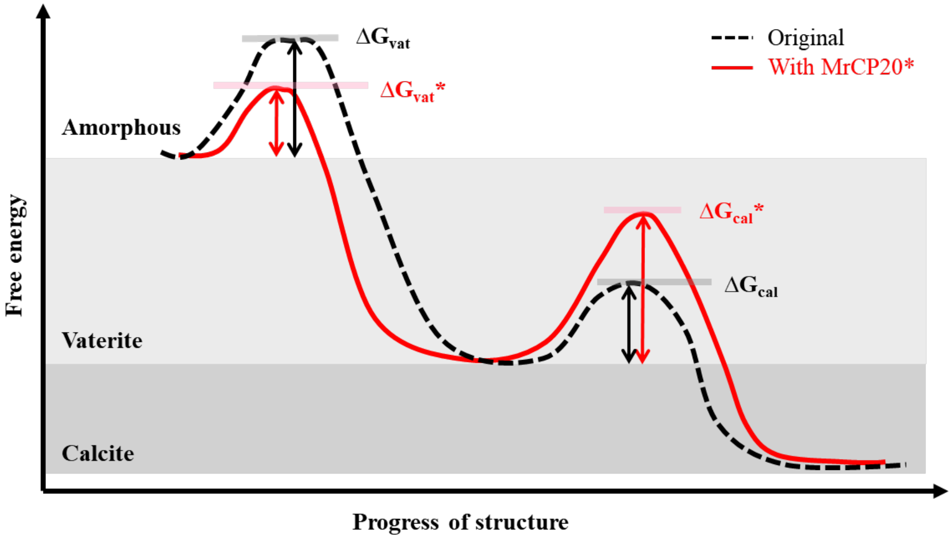

Figure 5.8 Multi-step CaCO3 crystallization pathways from amorphous precursors through vaterite towards the most stable calcite, with schematic indication of free energy change and activation energy barrier for each step. MrCP20 may decrease the activation energy required for phase transformation into vaterite ($\Delta G_{vat} > \Delta G_{vat}$*), while increasing what is required to reach calcite phase ($\Delta G_{cal} < \Delta G_{cal}$*).

$CaCO_3$ crystallization often proceeds by multi-step pathways from amorphous to calcite through metastable intermediates with activation energy barriers (ΔG).[66,67] Transition process of the phases depends on the solubility of each mineral phase and activation energy of their interconversion, which is known to be strongly influenced by additives.[68] The presence of MrCP20 either in solution or on surface during the mineralization process possibly encouraged the involvement of vaterite stage by decreasing the energy barrier of the amorphous-to-vaterite transformation ($\Delta G_{vat} > \Delta G_{vat}$*) or increasing the energy barrier of the vaterite-to-calcite transformation ($\Delta G_{cal} < \Delta G_{cal}$*), or both of them. The phase of aragonite was not represented in the figure since the pathway did not take place under our temperature condition.[69–71] The potential function of MrCP20 may benefit the growing process of mineral periphery shell at the bottom edge and the base plate by maintaining the vaterite morphology for prolonged period before transforming into calcite.

5.3.4 In-situ Crystal Growth Kinetics Observed with QCM-D

5.3.4.1 Vapor diffusion

Real time information of crystallization on -COOH modified surface was obtained by QCM-D. The resonant frequency was stabilized in air for 5 min followed by stabilization in $CaCl_2$ solution for 20 min. Upon supply of CO_2, the resonant frequency decreased significantly as crystal formation took place and being adsorbed on the quartz.

5.3.4.2 Quantification Model

Voinova et al. (1999)[72] developed the Kelvin-Voigt viscoelastic model, describing the resonant frequency (Δf) and dissipation changes (ΔD) of sensors for Newtonian fluids as a viscoelastic film formed on the surface. It is usually applicable to homogeneous and isotropic layer, or anisotropic layers which can be averaged over the bulk. Δf and ΔD are calculated as functions of fluid density, fluid viscosity, film viscosity, film density, film elasticity (shear modulus), and film thickness/mass. I input the model parameters of the density of calcite as 2710 kg/m^3, the fluid density as 1.1098 kg/m^3, and fluid viscosity as 0.001 kg/m·s, respectively. The other parameters were given within certain ranges: film viscosity (0.0005 – 0.01 kg/m·s), film elasticity (10^4 – 10^9 Pa) and film mass (10 – 10^6 ng/cm^2). By obtaining the best fits of the QCM-D measured frequency (Δf) and dissipation (ΔD) changes at different harmonics ($n = 3, 5$), film viscosity, film elasticity and film mass on sensors were calculated. The calculated mass was 86.5 µg/cm^2, which was comparable to the value calculated using Sauerbrey equation from the third harmonic ($n = 3$), which was 92.4 µg/cm^2. The more harmonics we have for fitting curves with the Kelvin-Voigt model, the more accurate mass values we can estimate. Unfortunately, as the load on the sensor increased drastically upon crystal growth, the oscillation of the sensors was beyond the capability of the equipment, and the system lost signals from the highest harmonics to either

7th or 5th. Hereby, surface mass from all the QCM-D measurements in this chapter were calculated using the 3rd harmonic and the Sauerbrey equation.

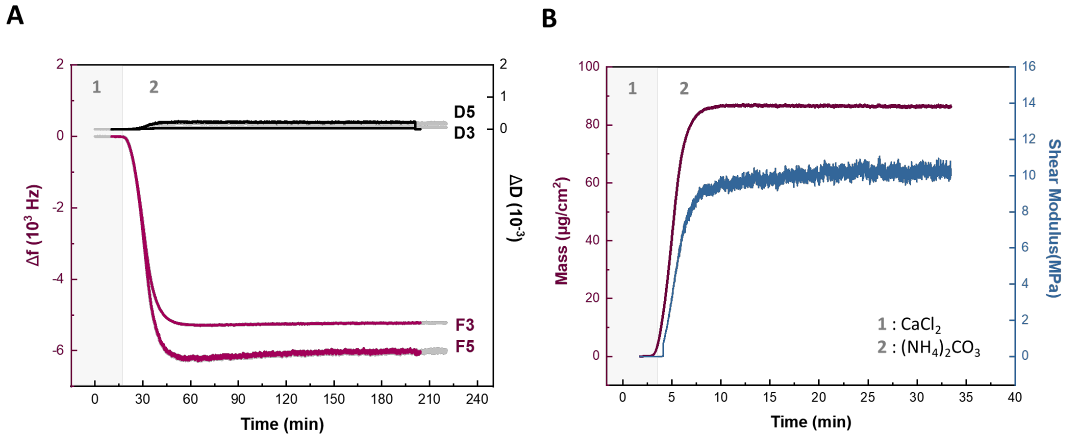

Figure 5.9 A representative QCM-D curve processed for the Kelvin-Voigt model fitting. **(A)** 3rd and 5th harmonics (grey) were taken for the fitting, and the resulting fitted curves are presented in vivid lines (frequency in red, dissipation in black). **(B)** Calculated mass (red) and shear modulus (blue) by the model fitting shows that the $CaCO_3$ mass on the surface reaches 86.5 (µg/cm^2) upon saturation.

5.3.4.3 Crystal Growth Inhibition with Increasing Amount of MrCP20

The influence of MrCP20 on crystal growth kinetics was analyzed as a function of the protein concentration. As the amount of MrCP20 in $CaCl_2$ solution increased, the frequency drop upon crystal growth decreased accordingly, as shown in **Figure 5.10**. One could observe not only the final saturated frequency value, but also a gradient of frequency by the time CO_2 was introduced, likely affected by the increasing amount of MrCP20. This data indicated that the protein regulated crystal growth from the beginning of the nucleation process.

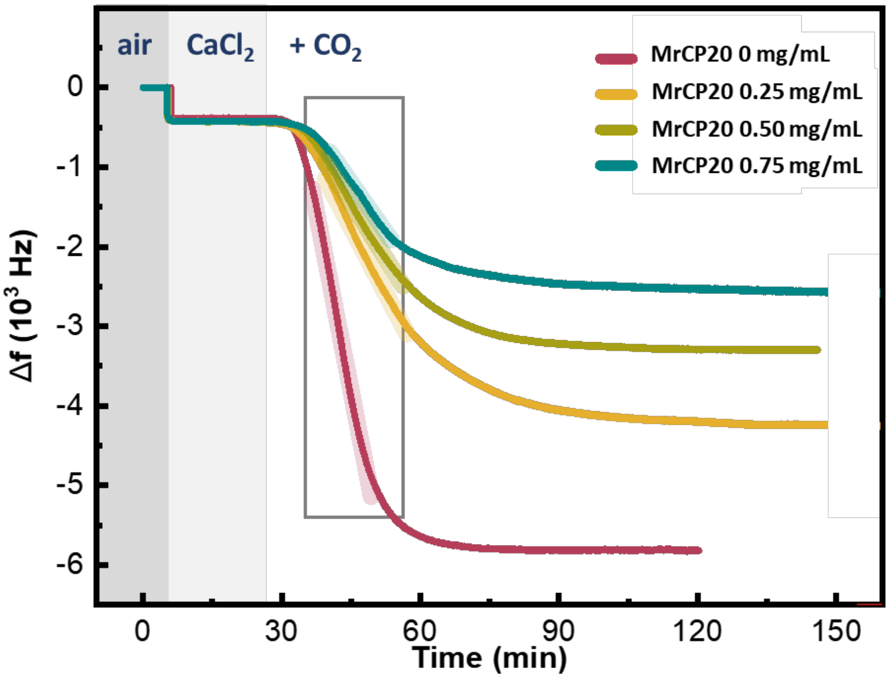

Figure 5.10 The frequency and dissipation shift of the QCM-D associated with crystallization of $CaCO_3$ on -COOH modified Au surface. After the surfaces were stabilized in air, 10 mM $CaCl_2$ with 0.25 mg/mL, 0.50 mg/mL, or 0.75 mg/mL of MrCP20 or without MrCP20 was dropped on the QCM quartz at 5 min and an excessive amount of $(NH_4)_2CO_3$ was introduced to the solution to provide CO_2 after 20 min.

Table 5.2 Linearly fitted slope of the highlighted section of each frequency curve from **Figure 5.10**.

MrCP20 (mg/mL)	Δf/t Slope (10^3 Hz/min)
0	-5.0
0.25	-1.8
0.50	-1.5
0.75	-1.4

The crystal mass upon the growth saturation was calculated using the Sauerbrey equation, and is represented in **Figure 5.11**. The effect of impurities on crystallization process has been extensively studied and most of the growth mechanisms are based on the concept of adsorption of impurities on a growing surface[73–75]. $CaCO_3$ crystal growth kinetics in the presence of additives has been interpreted in terms of a Langmuir-type isotherm in many studies to explain the growth inhibition effect[76–78]. In the present study, the inhibited mass relative to the fully grown crystal mass (control without any MrCP20) was linearly fitted to the inverse of the protein concentration with an *R* square value of 93.1% (**Figure 5.11B**). The discrepancy occurred from the effect of direct chelation of the proteins with the crystal ions in the solution which influenced the multistep crystallization process.

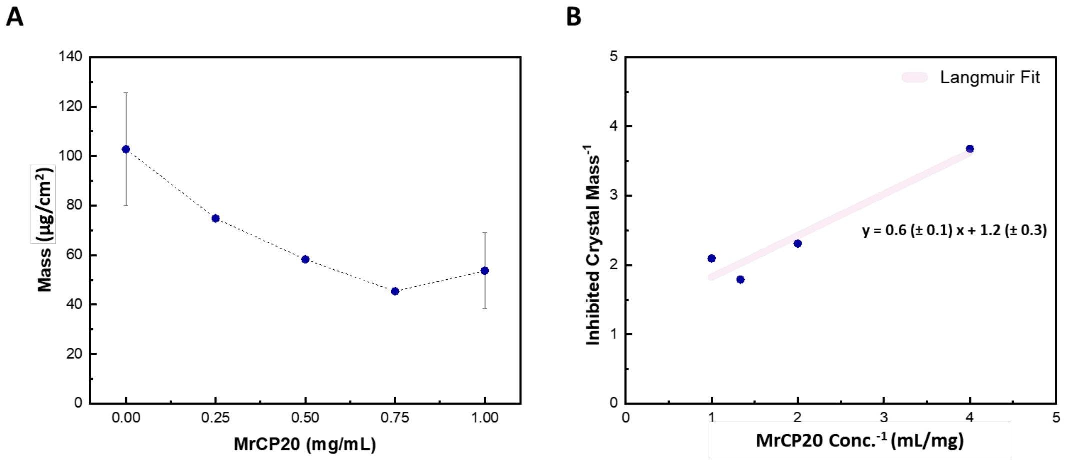

Figure 5.11 CaCO3 growth affected by the presence of MrCP20 in $CaCl_2$ solution. (**A**) Plot of the crystal mass as a function of MrCP20 concentration in solution, and (**B**) linearly fitted Langmuir isotherm plot.

5.3.4.4 Crystal Growth influenced by MrCP20

In order to study the effect of proteins in solution or on surface upon crystal growth, the *in-situ* crystallization process taking place on surfaces **2**-**4** was carried out on a QCM-D chip and the frequency change and dissipation were concomitantly monitored as shown in **Figure 5.12**. $CaCl_2$ in the absence of MrCP20 (**4**), showed an immediate frequency shift, dropping at -1628 Hz after 10 min, while $CaCl_2$ containing 1 mg/mL of MrCP20 (**3**) took four times longer to achieve the same frequency shift. Crystal growth rate on the surface **3** was also very slow compared to surface **4**. During the linear growth phase, the $\Delta f/t$ slope was -1.19 (Hz/sec) on the surface **3** and -3.13 (Hz/sec) on the surface **4**, respectively. In short, MrCP20 in solution led to a longer induction time and slower nucleation and growth kinetics of crystallization.

In agreement with previous studies on acidic amino acids retarding the crystallization kinetics of $CaCO_3$ [79–82], the large number of negative residues in MrCP20 can result in significant interference on the crystal growth. Strong interactions between the negative surface charge of MrCP20 and Ca^{2+} ions in solution forms an additional layer of the counterions, and this double layer (DLVO)[83,84] around the protein decreases the ability of both ions to reach the MUA surface. This mechanism occurs from the beginning of crystallization since the nucleation is predominantly dependent on the number density of nuclei, a mechanism referred as the classic nucleation theory (CNT)[85]. The ions partially captured by MrCP20 in solution deplete ions on the MUA surface, which increases the induction time and consequently inhibits the total nucleation and growth process of $CaCO_3$. This is also supported by MD simulation on MrCP20 and surrounding ions[27], which showed ion clusters formed around the protein interacting with the charged sites of the protein via electrostatic and water-mediated interactions. Additionally, reduced free cysteine residues have been suggested to participate in mineral growth as much as Asp[86] and MrCP20 possesses 6 disulfide bonds (12 Cys) and 20 free Cys in its natural state. Finally, steric hindrance from the protein can interfere electrostatic interactions between the Ca^{2+} and CO_3^{2-} ions in a broader range, resulting in inhibition of lattice construction.

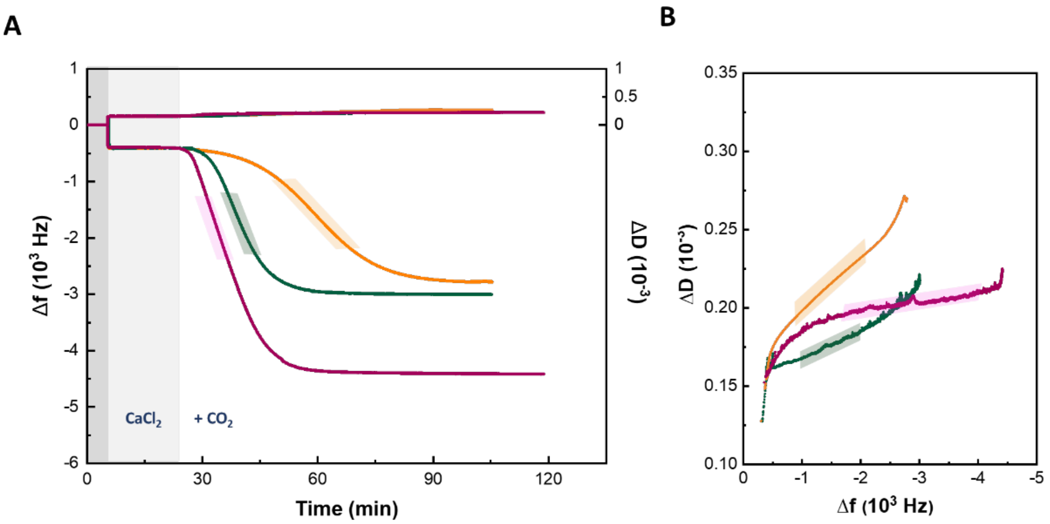

Figure 5.12 (A) Frequency and dissipation shift measured by QCM-D over time due to the crystallization of $CaCO_3$ on -COOH modified Au surface. After the surfaces were stabilized in air, 10 mM $CaCl_2$ with (**3**) or without (**2**,**4**) 1 mg/mL MrCP20 was dropped on the QCM quartz surfaces at 5 min and excessive amount of $(NH_4)_2CO_3$ was introduced aside the solution to provide CO_2 after 20 min. Highlighted section of each curve was linearly fitted to compare growth rate of the crystals regarding presence of MrCP20. **(B)** Corresponding $\Delta D/\Delta f$ plot, and highlighted section of each curve was linearly fitted to compare viscoelastic property of adsorbed layer regarding presence of MrCP20.

With the presence of MrCP20 on the surface, surface **2** showed a slightly longer induction time (5 min) and slightly slower growth rate than the control (surface **4**), with the $\Delta f/t$ slope of -2.76 (Hz/sec). Similar nucleation and growth rate indicated that there was no interference from the protein in the liquid environment, but a minor interference from the protein on surface. On the other hand, much less crystals were grown compared to surface **4**, and this was due to the protein layer partially covering MUA surface that changed the overall surface property. Due to the protein layer, Ca^{2+} ions were not homogeneously distributed on the surface, but rather locally concentrated on top of MUA/Au or MrCP20/MUA/Au. When CO_2 was introduced, CO_3^{2-} ions reaching the Ca^{2+} ions near the MUA surface were highly interrupted as they were partially attracted to the positive surface residues of MrCP20 (if any of them were exposed to the solution) as well as the Ca^{2+} layer formed around MrCP20. This also explains the lower number of nucleation sites and their more heterogeneous distribution than on surface **4**. The final mass of grown crystals was similar to that of **3**, showing that MrCP20 in solution and on surface have analogous inhibition effects on the crystal formation.

The viscoelastic behavior of the layer was best observed on dissipation plots normalized with frequency (**Figure 5.12B**). Surface **4** had the smallest gradient of $\Delta D/\Delta f$, which suggests that the crystal layer was the most rigid occurring due to the closest interaction between $CaCO_3$ and the surface. The slope of surface **2** was superior to surface **4** by a factor 2, indicating that the protein layer on the surface affected the rigidity by mediating the interaction between the crystals and the surface, and by forming more various crystal sizes. Surface **3** had the highest measured slope, suggesting that the protein in solution increased the shear modulus of the crystal layer the most among the three surfaces, with the highest variety in size. Altering ion clusters surrounding proteins in solution could curtail close ion interaction near the surface.

Table 5.4 Mass per surface area, $\Delta f/t$ slope, and $\Delta D/\Delta f$ slope obtained from multiple QCM-D experiments of surface **2**-**4**.

	Mass ($\mu g/cm^2$)						Mean	SD
2	72.3		69	50.7	68.85	45.72	61.314	12.170
3	76.3	57.1	74.3	65.5	80.53	41.86	67.698	15.449
4	128.64	92.4	-	111	96.08	71	105.39	22.702

	Δf/t slope (Hz/s)						Mean	SD
2	-4.26	-	-1.86	-1.62	-3.35	-2.69	-2.76	1.085
3	-0.87	-1.98	-1.60	-0.87	-2.25	-1.19	-1.36	0.583
4	-2.53	-5.48	-	-4.90	-5.18	-3.13	-4.03	1.151

	ΔD/Δf Slope ($10^{-6}/Hz^{-1}$)						Mean	SD
2	-0.02	-	-0.02	---	-0.03	-0.02	-0.023	0.005
3	-0.03	-0.02	-0.02	-0.02	-0.02	-0.03	-0.024	0.005
4	-0.03	-0.01	-	-0.02	-0.01	-0.01	-0.016	0.015

Six sets of experiments were done for reproducibility and the average values were summarized in the **Figure 5.13** and **Table 5.3-4**. In short, the QCM-D Δ*f/t* kinetic curves and Δ*D*/Δ*f* plots indicate that MrCP20 played a crucial role in regulating crystallization from nucleation to growth. In relative terms, the ratio of surface mass on surface was **2**:**3**:**4** = 1:1.1:1.7, and the ratio of Δ*D*/Δ*f* gradient was **2**:**3**:**4** = 1.5:1.5:1.

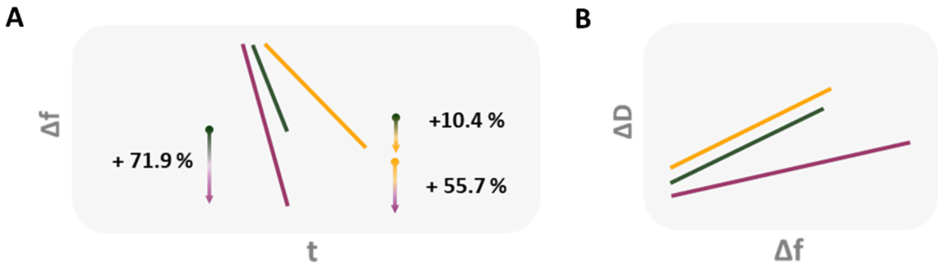

Figure 5.13 Summary scheme of average values of (**A**) Δ*f/t* slope, and (**B**) Δ*D*/Δ*f* slope obtained from multiple QCM-D experiments of surface **2**-**4**.

Table 5.3 Average values of mass per surface area, Δ*f/t* slope, and Δ*D*/Δ*f* slope obtained from multiple QCM-D experiments of surface **2**-**4**.

	Mass (μg/cm^2)	Δf/t slope	ΔD/Δf Slope
2	61.3 ± 12.2	-2.8 ± 1.1	-0.023 ± 0.005
3	67.7 ±15.4	-1.4 ± 0.6	-0.024 ± 0.005
4	105.4 ± 22.7	-4.0 ± 1.1	-0.016 ± 0.015

The unique behavior of MrCP20 was supported by another set of experiments done in the comparison of the protein with β-lactoglobulin. "β lg" in **Figure 5.14** indicates crystallization conducted in the presence of commercial β-lactoglobulin in $CaCl_2$ solution, prepared in the same method as surface **3**. No inhibition of the crystal growth was observed from **Figure 5.14A**, but the dissipation shift was similar with that of surface **3**. It proved that the similar molecular weight protein (18.4 kDa) could affect the dissipation of the adsorbed layer upon crystallization, but not the kinetics of the crystal growth.

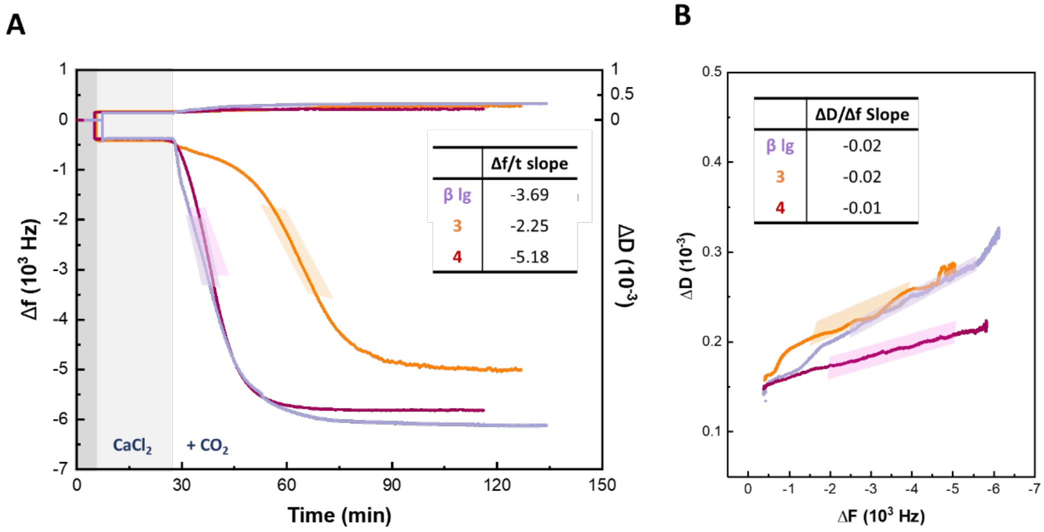

Figure 5.14 (A) Frequency and dissipation shift measured by QCM-D over time due to the crystallization of $CaCO_3$ on -COOH modified Au surface. Highlighted section of each curve was linearly fitted and represented in the inserted table to compare the growth rate of the crystals. **(B)** Corresponding $\Delta D/\Delta f$ plot, and highlighted section of each curve was linearly fitted and represented in the inserted table to compare viscoelastic properties of adsorbed layer.

5.3.5 Quantification of Crystal using XPS

After QCM-D measurements, the quartz surfaces were prepared for XPS analysis to quantitatively analyze the grown crystals. The crystals formed on the surface were first probed by optical microscopy measured from different scanning areas, averaged, and converted to the length of cube for calculations. In the absence of MrCP20, smooth calcite crystals of (113) nucleating plane[40] with a rhombohedral shape were observed with an average width of 7.7 ± 3.3 µm. In contrast to surface **4**, which showed homogeneously spread crystals, surfaces **2** and **3** had more random distributions in space, shape, and size of crystals. The mean width of the crystal was measured and averaged to be 6.6 ± 4.4 µm for surface **3** and 4.8 ± 3.2 for surface **2**. MrCP20 on surface and in solution interrupted nucleation on the surface, resulting in higher variability in size of the crystals, grown from fewer nuclei. Additionally, the protein diminished the surface's orienting effect for crystal growth at (113) direction, which was observable from the rhombohedral shape of the crystals[40].

According to Beer-Lambert law, the surface mass of the crystal was obtained from **eq.6**. The photoelectron intensity values were taken from the area of Ca 2s and Au $4d_{5/2}$ peaks as illustrated in **Figure 5.15-16**. Surface **2** had 6% less, and surface **4** had 62% more, respectively, of $CaCO_3$ grown on the surface compared to surface **3**.

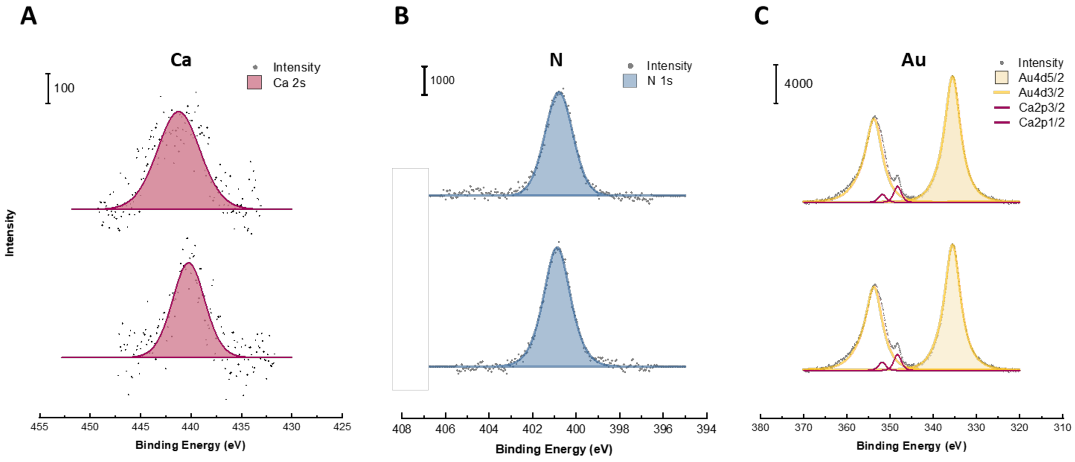

Figure 5.15 XPS spectrum for (**A**) Ca 2s, (**B**) N 1s, and (**C**) Au 4d peaks from surface **2** (top) and surface **3** (bottom).

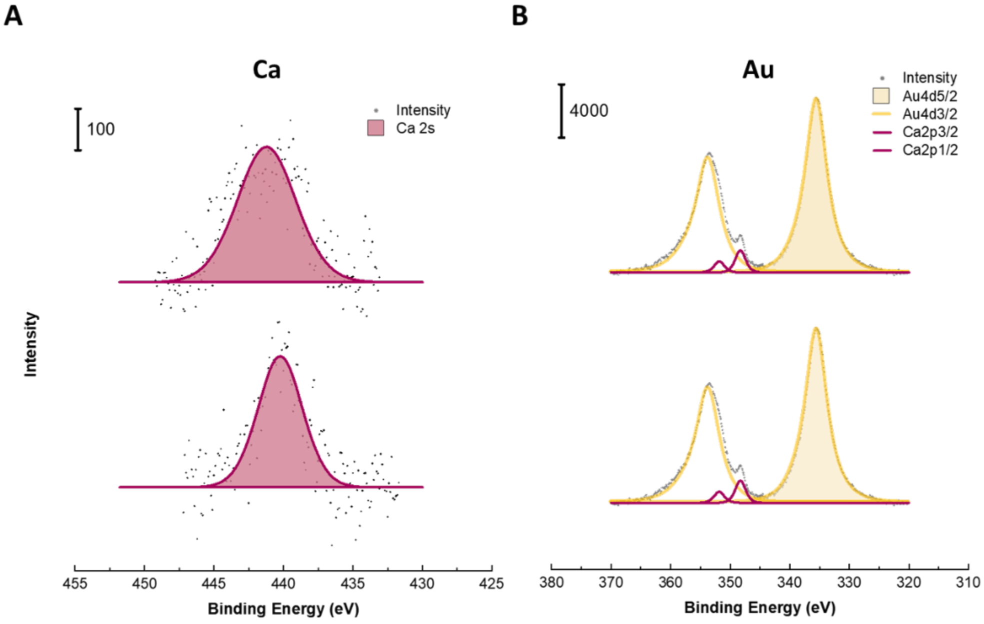

Figure 5.16 XPS spectrum for (**A**) Ca 2s and (**B**) Au 4d peaks from surface **3** (top) and surface **4** (bottom).

On the other hand, for surface **2**, the protein layer on top of MUA/Au can be taken into account for the calculation (**eq. 10**). E**q. 10** assumes a homogeneous layer of proteins that can induce uniform electron attenuation throughout the surface. The average protein layer thickness value of our experiment was obtained from the intensity ratio of N 1s to Au 4d **(Figure 5.15B, eq. 8)**. The parameters used for **eq. 8** are; density of protein in solid state 1.35g/cm^3, molecular weight of MrCP20 21428.95, and number of N in MrCP20 275. Therefore, $\boldsymbol{d_{mr}}$ was calculated to be 1.7 nm, and this value was in the range of radius of gyration (1.2 ~ 2.2 nm).[27,87] With consideration of the protein layer on surface **2**, surface **3** achieved 13% higher adsorbed mass compared to surface **2**.

The resulting surface mass of $CaCO_3$ investigated using XPS was compared with the relative Sauerbrey mass obtained by QCM-D experiments as shown in **Table 5.5**. The results were in close agreement with each other.

Table 5.3 Surface mass (µg/cm^2) obtained from XPS compared to the Sauerbrey mass obtained from QCM-D. For Surface **2**, surface layer modeling with[b] or without[a] considering the protein layer were used, resulting in surface **3** to have a relative mass range of 7-13%.

Surface mass (µg/cm^2)	**XPS**		**QCM-D**
2	179.05[a]	169.79[b]	61.31 ± 12.17
3	191.44		67.70 ±15.45
Relative mass **3**/**2** (%)	+ 7[a]	+ 13[b]	+ 10
3	78.73		67.70 ±15.45
4	127.87		105.39 ± 22.70
Relative mass **4**/**3** (%)	+ 62		+ 56

5.3.6 Protein Morphology in the Presence of CaCO$_3$

Calcium carbonate grown on SAM-modified Au surfaces (**4**) were characterized using PM-IRRAS (**Figure 5.17**). A sharp band at 1415 cm^{-1} was detected corresponding to the anti-symmetric stretching (v_3) in the *ab* plane of the carbonate group[88]. This band was also visible when it was grown on MrCP20/MUA/Au (**2**), and when it was grown in the presence of MrCP20 in solution (**3**).

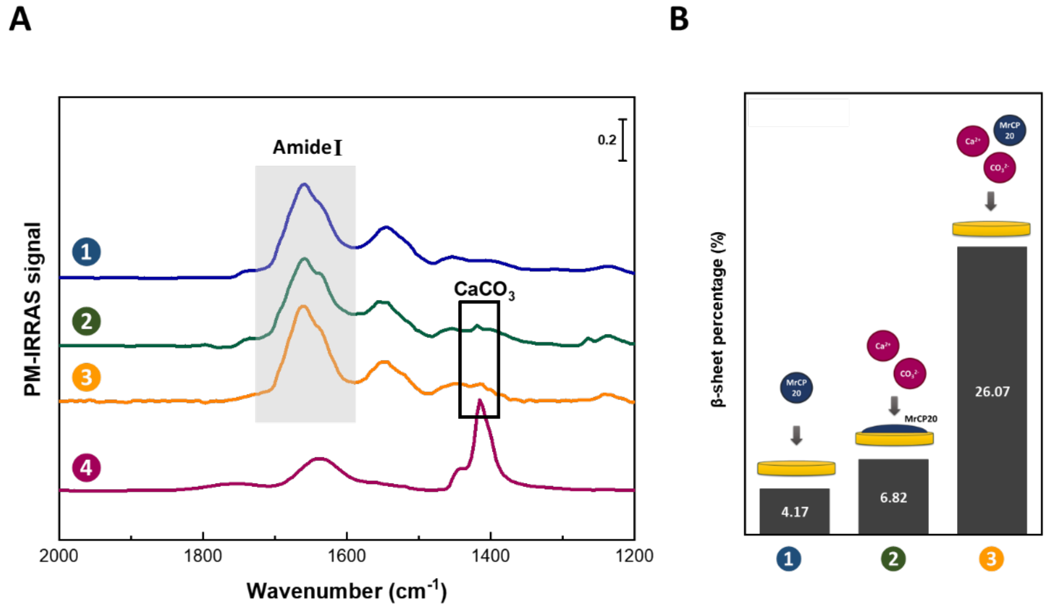

Figure 5.17 (A) PM-IRRAS measurement after protein adsorption showing the presence of the Amide I band at 1600-1700 cm^{-1} or $CaCO_3$ at 1415 cm^{-1} on MUA/Au. **(B)** Histogram showing relative parallel (dark) and antiparallel (bright) β-sheet contents of the adsorbed MrCP20 in different condition by PM-IRRAS.

The protein film adsorbed on the surfaces was assessed by the presence and the configuration of Amide I and Amide II bands. The Amide I mode represents 80 % of C=O stretching vibration of the amide group coupled to 10% of in-plane N-H bending and 10% of C-N stretching modes. The exact contributions of each vibration depend on hydrogen bonding of C=O and N-H groups, which are determined by the secondary structures of the protein[89,90]. The composition of each secondary structure, namely α-helix, β-sheet, β-turn, and random coil, was calculated by deconvolution of the amide I band, following the guidelines[91]. The deconvolution of protein bands when there was $CaCO_3$ on the surface was done after normalizing with $CaCO_3$ signal. The curves were fitted and converged with a range of $R^2 = 0.97$ and $\chi^2 = 10^{-6}$. The deconvolution process and the results of the components are shown in **Figure 5.18** and **Table 5.6**.

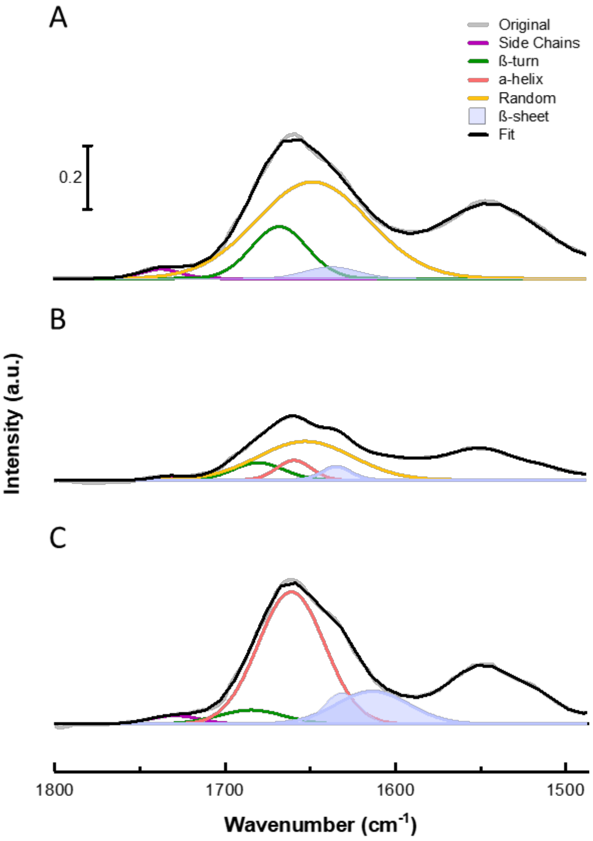

Figure 5.18 Deconvolution of the PM-IRRAS in the amide I region for **(A)** **1** MrCP20, **(B)** **2** MrCP20 on surface, and **(C)** **3** MrCP20 in solution. Each PM-IRRAS signal was baseline corrected and normalized with the signal coming from the surface.

Table 5.4 Secondary structure content of amide I band from surface **1**-**3**.

Amide I components	1 **MrCP20**		2 **MrCP20 on surface**		3 **MrCP20 in solution**	
	Wavenumber (cm^{-1})	Area %	Wavenumber(cm^{-1})	Area %	Wavenumber(cm^{-1})	Area %
β turn	1667.59	20.14	1680.01	15.61	1684.95	6.96
α-helices	-	-	1659.09	12.16	1661.13	66.97
Random	1648	75.68	1652.35	65.42	-	-
parallel β-sheet	1636.80	4.17	1634.18	6.82	1631.28	8.09
					1613.49	17.98

The influence of $CaCO_3$ growth on molecular structure of MrCP20 and fibrillation could be linked to the content of parallel and anti-parallel β-sheets, which are shown as relative percentage and presented in **Figure 5.17B**. A relatively high content of β-sheet (8.09 % of parallel and 17.98 % of antiparallel) was present in MrCP20 when there was growth of $CaCO_3$, compared to the adsorbate with only protein (4.17 % of parallel). When Ca^{2+} and CO_3^{2-} ions were added and $CaCO_3$ was grown after the protein adsorption on the surface, the ions in the solution and the mineralization process might have affected the protein structure of the adsorbed film, and increased the β-sheet content (6.82 % of parallel and 15.61 % of antiparallel). Electrostatic interactions between the ions and charged aminoacid residues of MrCP20 might affect the secondary structure of the protein as well as the crystal structure of $CaCO_3$. Additionally, the pH changed upon chemical reaction of Ca^{2+} and CO_2 to form $CaCO_3$ as discussed earlier, and this could affect the secondary structure of the proteins such that it assembled into fibrillar structures reminiscent of amyloid.[12,30,34] Such fibrillar structures are known to have significant mechanical stability and resistance to enzymatic degradation, which might contribute to the cement's tenacity[30,92–95].

According to the discussions above, MrCP20 affected the nucleation and growth of $CaCO_3$ by electrostatic and water-mediated interactions. As protein influenced crystal formation, the crystal showed the mutual effect on MrCP20 to have more structured ordering in favor for β-sheet packing and fibril formation. MrCP20 is potentially a good candidate to regulate the calcareous base plate's biomineralization process, as well as to interact with substratum from other marine creature or sedimentary minerals that are often made of calcium carbonate.

5.4 Conclusion

In this Chapter, different surface sensitive techniques were used to investigate protein-mediated calcium carbonate mineralization, as well as ions-mediated reconstruction of the adsorbed protein layer.

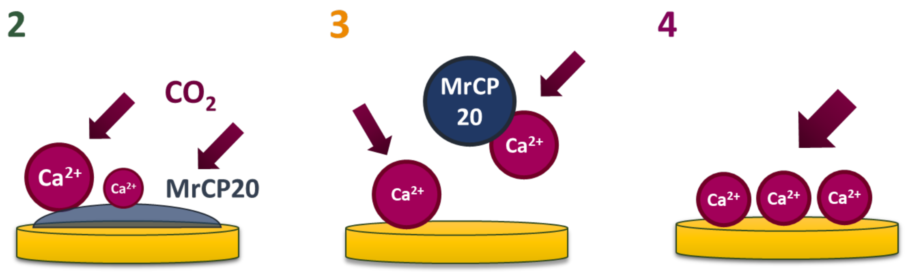

Nucleating speed	Fast	Slow	Very fast
Nucleation sites	Less	Less	A lot, well distributed
Growth speed	2	1	3
Saturated mass	1	1.1	1.7
Viscoelasticity	1.5	1.5	1

Figure 5.19 Schematic representation of the interaction between MrCP20 and $CaCO_3$ ions (top) and summary of the crystallization behavior (bottom) on surfaces **2**-**4**. The numbers indicate relative values.

The kinetics of crystallization and the resulting crystal structures were affected by the presence of MrCP20, owing to its high surface charge which enables electrostatic interactions and water mediated interactions with the surrounding ions. Protein in solution as well as the protein adsorbed on the surface interacted with the ions and stabilized the metastable vaterite polymorphism of $CaCO_3$ and reduced the amount of crystal formation. Less crystallinity, homogeneity in size, and alignment of the crystals may have been designed by MrCP20 to achieve better mechanical properties upon external stress. By delaying the process of nucleation and growth of $CaCO_3$, MrCP20 was suggested to play an important role in regulating biomineralization of the barnacle base plate and outer shell during its lifetime. The flexible conformational characteristics of MrCP20 is a key feature giving the ability of the protein adsorbed on the surface to affect calcium carbonate crystallography once ionic species in solution were introduced.

Additionally, the crystallization process affected the structural behavior of the protein on surface. Calcium carbonate growth increased the amount of both parallel and anti-parallel beta sheet of MrCP20, which stabilized its self-assembly into fibrillar nanostructures. This biomolecular structure can play multifunctional roles at the adhesive interface of barnacles by mediating adhesion and cohesion, and possibly antimicrobial effect. The combined results provided new insights of the mutual influence between MrCP20 and the barnacle base plate biomineralization at the molecular level.

References

1. Matsumura, K., Nagano, M. & Fusetani, N. Purification of a larval settlement-inducing protein complex (SIPC) of the barnacle, Balanus amphitrite. *Journal of Experimental Zoology* **281,** 12–20 (1998).
2. Aldred, N., Phang, I. Y., Conlan, S. L., Clare, A. S. & Vancso, G. J. The effects of a serine protease, Alcalase®, on the adhesives of barnacle cyprids (*Balanus amphitrite*). *Biofouling* **24,** 97–107 (2008).
3. Crisp, D. J. & Knight-Jones, E. W. The Mechanism of Aggregation in Barnacle Populations. *The Journal of Animal Ecology* **22,** 360 (1953).
4. Walker, G. A study of the cement apparatus of the cypris larva of the barnacle Balanus balanoides. *Marine Biology* **9,** 205–212 (1971).
5. Walker, G. THE EARLY DEVELOPMENT OF THE CEMENT APPARATUS IN THE BARNACLE, BALANUS BALANOlDES (L.) (CRUSTACEA: CIRRIPEDIA). 10
6. Mullineaux, L. S. & Butman, C. A. Initial contact, exploration and attachment of barnacle (Balanus amphitrite) cyprids settling in flow. *Mar. Biol.* **110,** 93–103 (1991).
7. Purification of a larval settlement-inducing protein complex (SIPC) of the barnacle, Balanus amphitrite. 9
8. Høeg, J. T., Maruzzo, D., Okano, K., Glenner, H. & Chan, B. K. K. Metamorphosis in Balanomorphan, Pedunculated, and Parasitic Barnacles: A Video-Based Analysis. *Integrative and Comparative Biology* **52,** 337–347 (2012).
9. Kamino, K. in *Biological Adhesives* (ed. Smith, A. M.) 153–176 (Springer International Publishing, 2016). doi:10.1007/978-3-319-46082-6_7
10. Maleschlijski, S., Bauer, S., Aldred, N., Clare, A. S. & Rosenhahn, A. Classification of the pre-settlement behaviour of barnacle cyprids. *Journal of The Royal Society Interface* **12,** 20141104 (2015).
11. Aldred, N., Høeg, J. T., Maruzzo, D. & Clare, A. S. Analysis of the Behaviours Mediating Barnacle Cyprid Reversible Adhesion. *PLOS ONE* **8,** e68085 (2013).

12. Barlow, D. E., Dickinson, G. H., Orihuela, B., Kulp, J. L., Rittschof, D. & Wahl, K. J. Characterization of the Adhesive Plaque of the Barnacle *Balanus amphitrite* : Amyloid-Like Nanofibrils Are a Major Component. *Langmuir* **26,** 6549–6556 (2010).
13. Burden, D. K., Barlow, D. E., Spillmann, C. M., Orihuela, B., Rittschof, D., Everett, R. K. & Wahl, K. J. Barnacle Balanus amphitrite Adheres by a Stepwise Cementing Process. *Langmuir* **28,** 13364–13372 (2012).
14. Crisp, D. J., Walker, G., Young, G. A. & Yule, A. B. Adhesion and substrate choice in mussels and barnacles. *Journal of Colloid and Interface Science* **104,** 40–50 (1985).
15. Fears, K. P., Orihuela, B., Rittschof, D. & Wahl, K. J. Acorn Barnacles Secrete Phase-Separating Fluid to Clear Surfaces Ahead of Cement Deposition. *Adv. Sci.* **5,** 1700762 (2018).
16. Dickinson, G. H., Vega, I. E., Wahl, K. J., Orihuela, B., Beyley, V., Rodriguez, E. N., Everett, R. K., Bonaventura, J. & Rittschof, D. Barnacle cement: a polymerization model based on evolutionary concepts. *Journal of Experimental Biology* **212,** 3499–3510 (2009).
17. Walker, G. The Biochemical Composition of the Cement of two Barnacle Species, Balanus Hameri and Balanus Crenatus. *Journal of the Marine Biological Association of the United Kingdom* **52,** 429–435 (1972).
18. Okano, K., Shimizu, K., Satuito, C. G. & Fusetani, N. VISUALIZATION OF CEMENT EXOCYTOSIS IN THE CYPRIS CEMENT GLAND OF THE BARNACLE MEGABALANUS ROSA. 7
19. Ödling, K., Albertsson, C., Russell, J. T. & Mårtensson, L. G. E. An *in vivo* study of exocytosis of cement proteins from barnacle *Balanus improvisus* (D.) cyprid larva. *Journal of Experimental Biology* **209,** 956–964 (2006).
20. Burden, D. K., Spillmann, C. M., Everett, R. K., Barlow, D. E., Orihuela, B., Deschamps, J. R., Fears, K. P., Rittschof, D. & Wahl, K. J. Growth and development of the barnacle *Amphibalanus amphitrite* : time and spatially resolved structure and chemistry of the base plate. *Biofouling* **30,** 799–812 (2014).
21. Kamino, K., Inoue, K., Maruyama, T., Takamatsu, N., Harayama, S. & Shizuri, Y. Barnacle Cement Proteins. *Journal of Biological Chemistry* **275,** 27360–27365 (2000).

22. Kamino, K. Underwater Adhesive of Marine Organisms as the Vital Link Between Biological Science and Material Science. *Mar Biotechnol* **10,** 111–121 (2008).
23. Kamino, K. Mini-review: Barnacle adhesives and adhesion. *Biofouling* **29,** 735–749 (2013).
24. Kamino, K. Novel barnacle underwater adhesive protein is a charged amino acid-rich protein constituted by a Cys-rich repetitive sequence. 5 (2001).
25. Kamino, K. Molecular Design of Barnacle Cement in Comparison with Those of Mussel and Tubeworm. *The Journal of Adhesion* **86,** 96–110 (2010).
26. Mohanram, H., Kumar, A., Verma, C. S., Pervushin, K. & Miserez, A. Three-dimensional structure of *Megabalanus rosa* Cement Protein 20 revealed by multi-dimensional NMR and molecular dynamics simulations. *Phil. Trans. R. Soc. B* **374,** 20190198 (2019).
27. Kumar, A., Mohanram, H., Li, J., Le Ferrand, H., Verma, C. S. & Miserez, A. Disorder–Order Interplay of a Barnacle Cement Protein Triggered by Interactions with Calcium and Carbonate Ions: A Molecular Dynamics Study. *Chem. Mater.* **32,** 8845–8859 (2020).
28. Kamino, K., Odo, S. & Maruyama, T. Cement Proteins of the Acorn-Barnacle, *Megabalanus rosa*. *The Biological Bulletin* **190,** 403–409 (1996).
29. Urushida, Y., Nakano, M., Matsuda, S., Inoue, N., Kanai, S., Kitamura, N., Nishino, T. & Kamino, K. Identification and functional characterization of a novel barnacle cement protein: Barnacle surface-cement protein. *FEBS Journal* **274,** 4336–4346 (2007).
30. Sullan, R. M. A., Gunari, N., Tanur, A. E., Chan, Y., Dickinson, G. H., Orihuela, B., Rittschof, D. & Walker, G. C. Nanoscale structures and mechanics of barnacle cement. *Biofouling* **25,** 263–275 (2009).
31. Nakano, M. & Kamino, K. Amyloid-like Conformation and Interaction for the Self-Assembly in Barnacle Underwater Cement. *Biochemistry* **54,** 826–835 (2015).
32. De Gregorio, B. T., Stroud, R. M., Burden, D. K., Fears, K. P., Everett, R. K. & Wahl, K. J. Shell Structure and Growth in the Base Plate of the Barnacle *Amphibalanus amphitrite*. *ACS Biomater. Sci. Eng.* **1,** 1085–1095 (2015).
33. Mori, Y., Urushida, Y., Nakano, M., Uchiyama, S. & Kamino, K. Calcite-specific coupling protein in barnacle underwater cement: Calcite-coupling protein in underwater adhesive. *FEBS Journal* **274,** 6436–6446 (2007).

34. So, C. R., Liu, J., Fears, K. P., Leary, D. H., Golden, J. P. & Wahl, K. J. Self-Assembly of Protein Nanofibrils Orchestrates Calcite Step Movement through Selective Nonchiral Interactions. *ACS Nano* **9,** 5782–5791 (2015).
35. So, C. R., Scancella, J. M., Fears, K. P., Essock-Burns, T., Haynes, S. E., Leary, D. H., Diana, Z., Wang, C., North, S., Oh, C. S., Wang, Z., Orihuela, B., Rittschof, D., Spillmann, C. M. & Wahl, K. J. Oxidase Activity of the Barnacle Adhesive Interface Involves Peroxide-Dependent Catechol Oxidase and Lysyl Oxidase Enzymes. *ACS Appl. Mater. Interfaces* **9,** 11493–11505 (2017).
36. Wu, C., Sun, Z. & Liu, L.-S. Quantitative control of $CaCO_3$ growth on quartz crystal microbalance sensors as a signal amplification method. *Analyst* **142,** 2547–2551 (2017).
37. Aizenberg, J., Black, A. J. & Whitesides, G. M. Control of crystal nucleation by patterned self-assembled monolayers. *Nature* **398,** 495–498 (1999).
38. Aizenberg Joanna, Muller David A., Grazul John L., & Hamann D. R. Direct Fabrication of Large Micropatterned Single Crystals. *Science* **299,** 1205–1208 (2003).
39. Love, J. C., Estroff, L. A., Kriebel, J. K., Nuzzo, R. G. & Whitesides, G. M. Self-Assembled Monolayers of Thiolates on Metals as a Form of Nanotechnology. *Chem. Rev.* **105,** 1103–1170 (2005).
40. Han, Y.-J. & Aizenberg, J. Face-Selective Nucleation of Calcite on Self-Assembled Monolayers of Alkanethiols: Effect of the Parity of the Alkyl Chain. *Angew. Chem.* **115,** 3796–3798 (2003).
41. Morimoto, R. Cells in stress: transcriptional activation of heat shock genes. *Science* **259,** 1409 (1993).
42. Addadi, L., Moradian, J., Shay, E., Maroudas, N. G. & Weiner, S. A chemical model for the cooperation of sulfates and carboxylates in calcite crystal nucleation: Relevance to biomineralization. *Proc Natl Acad Sci USA* **84,** 2732 (1987).
43. Gower, L. B. & Odom, D. J. Deposition of calcium carbonate films by a polymer-induced liquid-precursor (PILP) process. *Journal of Crystal Growth* **210,** 719–734 (2000).
44. Farmer, V. C. *Infrared spectra of minerals*. (Mineralogical society, 1974).
45. Decius, J. C. & Hexter, R. M. *Molecular vibrations in crystals*. (McGraw-Hill, 1977).

46. Hamada, Y., Nishimura, Y. & Tsuboi, M. Infrared spectrum of trans-acrolein. *Chemical physics* **100,** 365–375 (1985).
47. Giasson, S., Palermo, T., Buffeteau, T., Desbat, B. & Turlet, J. M. Study of boundary film formation with overbased calcium sulfonate by PM-IRRAS spectroscopy. *Thin Solid Films* **252,** 111–119 (1994).
48. Socrates, G. *Infrared and Raman characteristic group frequencies: tables and charts*. (John Wiley & Sons, 2004).
49. Sauerbrey, G. Verwendung von Schwingquarzen zur Wägung dünner Schichten und zur Mikrowägung. *Zeitschrift für Physik* **155,** 206–222 (1959).
50. Rodahl, M., Höök, F., Krozer, A., Brzezinski, P. & Kasemo, B. Quartz crystal microbalance setup for frequency and *Q* -factor measurements in gaseous and liquid environments. *Review of Scientific Instruments* **66,** 3924–3930 (1995).
51. Curie, P. & Curie, J. Développement par compression de l'électricité polaire dans les cristaux hémièdres à faces inclinées. *Bulletin de Minéralogie* 90–93 (1880).
52. Tanuma, S., Powell, C. J. & Penn, D. R. Calculations of electron inelastic mean free paths. V. Data for 14 organic compounds over the 50-2000 eV range. *Surf. Interface Anal.* **21,** 165–176 (1994).
53. SUGIHARA, K., TERANISHI, T., SHIMAZU, K. & UOSAKI, K. Structure dependence of the surface pKa of mercaptoundecanoic acid SAM on gold. *Electrochemistry* **67,** 1172–1174 (1999).
54. Ihli, J., Wong, W. C., Noel, E. H., Kim, Y.-Y., Kulak, A. N., Christenson, H. K., Duer, M. J. & Meldrum, F. C. Dehydration and crystallization of amorphous calcium carbonate in solution and in air. *Nat Commun* **5,** 3169 (2014).
55. Radha, A. V., Forbes, T. Z., Killian, C. E., Gilbert, P. U. P. A. & Navrotsky, A. Transformation and crystallization energetics of synthetic and biogenic amorphous calcium carbonate. *Proceedings of the National Academy of Sciences* **107,** 16438–16443 (2010).
56. Zicovich-Wilson, C. M., Pascale, F., Roetti, C., Saunders, V. R., Orlando, R. & Dovesi, R. Calculation of the vibration frequencies of α-quartz: The effect of Hamiltonian and basis set. *Journal of Computational Chemistry* **25,** 1873–1881 (2004).

57. Pascale, F., Zicovich-Wilson, C. M., Orlando, R., Roetti, C., Ugliengo, P. & Dovesi, R. Vibration frequencies of Mg3Al2Si3O12 pyrope. An ab initio study with the CRYSTAL code. *The Journal of Physical Chemistry B* **109,** 6146–6152 (2005).
58. Pascale, F., Catti, M., Damin, A., Orlando, R., Saunders, V. & Dovesi, R. Vibration frequencies of Ca3Fe2Si3O12 andradite: an ab initio study with the CRYSTAL code. *The Journal of Physical Chemistry B* **109,** 18522–18527 (2005).
59. Orlando, R., Torres, F., Pascale, F., Ugliengo, P., Zicovich-Wilson, C. & Dovesi, R. Vibrational spectrum of katoite Ca3Al2 [(OH) 4] 3: a periodic ab initio study. *The Journal of Physical Chemistry B* **110,** 692–701 (2006).
60. Noël, Y., De La Pierre, M., Maschio, L., Rérat, M., Zicovich-Wilson, C. & Dovesi, R. Electronic structure, dielectric properties and infrared vibrational spectrum of fayalite: An ab initio simulation with an all-electron Gaussian basis set and the B3LYP functional. *International Journal of Quantum Chemistry* **112,** 2098–2108 (2012).
61. Demichelis, R., Suto, H., Noël, Y., Sogawa, H., Naoi, T., Koike, C., Chihara, H., Shimobayashi, N., Ferrabone, M. & Dovesi, R. The infrared spectrum of ortho-enstatite from reflectance experiments and first-principle simulations. *Monthly Notices of the Royal Astronomical Society* **420,** 147–154 (2012).
62. De La Pierre, M., Carteret, C., Orlando, R. & Dovesi, R. Use of ab initio methods for the interpretation of the experimental IR reflectance spectra of crystalline compounds. *Journal of computational chemistry* **34,** 1476–1485 (2013).
63. Dovesi, R., De La Pierre, M., Ferrari, A. M., Pascale, F., Maschio, L. & Zicovich-Wilson, C. M. The IR vibrational properties of six members of the garnet family: A quantum mechanical ab initio study. *American Mineralogist* **96,** 1787–1798 (2011).
64. Dovesi, R., Valenzano, L., Pascale, F., Zicovich-Wilson, C. & Orlando, R. Ab initio quantum-mechanical simulation of the Raman spectrum of grossular. *Journal of Raman Spectroscopy: An International Journal for Original Work in all Aspects of Raman Spectroscopy, Including Higher Order Processes, and also Brillouin and Rayleigh Scattering* **40,** 416–418 (2009).
65. Van Santen, R. A. The Ostwald step rule. *J. Phys. Chem.* **88,** 5768–5769 (1984).

66. Rieger, J., Hädicke, E., Rau, I. & Boeckh, D. A rational approach to the mechanisms of incrustation inhibition by polymeric additives/Wirkungsweise von polymeren Inkrustrationsinhibitoren. *Tenside Surfactants Detergents* **34,** 430–435 (1997).
67. Söhnel, O. & Mullin, J. W. Precipitation of calcium carbonate. *Journal of Crystal Growth* **60,** 239–250 (1982).
68. Mann, S. The chemistry of form. *Angewandte Chemie International Edition* **39,** 3392–3406 (2000).
69. Wray, J. L. & Daniels, F. Precipitation of Calcite and Aragonite. *J. Am. Chem. Soc.* **79,** 2031–2034 (1957).
70. Ogino, T., Suzuki, T. & Sawada, K. The formation and transformation mechanism of calcium carbonate in water. *Geochimica et Cosmochimica Acta* **51,** 2757–2767 (1987).
71. Van Driessche, A. E., Kellermeier, M., Benning, L. G. & Gebauer, D. *New perspectives on mineral nucleation and growth: from solution precursors to solid materials*. (Springer, 2016).
72. Voinova, M. V., Rodahl, M., Jonson, M. & Kasemo, B. Viscoelastic Acoustic Response of Layered Polymer Films at Fluid-Solid Interfaces: Continuum Mechanics Approach. *Phys. Scr.* **59,** 391–396 (1999).
73. Liu, S.-T. & Nancollas, G. H. The crystal growth of calcium sulfate dihydrate in the presence of additives. *Journal of Colloid and Interface Science* **44,** 422–429 (1973).
74. van der Leeden, M. C., Kashchiev, D. & van Rosmalen, G. M. Effect of additives on nucleation rate, crystal growth rate and induction time in precipitation. *Journal of Crystal Growth* **130,** 221–232 (1993).
75. Lechuga-Ballesteros, D. & Rodríguez-Hornedo, N. The Relation between Adsorption of Additives and Crystal Growth Rate of L-Alanine. *Journal of Colloid and Interface Science* **157,** 147–153 (1993).
76. Reddy, M. M. Crystallization of calcium carbonate in the presence of trace concentrations of phosphorus-containing anions. *Journal of Crystal Growth* **41,** 287–295 (1977).
77. Reddy, M. M. & Nancollas, G. H. Calcite crystal growth inhibition by phosphonates. *Desalination* **12,** 61–73 (1973).

78. Asenath-Smith, E., Li, H., Keene, E. C., Seh, Z. W. & Estroff, L. A. Crystal Growth of Calcium Carbonate in Hydrogels as a Model of Biomineralization. *Adv. Funct. Mater.* **22,** 2891–2914 (2012).
79. Hood, M. A., Gold, C. S., Beyer, F. L., Sands, J. M. & Li, C. Y. Extraordinarily high plastic deformation in polyurethane/silica nanoparticle nanocomposites with low filler concentrations. *Polymer* **54,** 6510–6515 (2013).
80. Hood, M. A., Landfester, K. & Munoz-Espi, R. The role of residue acidity on the stabilization of vaterite by amino acids and oligopeptides. *Crystal growth & design* **14,** 1077–1085 (2014).
81. Innocenti Malini, R., Finney, A., Hall, S., Freeman, C. & Harding, J. The water–amorphous calcium carbonate interface and its interactions with amino acids. *Crystal Growth & Design* **17,** 5811–5822 (2017).
82. Finney, A. R., Innocenti Malini, R., Freeman, C. L. & Harding, J. H. Amino Acid and Oligopeptide Effects on Calcium Carbonate Solutions. *Crystal growth & design* **20,** 3077–3092 (2020).
83. Hermansson, M. The DLVO theory in microbial adhesion. *Colloids and surfaces B: Biointerfaces* **14,** 105–119 (1999).
84. Debye, P. & Hückel, E. De la theorie des electrolytes. I. abaissement du point de congelation et phenomenes associes. *Physikalische Zeitschrift* **24,** 185–206 (1923).
85. Kashchiev, D. & Van Rosmalen, G. Nucleation in solutions revisited. *Crystal Research and Technology: Journal of Experimental and Industrial Crystallography* **38,** 555–574 (2003).
86. Borukhin, S., Bloch, L., Radlauer, T., Hill, A. H., Fitch, A. N. & Pokroy, B. Screening the Incorporation of Amino Acids into an Inorganic Crystalline Host: the Case of Calcite. *Adv. Funct. Mater.* **22,** 4216–4224 (2012).
87. Fischer, H., Polikarpov, I. & Craievich, A. F. Average protein density is a molecular-weight-dependent function. *Protein Science* **13,** 2825–2828 (2004).
88. Fleet, M. E. Infrared spectra of carbonate apatites: ν2-Region bands. *Biomaterials* **30,** 1473–1481 (2009).

89. Arrondo, J. L. R., Muga, A., Castresana, J. & Goñi, F. M. Quantitative studies of the structure of proteins in solution by Fourier-transform infrared spectroscopy. *Progress in biophysics and molecular biology* **59,** 23–56 (1993).
90. Stuart, B. H. *Infrared spectroscopy: fundamentals and applications*. (John Wiley & Sons, 2004).
91. Yang, H., Yang, S., Kong, J., Dong, A. & Yu, S. Obtaining information about protein secondary structures in aqueous solution using Fourier transform IR spectroscopy. *Nat Protoc* **10,** 382–396 (2015).
92. Knowles, T. P. J. & Buehler, M. J. Nanomechanics of functional and pathological amyloid materials. *Nature Nanotechnology* **6,** 469–479 (2011).
93. Münch, J., Rücker, E., Ständker, L., Adermann, K., Goffinet, C., Schindler, M., Wildum, S., Chinnadurai, R., Rajan, D., Specht, A., Giménez-Gallego, G., Sánchez, P. C., Fowler, D. M., Koulov, A., Kelly, J. W., Mothes, W., Grivel, J.-C., Margolis, L., Keppler, O. T., Forssmann, W.-G. & Kirchhoff, F. Semen-Derived Amyloid Fibrils Drastically Enhance HIV Infection. *Cell* **131,** 1059–1071 (2007).
94. Smith, J. F., Knowles, T. P. J., Dobson, C. M., MacPhee, C. E. & Welland, M. E. Characterization of the nanoscale properties of individual amyloid fibrils. *Proc Natl Acad Sci USA* **103,** 15806 (2006).
95. Fukuma, T., Mostaert, A. S. & Jarvis, S. P. Explanation for the mechanical strength of amyloid fibrils. *Tribology Letters* **22,** 233–237 (2006).

Chapter 6 Antimicrobial activity and Amyloid-like Structure of MrCP19

The potential antimicrobial activities of MrCP19 and MrCP20 were evaluated using E. coli and other bacteria strains. Minimum inhibitory concentration of MrCPs was measured using the broth dilution method. Together with the Kirby-Bauer test, MrCP19 showed potential bacterial inhibiting activity, which is sufficiently strong to terminate bacterial cell growth. TEM micrographs illustrated that, in contrast to the control sample, the morphology of E. coli cells is affected by exposure to MrCP19. MrCP19 in the presence of bacteria assembled into distinct and long nanofibers reminiscent of amyloid formation. Using the thioflavin T (ThT) assay, the influence of bacteria cells on amyloid formation of the proteins is also studied. Moreover, fluorescence microscopy revealed aggregation behavior of the cells in the presence of MrCP19.

6.1 Introduction

In marine environment, underwater adhesion of fouling organisms is challenging as interfacial water layers and additional biofilms form on the submerged surfaces.[1–3] Biofilms are complex microbial assemblages embedded within extracellular polymeric substances (EPS) matrix.[4] The marine biofilms' influence on biofouling process has been studied to develop eco-friendly biofouling control strategies.[5]

Barnacle, as a dominant macrofouling organism, is under particular scrutiny as it settles firmly on different substrates irrespective of the different environmental conditions. In order to understand the fouling process, it is necessary to understand the structure of barnacle's base material, the surface structure to which barnacle attaches, and the communication system between the surface and the barnacle.

Detecting appropriate substratum to settle is a critical stage for barnacles to subsequently secure adhesion. Recent studies indicate that marine biofilms can guide barnacle larval recruitment for pre-settlement assessment, thereby either promoting or discouraging barnacle biofouling.[6–9] Variety of sources composing the biofilm such as quorum sensing (QS) molecules, or ion channels with different electrical signals, provide important cues.[5] Following the communication between the biofilm and the barnacles for pre-settlement, firm and irreversible settlement using cement adhesive takes place.[10] During the first stage of permanent attachment, lipids have been observed to clean the surface and to protect the adhesive proteins from excessive hydration and bacterial degradation.[11,12] However, dead bacteria cells were still observed underneath the juvenile barnacle base plate, with a high density of dead bacteria located close to the cyprid antennule adhesive plaques and a mixture of live and dead bacteria around the cuticle.[13] The presence or even condensation of bacteria cells underneath the barnacle followed by their eradication have not been completely understood.

Recent studies observing dead bacteria underneath the barnacle base plate support the intriguing hypothesis that one of the cement proteins performs antibacterial activity.[11,13–15]

As MrCP19 is suggested to be located in the interfacial layer of cement adjacent to the external substratum, the interaction between the protein and bacteria cells was investigated for its potential antimicrobial activity. MrCP20 was used as comparison for some experiments. Zone of inhibition test and Minimum Inhibitory Concentration (MIC) assay were performed to identify the minimum protein concentration for effective bactericidal activity. TEM observations indicated partial cell rupture in the presence of MrCP19 as well as protein fibrillization. The fibrillization of MrCP19 into amyloid-like nanofibrils at the cell membrane was confirmed using the thioflavin T (ThT) assay. Lastly, fluorescence microscopy was used to compare the live/dead behavior *E.coli* of in the presence or absence of the protein.

6.2 Materials and Methods

6.2.1 Zone of Inhibition Test (The Kirby-Bauer Test)

Mueller-Hinton (MH) agar was autoclaved at 121°C for 15 minutes and cooled down to be poured into the plates to a depth of approximately 4 mm. The plates were placed under the hood, partially covered with the lid, until the agar was fully solidified. The plates were used directly or after storage at 4 °C.

A single colony of *E. coli* was precultured in Mueller-Hinton broth (MHB) to mid-log phase and then diluted to an OD_{600} value of 0.05. Using a sterile swab, a drop of inoculum was taken and spread on prepared MH agar plate by streaking the swab and rotating the plate for even distribution of inoculum. A paper disk containing MrCP up to 1 mg/mL of concentration was put in the middle of agar plates, gently pressed to ensure complete contact with the agar surface. The zone of inhibition was observed after the plates were incubated at 35 °C for 16-18 hours.

6.2.2 Minimum Inhibitory Concentration (MIC) Verification

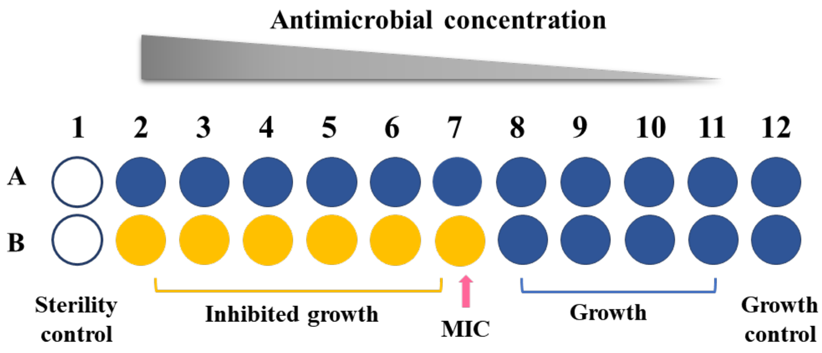

Figure 6.1 A schematic representation of a typical MIC assay plate. The wells in the column 2-11 at the top of the plate contain an antimicrobial agent at decreasing concentration from column 2 down to column 11. The MIC is defined as the lowest concentration preventing visible growth of microorganism. The well in column 1 is sterility control (antimicrobial agent without bacteria) and the well in column 12 is positive control (bacteria solution without antimicrobial agent).

Figure 6.1 depicts a typical MIC assay, where MIC is defined as the lowest concentration that can inhibit cell growth. The negative control (sterility control, antimicrobial agent without bacteria) and positive control (growth control, bacteria solution without antimicrobial agent) were used to check the sterility of sample and the stability of bacteria cells, respectively. From column 2, 50 µL of 2.6 mg/mL protein solution was serially diluted in two-fold, and the last 50 µL from column 11 was discarded. To prepare bacteria solutions, the gram-positive and gram-negative bacteria, *Enterococcus faecalis* (*E. faecalis)* and *Pseudomonas aeruginosa (PAO1)* strains, respectively, were grown in Mueller-Hinton broth (MHB) media to mid-log phase. The cultured bacteria solution was diluted to contain target Colony-forming unit per volume (CFU/mL) of 10^6. 50 µL of the solution was added to each well of 96-well plate, to make the total measurement volume of 100 µL for each well. The plates were covered but not sealed, to allow gas exchange, and they were inserted into a Spark multimode microplate reader (Tecan) with the temperature set to 35 °C. OD_{600}

readings were taken every 30 minutes for 24 hours, with orbital shaking at 180 rpm between reads.

6.2.3 TEM

E. coli cells were incubated with various concentrations of MrCP19 or MrCP20 proteins (0.5 mg/mL, 1 mg/mL) for 2 hours at 35 °C. The cells were centrifuged at 5000 rpm for 5 minutes, and the pellet was resuspended in 10 µL of Tris buffer (pH 8.3). A drop containing protein with treated or untreated bacteria was loaded onto copper-coated electron microscopy grids. The grids were then negatively stained with 2% phosphotungstic acid (PTA) for a better contrast giving dark hallow on the edge of the biological samples. The samples were examined using Energy filtered Carl Zeiss TEM, LIBRA® 120 with in-column Omega spectrometer.

6.2.4 ThT Assay for Assembled β-sheet Detection

Thioflavin T (ThT) was used for amyloid detection as described in **Chapter 3.2.5**. The sample solution of 120 µL was prepared in each well of 96-microwell plate (Thermo Fisher Scientific-Nuclon). 50 µL of protein solution was prepared with two-fold serial dilution starting from 2.7 mg/mL. 50 µL of bacteria solution and 20 µL ThT solution was added to reach the final CFU/mL of 10^6, the final ThT concentration of 16 µM, and the final sample volume of 120 µL. The fluorescence was measured at an excitation at 440 nm and emission of 485 nm, every 15 minute for 24 hours at 35 ºC using Infinite 200 Pro (Tecan, Switzerland). Each measurement was averaged from 9 readings per well, followed by 5 seconds orbital shaking.

6.2.5 Fluorescence Microscopy

Fluorescence imaging was performed on a wide-field deconvolution fluorescence microscopy (DeltaVision, Applied Precision, Inc., USA), using 60X/1.42 objective from Olympus and FITC filter. The sample solutions of bacteria incubated with proteins were prepared in a 96-microwell plate. Each well contained 100 µL of precultured *E. coli* solution (2 x 10^6 CFU/mL) with 100 µL of MrCP19 or MrCP20 in "Tris" (20 mM Tris, 150 mM NaCl) or "AA" (20 mM acetic acid buffer, 150 mM NaCl) (2 x 1 mg/mL). The images were taken after one hour of incubation and 20 hours of incubation at 35 ^{o}C.

6.3 Results and Discussion

6.3.1 Weak Inhibitory Effect of MrCP19 on Bacteria

6.3.1.1 Zone of Inhibition

The zone of inhibition test, or also known as Kirby-Bauer disk diffusion method, was performed to assess the antimicrobial activity of the proteins in relation to *E. coli*. (**Figure 6.2**) Only 1 mg/mL MrCP19 showed a zone of inhibition with the diameter of 20 mm, whereas 0.8 mg/mL of MrCP19 showed a smaller inhibition zone with a diameter of 13 mm, while MrCP20 did not show any zone of inhibition. According to previously reported inhibition zone diameter of prescribed antibiotics against *E. coli*, 20 mm indicates that the bacteria is in the boundary range between susceptible and resistant.[16–20]

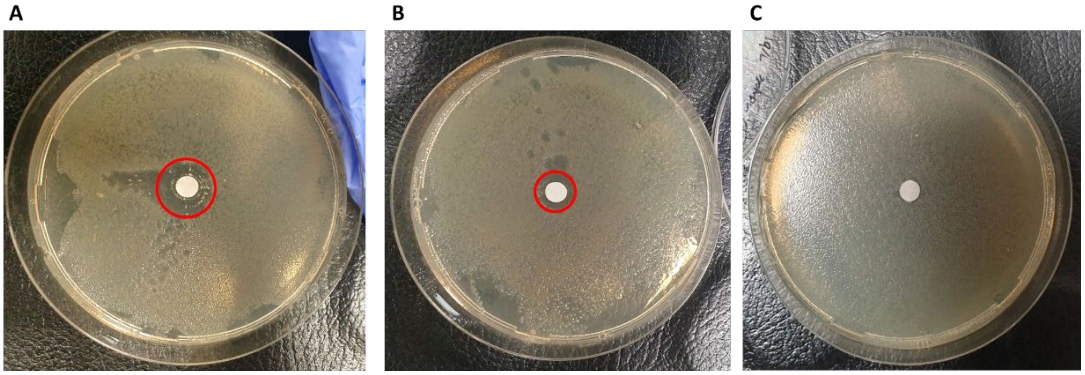

Figure 6.2 Inhibition zone diameter of **(A)** 20 mm observed with 1 mg/mL of MrCP19, **(B)** 13 mm observed with 0.8 mg/mL of MrCP19, while **(C)** no zone of inhibition was observed with 1 mg/mL of MrCP20.

6.3.1.2 Minimum Inhibitory Concentration

MIC is the lowest concentration of an antimicrobial agent that prevents visible growth of a microorganism. This MIC assay can provide quantitative information of the exact concentration needed to inhibit the bacterial growth, compared to Kirby-Bauer method.[21] In order to assess the proteins inhibitory effect on bacterial growth, MIC assay was conducted with both gram-positive and gram-negative cells, using *E. faecalis* and *PAO1* strains, respectively. *PAO1* is known to be more resistant to antibiotics than *E.coli*, due to extremely restricted membrane permeability.[22–24]

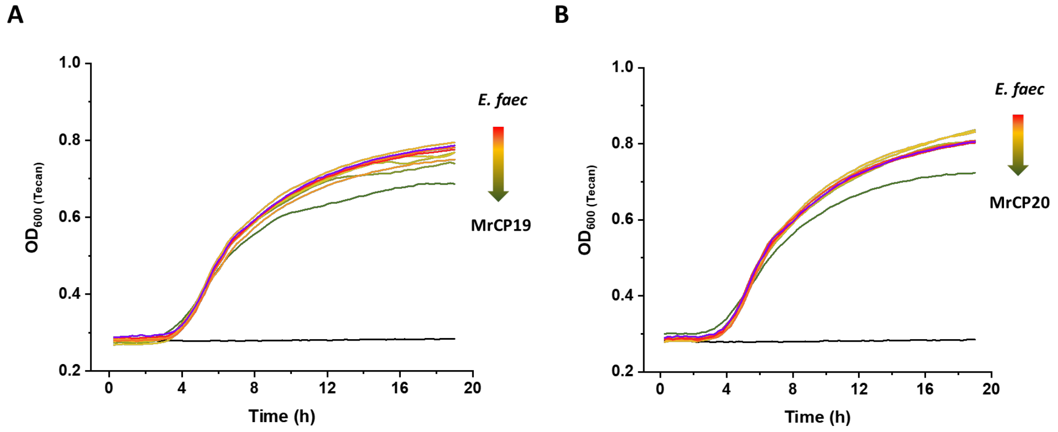

Figure 6.3 Cell growth of *E. faecalis* observed for 24 hours, incubated with different concentration of **(A)** MrCP19 or **(B)** MrCP20. The black curve indicates negative control showing no cell growth, and the blue curve indicates positive control showing bacterial growth without the presence of protein. The curves in between contain decreasing protein concentration in two-fold starting from 1.3 mg/mL (green) down to 2.5 µg/mL (red).

MrCP19 incubated with *E. faecalis* (**Figure 6.3A**) showed a bactericidal efficiency of 13.7 % (1.3 mg/mL) and 6.3 % (0.65 mg/mL). Lower concentration of the proteins (under 0.1 mg/mL) still showed growth inhibition but eventually the bacteria had all grown after 24 h. For the lowest concentration of MrCP19 (10 µg/mL and below), the growth curve was almost identical to the positive control. MrCP20 also showed weak inhibitory affect by 11.1 % (1.3 mg/mL), and at the lowest concentration, it had no effect on bacterial growth (**Figure 6.3B**). Both protein solutions were confirmed to be sterilized from the black curve whose OD values were consistent during the experiment.

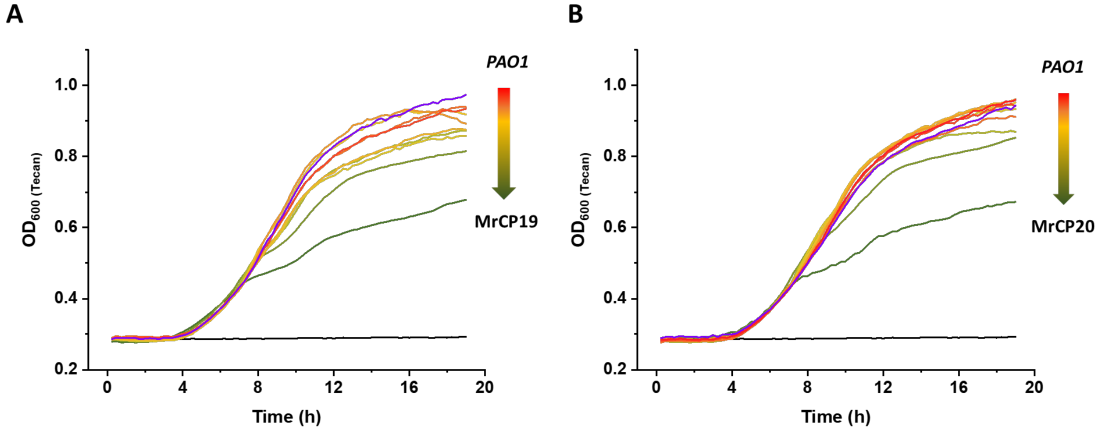

Figure 6.4 Cell growth of *PAO1* observed for 24 hours, incubated with different concentrations of **(A)** MrCP19 or **(B)** MrCP20. The black curve indicates negative control showing no cell growth, and the blue curve indicates positive control showing bacterial growth without the presence of protein. The curves in between contain decreasing protein concentration in two-fold starting from 1.3 mg/mL (green) down to 2.5 µg/mL (red).

A more significant bactericidal effect of both proteins was detected for *PAO1*. MrCP19 incubated with *PAO1* showed a bactericidal efficiency of 30.3 % at 1.3 mg/mL) and 16.3 % at 0.65 mg/mL (**Figure 6.4A**). At lower protein concentrations (under 0.1 mg/mL), an inhibitory effect was still observed on the growth curve. MrCP20 also showed an inhibitory efficiency of 30.0 % at 1.3 mg/mL) and of 11.2 % at 0.65 mg/mL. However, at lower proteins had concentration, there were no effect on bacterial growth (**Figure 6.4B**). Both protein solutions were confirmed to be sterilized from the black curves whose OD values were consistent during the experiment.

In summary, both proteins showed improved inhibitory effect for gram-negative *PAO1* compared to gram-positive *E. faecalis*. *PAO1* and *E. faecalis* have differences in structure, thickness, and composition of cells, but the main difference is that gram-negative cells have double membrane layers while gram-positive cells have only a single plasma membrane which is covered with a thick peptidoglycan layer on the outmost part.[25] Gram-negative cells possess a much thinner peptidoglycan layer between the outer membrane containing lipopolysaccharides (LPS), and the inner membrane. These results suggest that the presence of membrane, and thus membrane permeability, is important for the proteins to exhibit antimicrobial activity. On the other hand, the bactericidal activities of the two proteins were quite similar. At the protein concentration of 1.3 mg/mL, MrCP19 was slightly more effective than MrCP20, and at lower concentration, MrCP19 showed better bactericidal activity. Still the result was not as efficient as commercial antimicrobial agents due to the experimental limitations, such as the restricted concentration of the proteins and the experimental temperature over 35 ^{o}C for bacteria growth, which is not favorable for the proteins.

6.3.2 Potential Link Between Antimicrobial Activity and Amyloid-like Structure

6.3.2.1 TEM

To identify the cell membrane damage of bacteria caused by barnacle cement proteins, TEM images of *E. coli* treated with the cement proteins at 0.5 mg/mL or 1 mg/mL were obtained and compared with untreated *E. coli*.

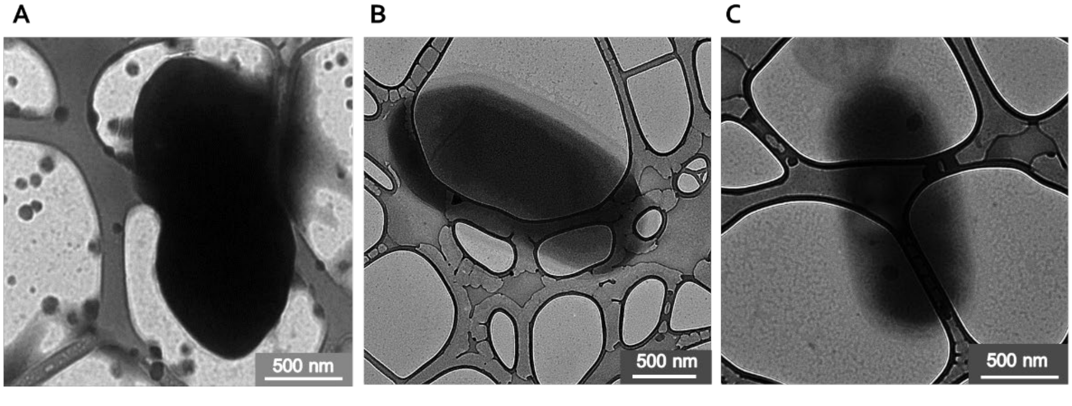

Figure 6.5 TEM images of negatively stained *E. coli* **(A)** in the absence or in the presence of **(B)** 0.5 mg/mL or **(C)** 1 mg/mL of MrCP20. Smooth cell surface was observed regardless of the presence of MrCP20.

Bacteria cells that were not exposed to proteins displayed intact cell membranes with no modification **(Figure 6.5A)**. The dark spots observed in the micrographs are due to the staining dye. These results were compared to the *E. coli* sample incubated with 0.5 mg/mL or 1.0 mg/mL MrCP20, which showed no cell membrane damage. **(Figure 6.5B-C)** Similar patterns were observed throughout the whole sample.

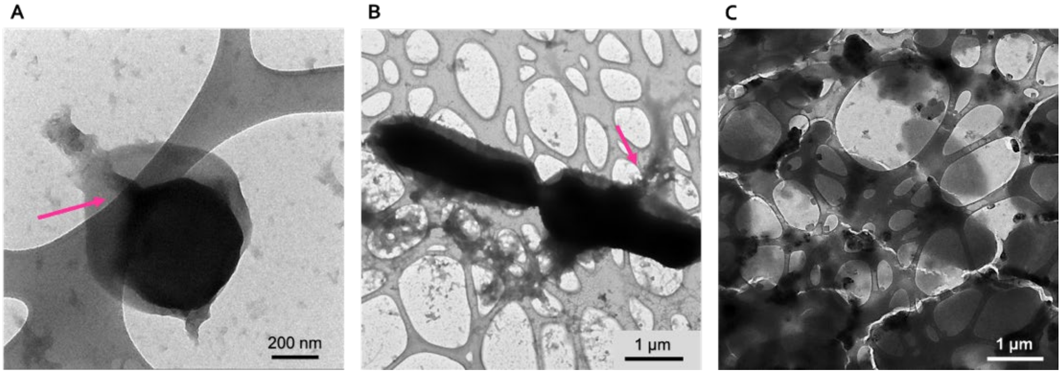

Figure 6.6 TEM images of *E. coli* sample in the presence of **(A-B)** 0.5 mg/mL or **(C)** 1 mg/mL of MrCP19 were taken. A small blebbing or swelling of the cell membrane was observed in (**A**), and a greater damage and large protrusion on the cell wall was observed in **(B)**. Smooth cell membranes were hardly detected at higher concentration of MrCP19 (**C**).

In contrast, the morphology of the MrCP19-treated bacteria showed blebbing features around the cells surface (**Figure 6.6A**). Even more severe protrusions of the cell membrane were observed **(Figure 6.6B)**. *E. coli* treated with a higher concentration of MrCP19 showed multiple spots of blebbing and protrusions, whereas intact smooth cell membranes were hardly detected **(Figure 6.6C)**. The same patterns were consistent for most of the cells throughout the grid surface.

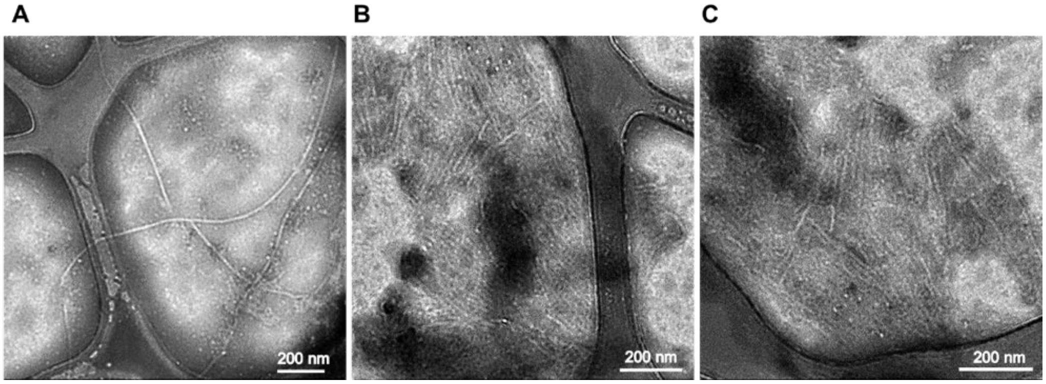

Figure 6.7 TEM images of *E. coli* incubated with 0.5 mg/mL of MrCP19, showing fibrous structures with a length ranging from 200 nm **(B-C)** to over 1 μm **(A)**.

Interestingly, bacteria with 0.5 mg/mL MrCP19 sample were decorated with unique fibrous structures. Thin and long (over 1 μm) fibers were observed as shown in **Figure 6.7A**, and stack of thin and short (200 nm) fibers were also observed in **Figure 6.7B-C**. Not all fibers were necessarily formed on the cell membranes since the end of the fibers could also be detected from the region far from bacteria cells. Fibers were dispersed throughout the area regardless of the local population of bacteria cells. When compared with the pure MrCP19 of 0.2 mg/mL (**Figure 4.6**), the diameter of the fibers was more consistent throughout the surface and evenly dispersed.

One antimicrobial activity mechanism exerted by antimicrobial peptides (AMPs) is through binding to the bacterial cell membrane followed by disrupting it.[26–29] Among various membrane invasion mechanisms for AMPs, one of the recent models suggests that AMPs permeate bacterial membranes via an amyloid mediated mechanism.[30,31] One model used for describing amyloid formation by AMP suggests that unstructured monomer peptides or proteins in aqueous solutions can adopt α helical structures at the membrane interface, and later undergo conformational transition to form β-sheet rich amyloid fibrils (**Figure 4.8**).[32,33]

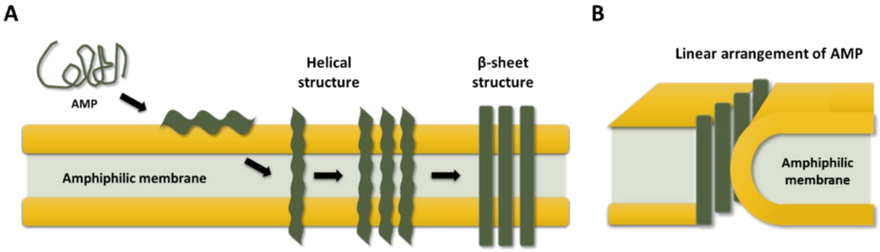

Figure 6.8 (A) Putative schematic representation for amyloid formation by amyloidogenic AMPs. Peptides attracted to the membrane undergo conformational changes into helical structures, followed by membrane penetration. It may become reoriented to accommodate amphiphilic property with alignment and oligomerization, along with the anionic lipid membrane neutralizing positively charged domains of the peptide. The oligomers might eventually adopt β-sheet conformation, aggregating and forming into amyloid fiber. **(B)** "Leaky slit" model[33] of bacterial membrane permeabilization proposes a linear arrangement of peptides possessing amphiphilic characteristics. This arrangement forces the membrane to rearrange their hydrophobic core and the hydrophilic head groups, resulting in irreversible permeabilization.

As discussed in **Chapter 2.3**, MrCP19 possesses a lot of hydrophobic residues as well as hydrophilic residues composed of similar amount of negatively charged and positively charged residues. This amphiphilic characteristic of MrCP19 is hypothesized to be a viable candidate favoring membrane binding and pore formation. Furthermore, the protein can undergo conformational change to accommodate amphiphilic characteristics during alignment and oligomerization upon membrane binding, which might eventually adopt β-sheet conformation, aggregating and forming amyloid fibers.[32] The anti-bacterial activity of MrCP19, or more precisely bacteria membrane disruption behavior of MrCP19 together with fibril formation, is further discussed in the following section to better understanding the membrane invasion mechanism.

6.3.2.2 ThT Assay

ThT assay can provide quantitative information on amyloid fibril formation by fluorescence intensity arising from ThT dye bound to consecutive β-sheet structures, as discussed in **Chapter 3.3.3**.[34–38] In order to assess the proteins fibril formation in the presence of bacteria membrane, ThT assay was conducted using *E. coli* as well as *PAO1* strains, as both species contain LPS as the outmost layer of their cell membrane.

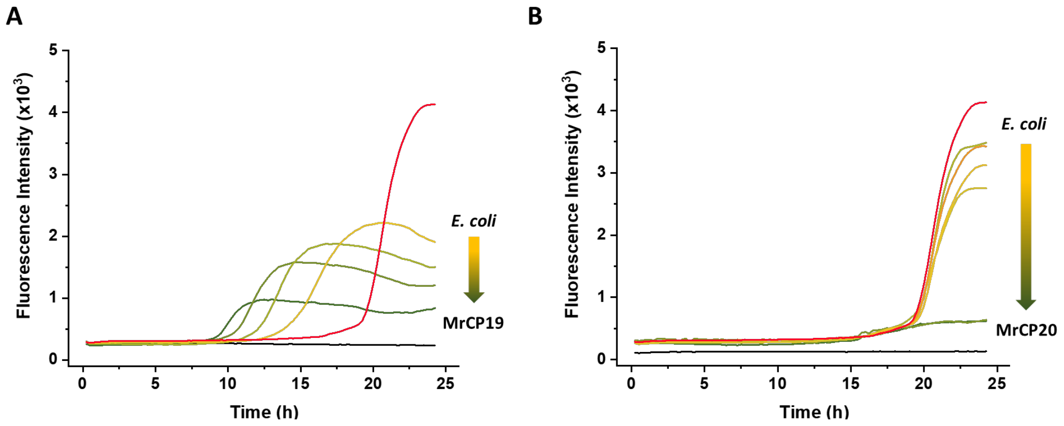

Figure 6.9 Fluorescence intensity measurements during amyloid fibril formation using ThT assay conducted with **(A)** MrCP19 or **(B)** MrCP20 incubated with *E. coli* in MHB. The black curve indicates negative control of pure protein solution showing no cell growth, and the red curve is positive control of pure bacteria solution without any protein. The curves in the middle contain decreasing protein concentration in two-fold starting from 1.3 mg/mL (green) down to less than 100 μg/mL (yellow).

The results of ThT assay on *E. coli* incubated with MrCPs are shown in **Figure 6.9**. *E.coli* control samples in this experiment (red curves) showed strong amyloid detection in 20 hours of incubation, attributing to the cells natural curli fibers.[39,40] Results from the protein control samples (green curves) showed that fiber quantity of the proteins is relatively marginal compared to the fiber quantity of the cells, which was carried out for 24 hours.

For bacteria samples incubated with different concentration of MrCP19 (**Figure 6.9A**), there were two main observations. (i) The fluorescence intensity from fibril structure was diminished after 24 hours for the bacteria samples with increasing amount of MrCP19. As discussed in **Chapter 6.3.1**, MrCP19 showed some bactericidal effect, and the decrease of fibril detection can be explained by inhibited growth of *E.coli* due to the protein. (ii) There is another clear trend that higher concentration of MrCP19 led to amyloid fiber formation in shorter time of incubation (more precisely, it started to show fluorescence intensity increase), which was much faster compared to the control *E. coli* sample. Once it reached a maximum intensity, it did not further increase. It is possible that MrCP19 fibril formation was triggered the cells to produce amyloid structure in shorter time starting from 9 hours and at the same time, these protein amyloid fibrils either inhibited the bacterial growth or protruded the membrane of the bacteria cells, preventing further fiber increase. Another theory is that these instant small increases of fibrils resulted from curli fibers of *E. coli* instead of protein fibers. Regarding the cell growth inhibition starting from 8-10 hours of protein treatment (**Figure 6.3-4**), the increase of curli fibers could take place upon unique interaction between MrCP19 and LPS, followed by cell protrusion and membrane damage. Different hypothesis can be tested and confirmed in the future by timewise TEM observations over 24 hours of *E. coli* with and without the protein.

MrCP20 on the other hand (**Figure 6.9B**), greatly decreased the fluorescence intensity after 24 hours of incubation at 1.3 mg/mL, and showed little decrease of fluorescence intensity for the lower concentrations. The fluorescence intensity values were comparable with that of MrCP19 for 1.3 mg/mL, but not at the lower concentrations. All inhibition of fibril formation was observed only after 20 hours, which is likely due to inhibited curli fiber growth. In contrast to MrCP19, no effect of promoting fibril formation was observed, neither forming its own amyloid fibers nor inducing curli fibers from *E. coli*. 1.3 mg/mL MrCP20 had not shown a strong bactericidal activity from the experiments, but its potential effect on curli fibril has been detected.

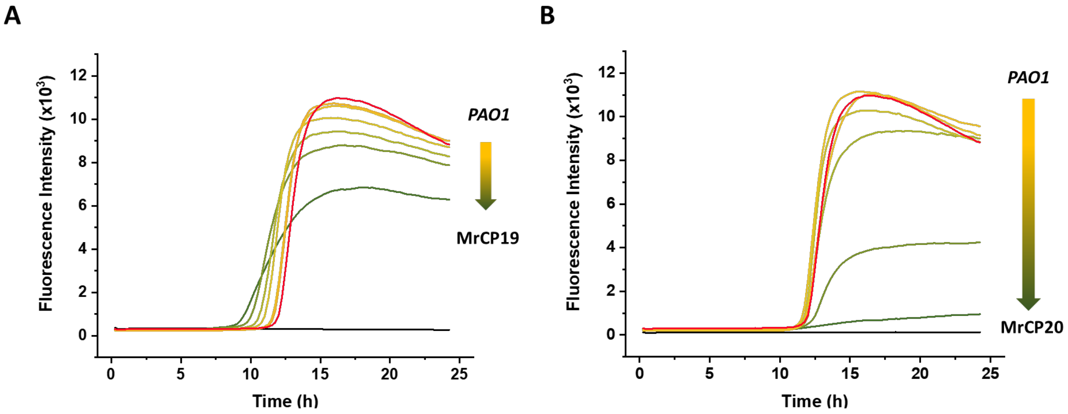

Figure 6.5 Fluorescence intensity measurement for amyloid fibril detection using ThT assay conducted with **(A)** MrCP19 or **(B)** MrCP20 incubated with *PAO1* in MHB. The black curve indicates negative control of pure protein solution showing no cell growth, and the red curve is positive control of pure bacteria solution without any protein. The curves in the middle contain decreasing protein concentration in two-fold starting from 2.25 mg/mL (green) down to less than 100 μg/mL (yellow).

The results of ThT assay on *PAO1* incubated with MrCPs are shown in the **Figure 6.10**. *PAO1* control samples in this experiment (red curves) indicated strong amyloid detection within 10 hours of incubation, due to their own amyloid fibrils, mainly the wild type FapC protein.[41,42] Similar with *E. coli* containing curli fiber, *PAO1* is known to utilize the functional amyloid fibrils to fortify the biofilm extracellular matrix. Results from the protein control samples (green curves) show that fiber quantity of the proteins was relatively marginal compared to the fiber quantity of the cells, which was carried out during for 24 hours.

Similar with the results from **Figure 6.9**, increasing the protein concentration tended to reduce the fluorescence intensity of *PAO1* incubated with MrCPs after 24 hours. Considering that the bacterial growth inhibition effect of the two proteins on *PAO1* was quite similar (**Figure 6.4**), MrCP20 inhibited fiber growth more efficiently than MrCP19, or fibers from MrCP19 contributed to the ThT detection. It is also possible that MrCP20 interferes with the fiber detection by structural hindrance surrounding β-sheet structure of curli. Higher concentration of MrCP19 (**Figure 6.10A**) enhanced fibril formation compared to the earlier incubation time but reached a weaker signal after 24 hours. On the other hand, MrCP20 (**Figure 6.10B**) did not have promote fibril formation but only resulted in a huge decrease of final fluorescence intensity. As proposed for *E. coli* samples above, MrCP19 can synergistically form amyloid fibers with FapC protein, or promote amyloid FapC protein formation by interacting with the cell membrane.

In order to achieve a better understanding of interacting mechanisms between the proteins and LPS of the gram-negative cells, AFM and ThT assay as additional experiments (the results are not shown) on vesicles, were conducted with Phosphatidylethanolamine (PE) to simply mimic *E. coli* cell membrane (75 % composed of PE). However, no vesicles were observed to experience membrane damage, nor improving fibril formation of MrCPs. More than the simplified PE structure will be required to understand mechanisms of the proteins' fiber formation upon membrane interaction and antimicrobial activity.

6.3.2.3 Fluorescence Microscopy

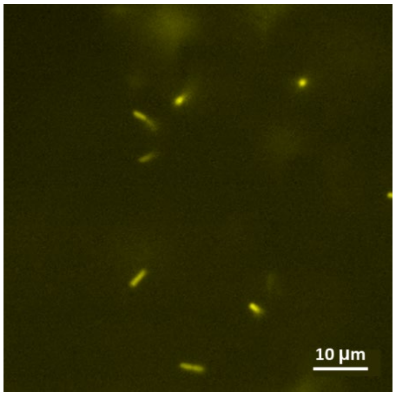

Figure 6.6 Fluorescence imaging of *E. coli* grown in MHB.

As a final method to observe the behavior of bacteria in the presence of MrCPs, fluorescence microscope images were taken after one hour and one day of incubation, respectively. Compared to the *E. coli* control sample (**Figure 6.11**), *E. coli* incubated with MrCPs at pH 8.3 and pH 3.6 for one hour showed no significant difference (**Figure 6.12A-D**). Subtle increase of the dynamic motion of the cells was observed when they were incubated with

MrCP20 (**Figure 6.12A-B**), while the opposite was observed when they were incubated with MrCP19 (**Figure 6.12C-D**).

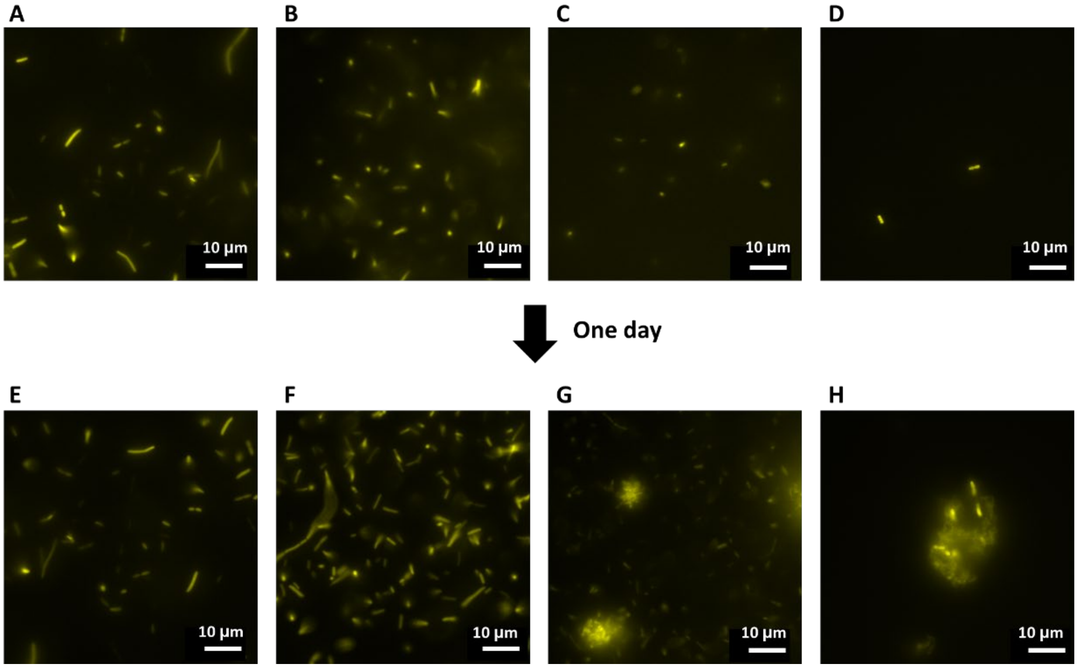

Figure 6.7 Fluorescence imaging of *E. coli* incubated with MrCP20 **(A)** in Tris or **(B)** in AA, or with MrCP19 **(C)** in Tris or **(D)** in AA, for 1 hour. They were also measured after 24 hours of incubation at 35 ºC **(E-H)**. MrCP19 in both condition **(G-H)** was observed to aggregate the cells into multiple groups.

After incubation for 24 hours in 35 ºC, an increased amount of the cells could be generally observed. Notably, a unique behavior from cells incubated with MrCP19 was identified. While *E. coli* incubated with MrCP20 (**Figure 6.12E-F**) did not show specific trend, *E. coli* incubated with MrCP19 either in Tris or in AA (**Figure 6.12G-H**) showed a clear tendency of aggregating into multiple groups. This pattern was observable throughout the sample solution. It was not possible to detect protein or fibers within the fluorescence imaging, yet we can conclude that MrCP19 affected not only cell membrane but also cell distribution. Amyloid fibrillation of MrCP19 might play a key role in interacting with the cell membrane, as well as triggering interactions between the protein and curli fibers in a way that aggregate the cells. This aggregation might be detrimental to the cells since the oxygen consumption would be locally concentrated to deplete oxygen supply.

6.4 Conclusion

In this Chapter, various microbiology tests were conducted using *E. coli* and other bacteria species to assess the potential antimicrobial activity of MrCPs. Zone of inhibition and MIC tests showed that MrCP19 exhibits a slightly stronger antimicrobial activity than MrCP20. MIC test suggested that *E. faecalis* (gram-negative bacteria) is more resistant to the proteins than *PAO1* (known to be more resistant than *E. coli*, gram-negative bacteria). TEM imaging indicated: (i) cell disruption through membrane damage or penetration, as well as (ii) fibril formation in the presence of MrCP19. From MIC test and TEM imaging, we propose an amyloid formation and penetration mechanism of the proteins as they interact with the cell membrane, with LPS that mainly composes the outer membrane of gram-negative cells.

The β-sheet propensity structure of MrCP19 seemed to be the underlying commonality for understanding both amyloid fibril formation and cell membrane permeation. Thus, ThT assay was conducted to monitor β-sheet amount of the proteins and bacteria cells, which suggested acceleration of fibril formation at increasing concentration of MrCP19 in the presence of gram-negative bacteria cells. The amphiphilic structure of the cell membrane might favor interaction with amphiphilic MrCP19, enabling antimicrobial activity. It is also plausible that MrCP19 forms fibrils are encouraged by lipid components of the putative primer, not only by bacteria cells, and this can be investigated in further experiments. On the other hand, the possibility of increased production of amyloid fibrils by the bacteria as a self-defence in the exposure to the proteins cannot be neglected.[43,44] Further studies for proving MrCP19 amyloid fibrillation without the effect of natural bacterial amyloid fibrils will strengthen our understanding of antimicrobial mechanism as one of functional roles of MrCP19.

References

1. Guezennec, J., Herry, J. M., Kouzayha, A., Bachere, E., Mittelman, M. W. & Bellon Fontaine, M. N. Exopolysaccharides from unusual marine environments inhibit early stages of biofouling. *International Biodeterioration & Biodegradation* **66,** 1–7 (2012).
2. Almeida, J. R. & Vasconcelos, V. Natural antifouling compounds: Effectiveness in preventing invertebrate settlement and adhesion. *Biotechnology Advances* **33,** 343–357 (2015).
3. Li, J., Wang, T., Yu, S., Bai, J. & Qin, S. Community characteristics and ecological roles of bacterial biofilms associated with various algal settlements on coastal reefs. *Journal of Environmental Management* **250,** 109459 (2019).
4. López, D., Vlamakis, H. & Kolter, R. Biofilms. *Cold Spring Harbor perspectives in biology* **2,** a000398 (2010).
5. Rajitha, K., Nancharaiah, Y. V. & Venugopalan, V. P. Insight into bacterial biofilm-barnacle larvae interactions for environmentally benign antifouling strategies. *International Biodeterioration & Biodegradation* **149,** 104937 (2020).
6. Khandeparker, L., Anil, A. C. & Raghukumar, S. Barnacle larval destination: piloting possibilities by bacteria and lectin interaction. *Journal of Experimental Marine Biology and Ecology* **289,** 1–13 (2003).
7. Nasrolahi, A., Stratil, S. B., Jacob, K. J. & Wahl, M. A protective coat of microorganisms on macroalgae: inhibitory effects of bacterial biofilms and epibiotic microbial assemblages on barnacle attachment. *FEMS Microbiology Ecology* **81,** 583–595 (2012).
8. De Gregoris, T. B., Khandeparker, L., Anil, A. C., Mesbahi, E., Burgess, J. G. & Clare, A. S. Characterisation of the bacteria associated with barnacle, Balanus amphitrite, shell and their role in gregarious settlement of cypris larvae. *Journal of Experimental Marine Biology and Ecology* **413,** 7–12 (2012).
9. Lee, O. O., Chung, H. C., Yang, J., Wang, Y., Dash, S., Wang, H. & Qian, P.-Y. Molecular techniques revealed highly diverse microbial communities in natural marine

biofilms on polystyrene dishes for invertebrate larval settlement. *Microbial ecology* **68,** 81–93 (2014).

10. Kamino, K. Barnacle Underwater Attachment. 24
11. Gohad, N. V., Aldred, N., Hartshorn, C. M., Jong Lee, Y., Cicerone, M. T., Orihuela, B., Clare, A. S., Rittschof, D. & Mount, A. S. Synergistic roles for lipids and proteins in the permanent adhesive of barnacle larvae. *Nat Commun* **5,** 4414 (2014).
12. Fears, K. P., Orihuela, B., Rittschof, D. & Wahl, K. J. Acorn Barnacles Secrete Phase-Separating Fluid to Clear Surfaces Ahead of Cement Deposition. *Adv. Sci.* **5,** 1700762 (2018).
13. Essock-Burns, T., Gohad, N. V., Orihuela, B., Mount, A. S., Spillmann, C. M., Wahl, K. J. & Rittschof, D. Barnacle biology before, during and after settlement and metamorphosis: a study of the interface. *Journal of Experimental Biology* jeb.145094 (2016). doi:10.1242/jeb.145094
14. Aldred, N., Gohad, N. V., Petrone, L., Orihuela, B., Liedberg, B., Ederth, T., Mount, A., Rittschof, D. & Clare, A. S. Confocal microscopy-based goniometry of barnacle cyprid permanent adhesive. *THE JOURNAL OF EXPERIMENTAL BIOLOGY* 4
15. Zardus, J. D., Nedved, B. T., Huang, Y., Tran, C. & Hadfield, M. G. Microbial biofilms facilitate adhesion in biofouling invertebrates. *The Biological Bulletin* **214,** 91–98 (2008).
16. Andrews, J. M. BSAC standardized disc susceptibility testing method (version 8). *Journal of antimicrobial chemotherapy* **64,** 454–489 (2009).
17. Kronvall, G., Giske, C. G. & Kahlmeter, G. Setting interpretive breakpoints for antimicrobial susceptibility testing using disk diffusion. *International journal of antimicrobial agents* **38,** 281–290 (2011).
18. Lorian, V. *Antibiotics in laboratory medicine*. (Lippincott Williams & Wilkins, 2005).
19. Jacoby, G. A. & Han, P. Detection of extended-spectrum beta-lactamases in clinical isolates of Klebsiella pneumoniae and Escherichia coli. *Journal of clinical microbiology* **34,** 908–911 (1996).
20. Wikler, M. A. Performance standards for antimicrobial susceptibility testing Sixteenth informational supplement. *M 100-S 16* (2006).
21. Tiller, J. C. Antimicrobial surfaces. *Bioactive surfaces* 193–217 (2010).

22. Nikaido, H., Nikaido, K. & Harayama, S. Identification and characterization of porins in Pseudomonas aeruginosa. *Journal of Biological Chemistry* **266,** 770–779 (1991).
23. Bellido, F., Martin, N. L., Siehnel, R. J. & Hancock, R. E. Reevaluation, using intact cells, of the exclusion limit and role of porin OprF in Pseudomonas aeruginosa outer membrane permeability. *Journal of bacteriology* **174,** 5196–5203 (1992).
24. Hancock, R. E. & Brinkman, F. S. Function of Pseudomonas porins in uptake and efflux. *Annual Reviews in Microbiology* **56,** 17–38 (2002).
25. Samuel, B. Medical microbiology. *The University of Texas Medical Branch at Galveston–Tx, USA* (1996).
26. Brogden, K. A. Antimicrobial peptides: pore formers or metabolic inhibitors in bacteria? *Nature reviews microbiology* **3,** 238–250 (2005).
27. Melo, M. N., Ferre, R. & Castanho, M. A. Antimicrobial peptides: linking partition, activity and high membrane-bound concentrations. *Nature Reviews Microbiology* **7,** 245–250 (2009).
28. Sengupta, D., Leontiadou, H., Mark, A. E. & Marrink, S.-J. Toroidal pores formed by antimicrobial peptides show significant disorder. *Biochimica et Biophysica Acta (BBA)-Biomembranes* **1778,** 2308–2317 (2008).
29. Nguyen, L. T., Haney, E. F. & Vogel, H. J. The expanding scope of antimicrobial peptide structures and their modes of action. *Trends in biotechnology* **29,** 464–472 (2011).
30. Harris, F., Dennison, S. R. & Phoenix, D. A. Aberrant action of amyloidogenic host defense peptides: a new paradigm to investigate neurodegenerative disorders? *The FASEB Journal* **26,** 1776–1781 (2012).
31. Kagan, B. L., Jang, H., Capone, R., Teran Arce, F., Ramachandran, S., Lal, R. & Nussinov, R. Antimicrobial properties of amyloid peptides. *Molecular pharmaceutics* **9,** 708–717 (2012).
32. Phoenix, D. A., Dennison, S. R. & Harris, F. *Antimicrobial peptides*. (John Wiley & Sons, 2012).
33. Saarikangas, J., Zhao, H., Pykäläinen, A., Laurinmäki, P., Mattila, P. K., Kinnunen, P. K., Butcher, S. J. & Lappalainen, P. Molecular mechanisms of membrane deformation by I-BAR domain proteins. *Current biology* **19,** 95–107 (2009).

34. LeVine III, H. [18] Quantification of β-sheet amyloid fibril structures with thioflavin T. *Methods in enzymology* **309,** 274–284 (1999).
35. Bolder, S. G., Sagis, L. M., Venema, P. & van der Linden, E. Thioflavin T and birefringence assays to determine the conversion of proteins into fibrils. *Langmuir* **23,** 4144–4147 (2007).
36. Hawe, A., Sutter, M. & Jiskoot, W. Extrinsic fluorescent dyes as tools for protein characterization. *Pharmaceutical research* **25,** 1487–1499 (2008).
37. Biancalana, M. & Koide, S. Molecular mechanism of Thioflavin-T binding to amyloid fibrils. *Biochimica et Biophysica Acta (BBA)-Proteins and Proteomics* **1804,** 1405–1412 (2010).
38. Gade Malmos, K., Blancas-Mejia, L. M., Weber, B., Buchner, J., Ramirez-Alvarado, M., Naiki, H. & Otzen, D. ThT 101: a primer on the use of thioflavin T to investigate amyloid formation. *Amyloid* **24,** 1–16 (2017).
39. Chapman, M. R., Robinson, L. S., Pinkner, J. S., Roth, R., Heuser, J., Hammar, M., Normark, S. & Hultgren, S. J. Role of Escherichia coli curli operons in directing amyloid fiber formation. *Science* **295,** 851–855 (2002).
40. Barnhart, M. M. & Chapman, M. R. Curli biogenesis and function. *Annu. Rev. Microbiol.* **60,** 131–147 (2006).
41. Dueholm, M. S., Petersen, S. V., Sønderkær, M., Larsen, P., Christiansen, G., Hein, K. L., Enghild, J. J., Nielsen, J. L., Nielsen, K. L. & Nielsen, P. H. Functional amyloid in Pseudomonas. *Molecular microbiology* **77,** 1009–1020 (2010).
42. Pang, Z., Raudonis, R., Glick, B. R., Lin, T.-J. & Cheng, Z. Antibiotic resistance in Pseudomonas aeruginosa: mechanisms and alternative therapeutic strategies. *Biotechnology Advances* **37,** 177–192 (2019).
43. Dueholm, M. S., Søndergaard, M. T., Nilsson, M., Christiansen, G., Stensballe, A., Overgaard, M. T., Givskov, M., Tolker-Nielsen, T., Otzen, D. E. & Nielsen, P. H. Expression of Fap amyloids in P seudomonas aeruginosa, P. fluorescens, and P. putida results in aggregation and increased biofilm formation. *Microbiologyopen* **2,** 365–382 (2013).

44. Biesecker, S. G., Nicastro, L. K., Wilson, R. P. & Tükel, Ç. The functional amyloid curli protects Escherichia coli against complement-mediated bactericidal activity. *Biomolecules* **8,** 5 (2018).

Chapter 7 Conclusions and Future Work

This final chapter highlights the main outcomes and conclusions achieved in the project about MrCP19 and MrCP20's surface behavior in relation to their molecular structure. Based on the results and their contribution to current knowledge of the function of barnacle cement proteins, further experiments are suggested. Future work is proposed to further elucidate how these proteins, together with other cement components and surrounding materials, can contribute to the barnacle adhesion as well as provide guidelines to develop new types of water-resistant bioadhesives.

7.1 General Conclusion and Discussion

In this thesis, an integrative approach from protein analysis to surface sensitive techniques was used to understand the structural behavior of the two barnacle cement proteins MrCP19 and MrCP20, as well as their biophysical functional roles during the barnacle's growth and firm attachment on surfaces.

The first aim to obtain recombinant proteins using heat shock method and identify the protein morphology was presented in **Chapter 3**. The results demonstrated that the monomeric form of the proteins was obtained after using two-step purification methods, with higher amount of β-sheet component and amyloid fibrils detected from MrCP19 compared to MrCP20.

In **Chapter 4**, the second objective to understand the proteins' surface adsorption and adhesion behavior based on their biochemical properties was accomplished by employing different surface sensitive techniques. Intermolecular forces controlling surface adhesion was discussed and different interfacial role of MrCP19 and MrCP20 were suggested.

Molecular-level coordination of MrCP20 with calcium carbonate to understand the protein's functional role in participating to base plate biomineralization was examined for the third objective in **Chapter 5**. The mutual influence of MrCP20 and calcium carbonate was observed, elucidating the protein's contribution to barnacle base and side plates growth regulation for synchronizing adhesive development and protective calcareous plate growth.

Chapter 6 discussed the last aim, namely the investigation of the potential antimicrobial activity of MrCP19 relating to its amyloid-like fibrillar structure. The results suggested that MrCP19 can inhibit bacterial growth by aggregating group of cells mediated by the amyloid structure of MrCP19.

In summary, this work successfully broadened the knowledge of two key MrCPs, which improves our overall understanding of barnacles' cement components and their functional roles at interfaces. MrCP19 showed strong fibrillation behavior in solution, especially under acidic condition, and this was directly related to its fibrous and dissipative structure when adsorbed on surface. We observed the unique structural behavior of MrCP19 on surface to perform distinguishing adherence between two surfaces, as well as potential antimicrobial effect. MrCP20 possessing great amount of negatively charged residues, adsorbed on surfaces as a strong and rigid layer, playing great adhesion energy. More interestingly, mutual influence of MrCP20 and $CaCO_3$ was discussed, and potential mineralization regulation function of the protein. These results can describe the distinct functional roles of the two proteins, and furthermore, it can bring one step forward to understand the multi protein cement layer together with discovery of cooperation with other components in the future.

Barnacle underwater adhesion is still being investigated through multidisciplinary research approaches, and the work has potential to develop barnacle-inspired technologies for biocompatible bacterial-resistant wet adhesives.

Pursuing these outcomes met several minor and major challenges.

i. Above all, protein loss was inevitable during and after protein purification due to their susceptibility to aggregation in solution and/or on surfaces, and adsorption to various surfaces. Careful observations on their behavior were necessary, and efforts to prevent them from premature aggregation or adhesion should have been followed in every step of the expression and purification process. Since MrCP19 and MrCP20 are adhesive proteins, they tended to stick to the columns used for purification. Manually controlling the injection of the protein solution and elution buffer into Ni-NTA columns improved protein binding to the beads as well as protein harvest by providing good pressure to the proteins and keeping favorable local concentration of the proteins inside the columns. Dialysis in Tris buffer was followed to remove impurities from the eluted solution. This method could minimize protein attachment to the SEC column and valves. Spinning rate and running time for protein concentration step was maintained at moderate levels, with continuous pipetting between each run to prevent protein aggregation.

ii. Controlled fibril formation of the proteins on surfaces was difficult to achieve. Different model surfaces were prepared to optimize consistent fibrillation, and different buffers were prepared under different pH conditions, salt concentrations, protein concentration, and time point of incubation. All the possible factors affecting fibril formation had to be carefully compared to infer reliable conditions for fibril formation.

iii. Protecting the proteins and bacteria cells from infection was challenging especially when both were used for experiments in the same spaces. The protein samples and the cells cultures or plates were handled carefully throughout the experiments.

iv. $CaCO_3$ crystals for the experiment were grown using vapor diffusion method, where the CO_2 diffusion kinetics can be affected by various factors. The freshness of materials, any little defect from experimental tools, timing for different steps, and other experimental methods were carefully controlled. Multiple sets of the experiment were repeated to minimize non-constant environmental conditions (such as temperature and humidity) and achieve statistical significance.

7.2 Future Perspectives

7.2.1 Surface Adhesion and Fibril Formation Mechanism of MrCP19 on Different Surfaces

MrCP19 incubated in either basic or acidic pH condition was confirmed to form nanofibrils when it was deposited on mica surface at low concentration (**Chapter 4**). Different types of nanofibrils were also observed in the presence of bacteria cells' amphiphilic membrane (**Chapter 6**). However, the detailed mechanism of fiber self-assembly is not yet fully understood. The effects of increasing protein concentration, buffer salt concentration, and pH were studied with CD measurements and ThT assay, but no unambiguous conclusion could be driven. As no fibrillation mechanism was identified from protein solution, studies focusing on surfaces as a trigger for fibrillation would be worth exploring. A preliminary liposome study (performed after antimicrobial tests in **Chapter 6**) to observe either change in protein structure or vesicle structural damage was not conclusive. Functionalizing the planar surfaces using thiols with positively charged, negatively charged, or hydrophobic terminal groups, would be a promising alternative to elaborate how these different functional groups on surface affect the protein's structural behavior. In order to analyze protein adsorption, fibrillation, and other conformational structuring at the molecular level, surface sensitive techniques such as nanoplasmonic sensing (NPS) technology and localized surface plasmon resonance (LSPR) can be used for shorter sensing depth observation.[1,2]

Positively charged and negatively charged surfaces as well as hydrophobic surfaces can be prepared by functionalizing Au slides with different functional groups ($-NH_2$, -COOH, and $-CH_3$), using the functionalization method explained in **Chapter 5**. The combination of PM-IRRAS, QCM-D, XPS, AFM, and other surface techniques using different SAMs can provide information about the orientation of the protein on surface, and furthermore, the fibril growth process (**Figure 7.1-2**).[3,4] Using the SAMs for other experiments such as SFA, QCM-D, and LSPR would consequently explain how the surface affected proteins' fibril structural behavior would drive their surface adsorption and adhesion behavior.

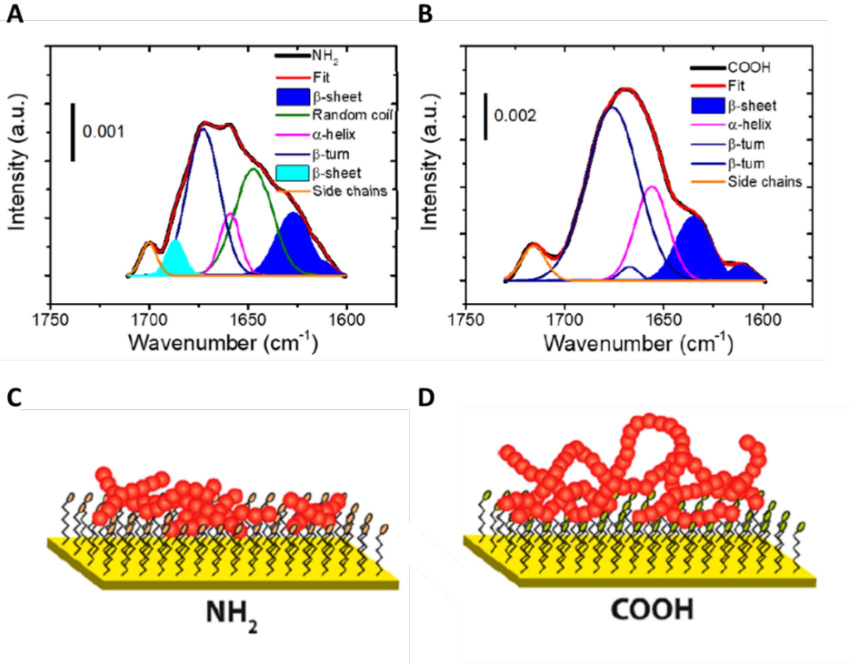

Figure 7.1 Deconvolution of the PM-IRRA spectra in the amide I region recorded for hIAPP adsorption onto a **(A)** NH_2- and **(B)** COOH- terminated SAM on a Au substrate, respectively. Black lines correspond to the experimental data while red lines represent the sums of the fitted components. **(C-D)** Schematic representation of hIAPP fibrillization at the different SAMs.[3]

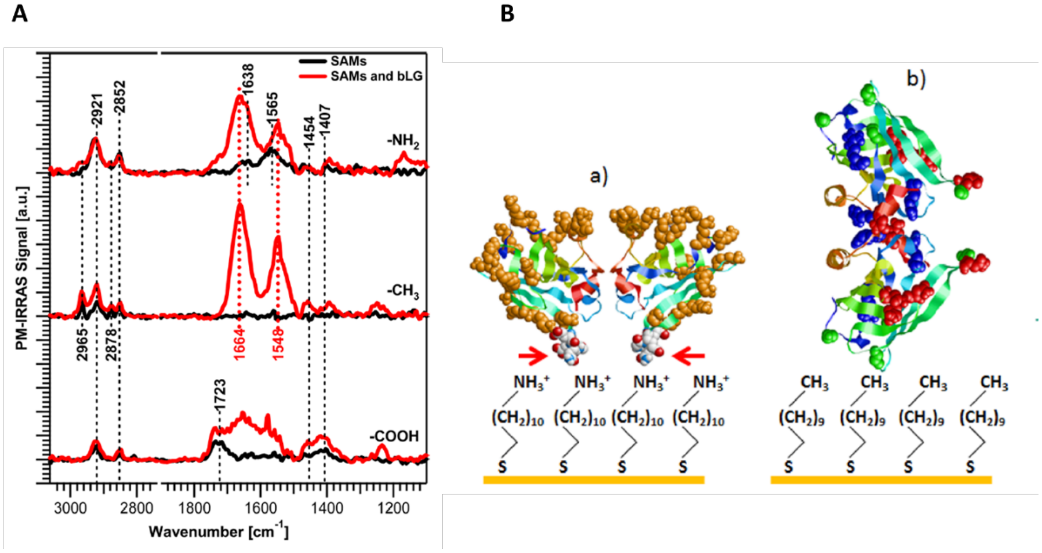

Figure 7.2 (A) PM-IRRAS measurements before and after βLG adsorption on COOH-, CH_3-, and NH_2-terminated SAMs. **(B)** Part of proposed orientation of βLG on $-NH_2$ (a) and CH_3 (b) terminated SAMs.[4]

7.2.2 In-time Crystallization Observation Using Surface Sensitive Technique

From this thesis, quantitative and kinetic information during $CaCO_3$ crystallization process regulated by MrCP20 was obtained in **Chapter 5**. The final crystallized mass of $CaCO_3$ was decreased by ~30% with the protein and the growth kinetic was also retarded due to the interaction between the charged amino acid residues composing the protein and Ca^{2+} and CO_3^{2-} ions. While the pure $CaCO_3$ showed only calcite phase existing according to Raman spectroscopy, $CaCO_3$ grown in the presence of MrCP20 contained both vaterite and calcite phase (**Figure 5.1A**). In an attempt to measure the evolution of the structure of calcite microparticles (μPs) on Au/MUA, X-ray diffraction (XRD) was performed on crystals grown on MUA/Au using Rigaku Smartlab in/out plane diffractometer (**Appendix**).

As we observed the destruction or decomposition of calcite crystals by microscopy in **Chapter 5**, enhanced heterogeneity due to the protein was confirmed by XRD. Due to longer preparation time and limited experimental condition (specifically, the transition from a closed liquid environment for the crystal growth to an open-air environment for XRD measurement without external influence, was difficult to achieve), it was challenging to follow crystal phase transformation and its kinetics using XRD.

In order to map the phase transformation mechanism of calcium carbonate from amorphous to vaterite to calcite regulated by MrCP20, more precise x-ray diffraction information at the earlier stages of phase transformation is required. Synchrotron studies, which enables in-situ and time-resolved diffraction at the solid/liquid interface, would help achieve this objective.

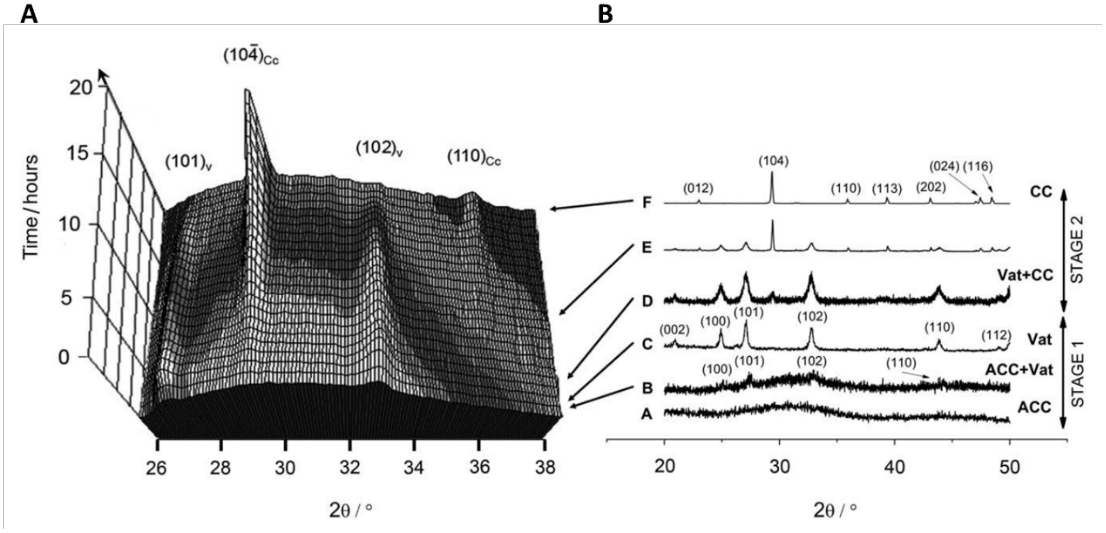

Figure 7.3 (A) Three-dimensional representation of time-resolved ED-XRD patterns showing the evolution of vaterite (101), (102) and calcite (104) and (110) reflections. **(B)** X-ray diffraction patterns of solids collected at different elapsed times during the off-line experiments, showing ACC, vaterite and calcite solid phases.[5]

A solid/liquid mylar cell[6] can be used to flow in-situ the liquid precursors containing or lacking MrCP20, and observe the growth of the µPs. With a scan speed of a few 10th of seconds, we would be able to successively acquire radial and azimuthal reference scans in plane at a grazing incidence of a few degrees, and to follow the phase transition of the µPs from its initial stage. It is a crucial information to reveal barnacle's unknown mechanism of regulating base plate growth and cement development, but also to prove the cement protein's functional role at the interfacial layer. This would further lead to the discovery of molecular strategies of the barnacle cement layers that exhibit cooperative functions of surface adhesion as well as biomineralization control.

References

1. Melby, E. S., Allen, C., Foreman-Ortiz, I. U., Caudill, E. R., Kuech, T. R., Vartanian, A. M., Zhang, X., Murphy, C. J., Hernandez, R. & Pedersen, J. A. Peripheral membrane proteins facilitate nanoparticle binding at lipid bilayer interfaces. *Langmuir* **34,** 10793–10805 (2018).

2. Bohren, C. F. & Huffman, D. R. *Absorption and scattering of light by small particles*. (John Wiley & Sons, 2008).

3. Hajiraissi, R., Hanke, M., Yang, Y., Duderija, B., Orive, A. G., Grundmeier, G. & Keller, A. Adsorption and Fibrillization of Islet Amyloid Polypeptide at Self- Assembled Monolayers Studied by QCM-D, AFM, and PM-IRRAS. 8 (2018).

4. Lebec, V., Landoulsi, J., Boujday, S., Poleunis, C., Pradier, C.-M. & Delcorte, A. Probing the orientation of β-lactoglobulin on gold surfaces modified by alkyl thiol self-assembled monolayers. *The Journal of Physical Chemistry C* **117,** 11569–11577 (2013).

5. Rodriguez-Blanco, J. D., Shaw, S. & Benning, L. G. The kinetics and mechanisms of amorphous calcium carbonate (ACC) crystallization to calcite, via vaterite. *Nanoscale* **3,** 265–271 (2011).

6. Garai, D., Solokha, V., Wilson, A., Carlomagno, I., Gupta, A., Gupta, M., Reddy, V. R., Meneghini, C., Carla, F. & Morawe, C. Studying the onset of galvanic steel corrosion in situ using thin films: film preparation, characterization and application to pitting. *Journal of Physics: Condensed Matter* **33,** 125001 (2021).

Appendix

1. List of Publications

Hur, S. ; Méthivier, C. ; Wilson, A ; Boujday, S. ; Miserez, A. Biomineralization in barnacle base plate with the effect of adhesive cement proteins. *(to be submitted)*

Hur, S. ; Wang, J. ; Yu, J. ; Boujday, S. ; Miserez, A. Surface adsorption and adhesion studies of barnacle cement proteins with structural understanding. *(to be submitted)*

Hur, S. ; Rice, S. ; Boujday, S. ; Miserez, A. Potential antimicrobial activity in link with amyloid fibrillization of barnacle cement proteins. *(to be submitted)*

2. Oral and poster communications

Oral presentation :

Hur, S. *et al.*, Barnacle Cement Proteins : Adhesion, Adsorption, and Biomineralization, SU-NTU joint webinar - **Oct 2021**

Hur, S. *et al.*, Biomineralization Study of Barnacle Adhesive Cement Proteins on Functionalized Gold, Journées plénières GdR B2i, Toulouse - **Sep 2021**

Hur, S. *et al.*, Biomineralization of Barnacle Base Plate in Association with Adhesive Cement Proteins, Goldschmidt, Lyon - **July 2021**

Hur, S. *et al.*, Biomineralization of Barnacle Base plate in Association with Adhesive Cement Proteins, SU-NTU joint webinar - **June 2021**

Hur, S. *et al.*, Understanding Molecular Mechanism of Underwater Barnacle Adhesion in terms of Protein Behavior on Surface, 4th Meeting of the French-Singaporean Research Network on Renewable Energy (SINERGIE) GDRI, Singapore - **Nov 2019**

Poster presentation :

Hur, S. *et al.*, Understanding Molecular Mechanism of Barnacle's Underwater Adhesion Through Cement Proteins Studies, The 16th Pacific Polymer Conference (PPC16), Singapore - **Dec 2019**

3. Additional studies

XRD patterns provide information of thin-film structure, such as crystal orientation, lattice distortion, and crystallite anisotropy, where in-plane XRD has strength in analyzing an extremely thin-film. [1,2] The evolution of the $CaCO_3$ crystal grown on Au/MUA was studied using Rigaku Smartlab in/out of plane X-ray diffraction analysis (**Figure A.1**).

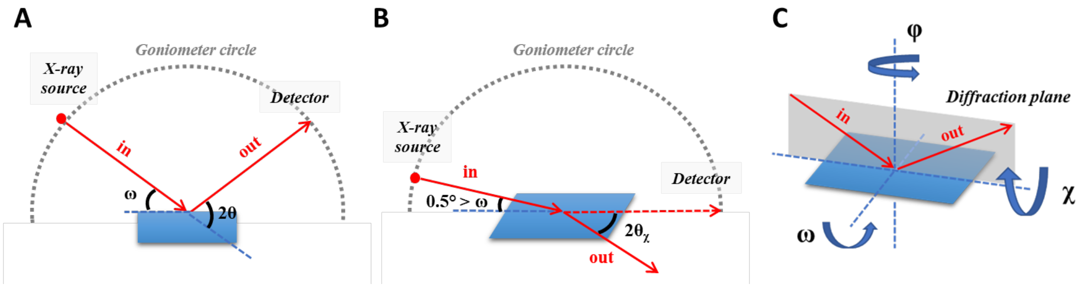

Figure A.0.1 Schematic representation of (**A**) Out of plane and (**B**) In plane XRD diffractometer and (**C**) definition of rotational axis according to Euler's system.

A post-mortem sample was fitted in the diffractometer equipped with an intense Cu Kα 9 kW rotating anode. Out of plane scan produced an intense peak at $2\theta = 29.4°$ associated to calcite (104), together with presence of Au (111) at $2\theta = 38.27°$ (**Figure A.2**). This indicates that (104) is the preferential orientation of calcite on Au layer in this sample. Rocking curve (omega-scan) represents in general the misorientation distribution of lattice planes, where we could observe the calcite crystals grown without the protein were aligned well at lattice plane (104) (**Figure A.2B**). In plane scan identified calcite (110), (113), and (116), as well as Au (220) (**Figure A.2C**). In particular, the main peak (calcite (110)) is the in-plane counterpart of calcite (104) out-of-plane preferential orientation. These values correspond well to previously-proposed common lattice planes of $CaCO_3$ crystals grown on even-length (C_{10} (MUA), C_{14}, and C_{16}) carboxylic acid terminated alkylthios, attributed to certain alignment of the terminal groups.[3,4] Azimuthal scan at calcite (110) in the range of 60° (with the symmetry of hexagonal system) showed that (110) faced calcites are in-plane randomly distributed (**Figure A.2D**).

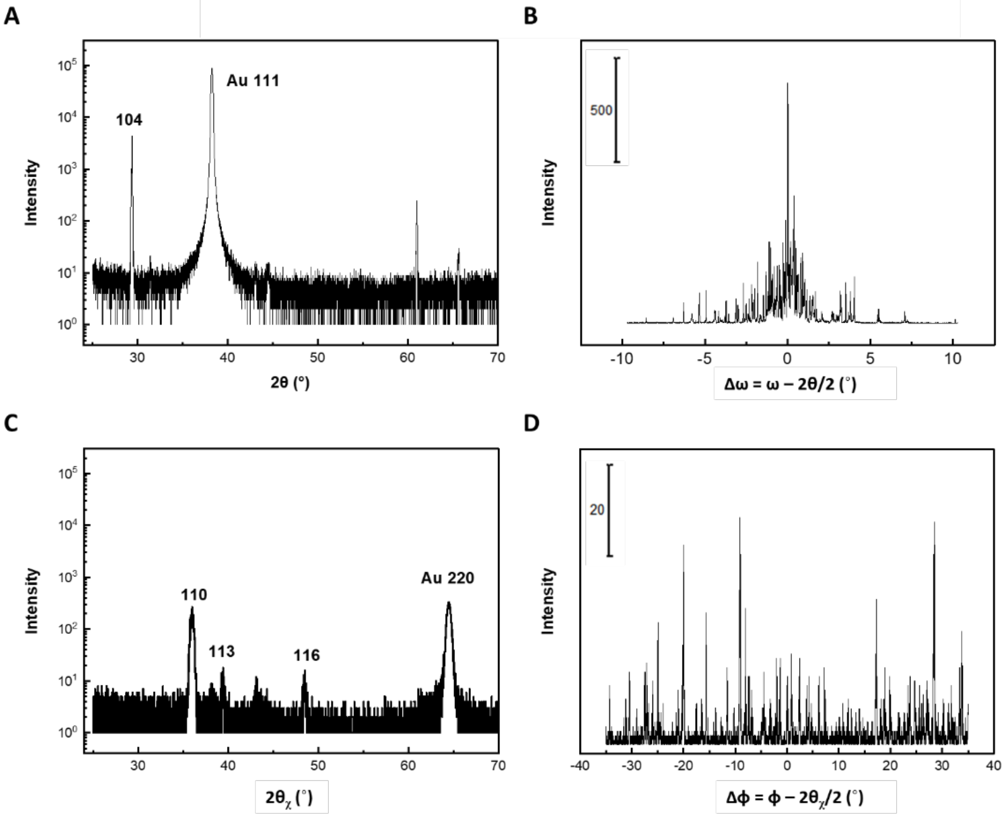

Figure A.0.2 Out of plane (**A-B**) and in plane (**C-D**) XRD scans representing calcite crystals in good alignment and distribution. Indices assigned to different peaks indicate lattice planes of calcite, or Au as specified.

Parallel experiments were conducted for the crystals grown in the presence of MrCP20 on surface, in order to study the effect of protein on crystallinity throughout the whole surface in contrast to Raman analysis on single crystals. Out-of-plane results showed lower intensity of calcite (104) in the presence of MrCP20 compared to control calcite crystals. (**Figure A.3A-B**). Additional peaks from calcite crystals were observed from in-plane scanning in the presence of MrCP20 (**Figure A.3C-D**). Calcite with the crystal faces (104), (202), and (018) were obtained and no vaterite was observed. As we observed the destruction or decomposition of calcite crystals by microscopy in **Chapter 5**, enhanced heterogeneity due to the protein was confirmed by XRD.

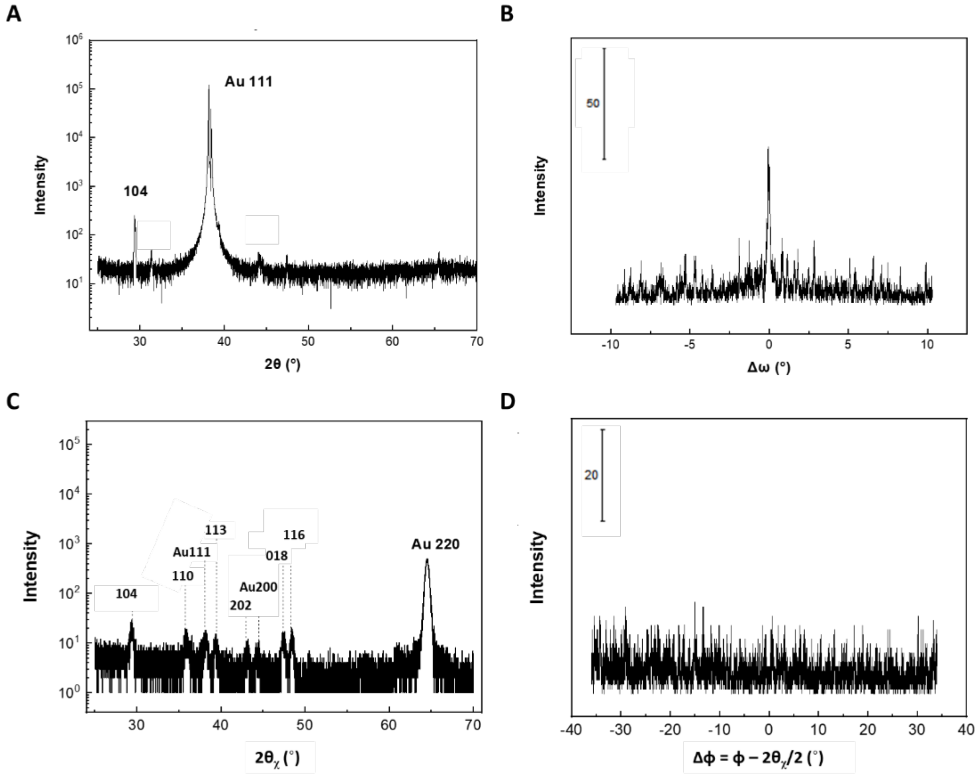

Figure A.0.3 (**A**) Out of plane XRD scan on crystals grown in the presence of MrCP20 on surface, and (**B**) omega scan at calcite (104). (**C**) In plane XRD scan on crystals grown in the presence of MrCP20 on surface, and (**D**) azimuthal scan at calcite (110). Indices assigned to different peaks indicate lattice planes of calcite, or Au as specified.

Reference

1. Chen, Y. *et al.* Plasma assisted molecular beam epitaxy of ZnO on c-plane sapphire: Growth and characterization. *Journal of Applied Physics* **84**, 3912–3918 (1998).

2. Ma, C.-H., Huang, J.-H. & Chen, H. Residual stress measurement in textured thin film by grazing-incidence X-ray diffraction. *Thin solid films* **418**, 73–78 (2002).